Suspension Mechanics at Finite Inertia

by

Pandurang Manohar Kulkarni

A Dissertation Submitted to the Graduate Faculty in Engineering in Partial Fulfillment of the Requirements for the Degree of Doctor of Philosophy
The City University of New York

2009

This manuscript has been read and accepted for the Graduate Faculty in Engineering in satisfaction of the dissertation requirement for the degree of Doctor of Philosophy.

Date	Prof. Jeffrey F. Morris Chair of Examining Committee
Date	Prof. Mumtaz Kassir Executive Officer
	Prof. Joel Koplik
	Prof. Morton Denn
	Prof. Mark Shattuck
	Prof. Gabriel Tardos
	Prof. Taehun Lee

Supervision Committee

THE CITY UNIVERSITY OF NEW YORK

Abstract

Suspension Mechanics at Finite Inertia

by

Pandurang M. Kulkarni

Advisor: Jeffrey F. Morris

This work addresses the influence of microscale inertia on the motion of rigid particles freely suspended in a Newtonian fluid via lattice-Boltzmann numerical simulations. The suspended particles are non-Brownian, neutrally-buoyant and spherical in shape to consider inertial effects exclusively.

First, the relative trajectories of two spheres immersed in finite-inertia simple-shear flow are described. The inertia is characterized by the shear flow Reynolds number $Re = \rho\dot{\gamma}a^2/\mu$, where μ and ρ are the viscosity and density of the fluid respectively, $\dot{\gamma}$ is the shear rate and a is radius of the particle. Reynolds numbers of $0 \leq Re \leq 1$ are considered with a focus on inertia at $Re = O(0.1)$. At finite inertia, the topology of the pair trajectories is altered from that predicted at $Re = 0$, as closed trajectories found in Stokes flow vanish and two new forms of trajectories are observed. These include spiraling and reversing trajectories in addition to largely undisturbed open trajectories. For $Re = O(0.1)$, the limits of the various regions in pair space yielding open, reversing and spiraling trajectories are roughly defined.

In a pressure-driven pipe flow at finite Reynolds number, suspended particles are known to undergo lateral migration to a specific position off the centerline. We investigate the inertia-driven lateral migration of a single particle in a rectangular conduit flow. The parameters that affect the cross-stream motion are particle size relative to the channel (W/d), aspect ratio of the channel (H/W) and the shear

rate based Reynolds number on the particle scale, Re_p. The particle equilibrium positions in rectangular cross-section are obtained by the trajectory analysis with various starting positions of the particle. In a 2:1 channel with particle of size one-third of the channel width, it is found that the particle migrates to the center of the longer edge and the rate of approach scales linearly with Re_p. Upon changing the particle size and the aspect ratio, we find a bifurcation in the form of multiple equilibrium locations. In case of a dilute suspension, the existence of particle ordering in the axial direction and the underlying physical mechanism are also discussed.

Furthermore, we examine the effect of particle-scale inertia on the rheology of a dense suspension subjected to simple-shear flow. The dimensionless parameters governing the bulk rheology are the solid-volume fraction ϕ and the Reynolds number $Re = \rho\dot{\gamma}a^2/\mu$. Using the lattice Boltzmann simulations in a wall-bounded shear flow, the time averaged particle stress is computed. The relative viscosity, normal stress differences and particle pressure are reported for $0.01 \leq Re < 5$ and $0.05 \leq \phi \leq 0.3$. The anisotropy in microstructure at finite Re is also studied through the pair distribution function $g(\boldsymbol{r})$.

The suspension balance approach is then used to perform "computational suspension dynamics". Specifically we develop continuum modeling of suspension flows with inertia to predict the velocity and particle concentration profiles in a pressure-driven pipe flow. The particle-scale inertia is taken into account by modifying the model for particle stress and introducing the lateral force associated with inertial migration to the particle phase momentum balance. Case studies on cross-stream migration are provided and it is found that the predicted profiles show the influence of inertia in a manner consistent with the limited experimental data.

Acknowledgements

First and foremost, I am heartily thankful to my advisor, Prof. Jeffrey Morris, whose guidance and supervision from the initial to final level enabled me to develop an understanding of the subject. His perpetual energy, acute physical insight on problems and exceptional collaborative skills not only motivated me at every stage of this thesis work but also enriched my growth as a researcher. On many occasions, he shared his own experiences for my betterment. I am indebted to him more than he knows.

I would like to thank my PhD committee, Prof. Joel Koplik, Prof. Morton Denn, Prof. Mark Shattuck, Prof. Taehun Lee, and Prof. Gabriel Tardos for their constructive comments on this thesis. I am grateful to Prof. Tony Ladd of the University of Florida for generously providing the lattice-Boltzmann code. A special thanks to our Harvard collaborators, Prof. Howard Stone and Katherine Humphry for the enlightening email discussions on inertial migration problem. To Prof. Maldarelli and Prof. Rumschitzki, thanks a lot for the wonderful courses you taught me.

In addition, I gratefully acknowledge Dr. Guy Metcalfe for inviting me to work on "Reactive transport in porous media," at CSIRO, Melbourne. I am also thankful to Dr. Daniel Lester, Dr. Alison Ord and Dr. Murray Rudman for many stimulating discussions during my stay.

Many thanks go in particular to Anil Kumar, John Singh and Rohit Ingale for sharing their thoughts with me, which were very fruitful for shaping my career. Furthermore, I would like to thank my present and past group members: Hameed, Sandeep, Prasad, Jorge, Yevgeny, Bloen, Xiajuan and Ehssan for providing a great work environment in the lab. To Andy, Xu and Mary, thanks for all your help during these

years.

I convey special acknowledgment to my friends: Amar, Vikas, Manoj, Shyam, Nikhil, Gogo, Joshi, Rajesh, Ashish, Swapnil, Abhinav, Jayant, Nilesh, Vilobh, Pratik, Prasad Y, and Mayur. I feel extremely fortunate to have them around whenever I needed (may it be a break for coffee or cricket).

I would like to express my sincere appreciation to beloved Keshav Shinde Sir of Suyash High School, Solapur, who motivated me to join UDCT and to pursue higher education in Chemical Engineering.

Where would I be without my family? Words fail to express my gratitude to my wife, Sonali. I owe her for her love and inseparable support, especially in these stressful thesis writing days (and nights). I am thankful to my brother, Mandar, who always cheered me. Finally, I would like to dedicate this thesis to my parents, Mrs. Ashwini Kulkarni and Mr. Manohar Kulkarni, for their dedication, love and prayers. I am extremely indebted to them for providing the necessary steppingstone to achieve my goals in life.

Pandurang M. Kulkarni

Contents

List of Figures

List of Tables

Chapter 1

Introduction

1.1 Motivation and background

A suspension is an important class of two-phase materials in which the discrete phase consists of solid particles and the continuous phase is a gas or a liquid. Suspensions are ubiquitous in nature as well as in industry. For example, particulate suspensions are involved in the manufacturing processes of many chemical industries – foods, paints, coatings, and personal care products are examples. Particle-laden flows are also found in fluidization, packed beds, slurry reactors, crystallization and other unit operations. In practice, the flow conditions range from laminar to turbulent and many intriguing phenomena such as resuspension and hydrodynamic instabilities occur in suspensions. But we do not know how to account for many of these effects quantitatively. As a result, understanding the transport properties of suspension flows remains a fundamental problem in fluid mechanics.

The simplest type of suspension is composed of rigid spherical particles suspended in a Newtonian fluid. Under the application of flow, the inability of rigid particles to undergo deformation generates an additional dissipative mechanism at the microscale and adds to the bulk viscosity of the system. The viscosity of the suspension has been an active area of research since Einstein's pioneering work about a hundred years ago.

He showed that in the dilute limit a suspension is Newtonian but with an effective viscosity that is higher by $(1 + 2.5\phi)$ times the fluid viscosity, where ϕ is the solid fraction [1]. When the solid fraction is increased, the suspended particles interact through hydrodynamics, Brownian motion and interparticle forces. A balance of these interactions leads to a macroscopic behavior that is significantly different from the Newtonian fluid. This includes rate dependence (shear thinning and thickening), viscoelasticity and thixotropy–rheology varying with time.

To describe the detailed motions of a mixture requires solving of the equations of motion with appropriate boundary conditions. On the microscale, the mechanics of the Newtonian fluid is governed by the Navier-Stokes equation,

$$Re(\frac{\partial \boldsymbol{u}}{\partial t} + \boldsymbol{u} \cdot \boldsymbol{\nabla} \boldsymbol{u}) = -\nabla p + \nabla^2 \boldsymbol{u}, \tag{1.1}$$

where $\boldsymbol{u}$ and p are the fluid velocity and pressure. The velocity, distance and time are nondimensionalized by U, a and a/U, respectively, where U is the velocity scale, and a is radius of a particle. The Reynolds number, Re, characterizes the strength of inertial forces over viscous forces. On the particle scale, it is defined as $Re = \rho U a/\mu$, and ρ and μ are the density and viscosity of the fluid, respectively. When the fluid is viscous and particles are small, one can assume $Re = 0$. This is referred to as a *Stokes flow* or *creeping flow* that provides a limiting case where viscous forces dominate over the inertial forces. Due to linearity of hydrodynamic equations, various analytical solution techniques such as Green's functions and multipole expansions have been developed for the Stokes flow [2, 3].

The suspension mechanics at low Reynolds number was developed after Batchelor [4] who derived an expression for the bulk stress that involved contributions from the fluid and the particle phases. He also identified the importance of the pair

problem in understanding rheology of dense suspensions and provided an analytical solution for the motion of two particles in simple shear flow [5, 6]. Subsequently, more sophisticated solutions of the pair problem followed that computed the near-field and the far field pair interactions to a high degree of accuracy [7, 8, 9, 10]. These analytical theories provided the foundation of computer simulation tools such as Stokesian Dynamics [11, 12]. The quasi-steady nature of Stokes flow means that only particle positions and boundary motions or driving forces are sufficient to define the dynamics. As a consequence, the resistance and mobility formulations facilitate the computation of translation (force and velocity), rotation (torque and rotation rate) and particle contribution to the bulk stress (stresslets). Furthermore, linearity of the creeping flow allows superposition of independent solutions and has been exploited to study the combined effect of shear and Brownian motion on the suspension rheology [13, 14, 15, 16].

Various analytical [14] and simulation results [17, 15, 16, 18] showed that a strongly sheared suspension exhibits normal stresses and a viscosity that increases in a complex fashion with the volume fraction. The key issue is the microstructure which refers to the statistical description of relative positions and orientations of the particles [19, 14]. The sheared suspension at the particle level exhibits structural anisotropy that provides a means to explain the normal stresses and viscosity [16]. Experimental work carried out on the Stokes flow suspension not only validated the rheological findings [20, 21, 22] but have also revealed interesting bulk phenomena such as *shear-induced migration* [23, 24, 25, 26] in shear-rate varying flows. A constitutive stress law relating the mixture stress to the strain rate has been proposed that describes the observed bulk phenomena to a reasonable accuracy [27, 28, 29].

Thus a Stokes flow suspension is well-examined and a range of aspects of the flow are well-understood. However, the role of inertia on the motion of suspended particles

has not been understood with any degree of thoroughness. It is to be noted that the fluid inertia is important in many industrial applications. The transport of suspension slurries in petroleum, waste disposal, coal and mineral processing involves particles of large size and water based low-viscosity fluids at elevated flow rates. Therefore the inertial effects in such cases are dominant and hence cannot be ignored. For design purposes, the current approaches rely heavily on the empirical correlations, e.g. pressure-drop calculations in a packed bed [30]. But from the scientific point of view, a mechanistic description of inertia on microscale is desirable. Such a description is the central goal of this study.

Inertia at the microscale is the root cause of interesting effects even in the dilute limit. In a pressure-driven circular pipe flow at small inertia, the particles migrate to an equilibrium position located at a distance of three-fifths of the pipe radius from the axis [31, 32, 33]. The relative motion between the particle and the fluid at small but finite inertia causes a lift force that acts perpendicular to the stream-wise direction [34]. Analytical studies on a point particle in the Poiseuille flow are able to predict the lateral force [35, 36, 37, 38].

The linear flows such as simple shear are basic to the understanding of transport properties. A finite Reynolds number shear flow qualitatively alters the topology of streamlines around a single particle [39, 40, 41, 42] from that predicted at $Re = 0$ [4]. An important aspect of the disturbance flow around the particle was missed in earlier studies and has been found only recently: the streamlines close to the surface of the particles are not closed but actually spiraling [43, 44]. This has some important implications in heat and mass transfer problems as inertia provides a convective means of transport through outward spiraling streamlines.

The rheology of a sheared suspension is important for the development of a constitutive description. One of the striking features of the fluid inertia is that it

alters the Newtonian rheology even at the single particle level [45]. Inertia introduces added stress due to acceleration of particles and the fluctuations in the fluid velocity. The latter is often termed a Reynolds stress and is of the form $\rho\langle \boldsymbol{u}'\boldsymbol{u}'\rangle$, where the angled brackets denote the ensemble average and $\boldsymbol{u}' = \boldsymbol{u} - \langle \boldsymbol{u}\rangle$ denotes the fluctuation velocity from the mean flow, $\langle \boldsymbol{u}\rangle$ [4]. Weak inertia ($Re \ll 1$) leads to increase in the particle contribution to the viscosity and gives rise to normal stresses [45].

Here, the fluid inertia needs to be distinguished from the particle inertia. A relevant dimensionless number is the Stokes number defined as $St = \rho_p/\rho_f Re$, where ρ_p is the density of solid particles. This is important in gas-solid suspensions where the density of solid particles is much higher than the gas. The rheological behavior of these systems is governed by particle contacts and has been characterized in the limit of $St \gg 1$ but $Re \ll 1$ [46]. This is, however, not the focus of this study. We consider liquid-solid suspensions for which $St \approx Re$ is valid.

The progress in understanding the many-body interactions and rheology of a dense suspension at $Re = O(1)$ has been slow [47]. The inclusion of convective terms on the left hand side of the Navier-Stokes equation adds unsteadiness and nonlinearity to the problem. Unlike Stokes flow, the fluid flow is needed to determine the Reynolds stress term, $\rho\langle \boldsymbol{u}'\boldsymbol{u}'\rangle$. This rules out analytical solutions even for the single particle and one has to rely on perturbative or fully numerical approaches. In experiments, a high fluid inertia requires a low viscosity fluid like water. As a result density-matching becomes increasingly difficult. Consider, for example, particles of size 100 μm suspended in low viscosity fluid like water. Even a slight density difference of 0.01 gm/cc causes a characteristic settling time, $\tau_s = a/u_t$ of 1 second, where u_t is the terminal settling velocity. This restricts the experimental investigation using conventional rheometers where bulk length scale is of order $10a$.

On the other hand, because of recent progress in numerical methods and

computational resources, numerical studies have become an important tool for studying inertial suspensions. The three-dimensional problems for the case of uniform flow around isolated bodies have been extensively studied by direct numerical simulations [48]. Some basic issues like the disturbance flow around the body and the drag and lift have been examined over a range of Reynolds numbers and flow conditions (laminar to turbulent). The shear flow over a single particle has also been addressed and the dilute limit rheology compared with predictions of asymptotic theory [45]. Finite element method (FEM) simulations on many-body problems at finite Re are mainly limited to sedimentation [49] and two-dimensional sheared suspensions [50, 51]. This is primarily due to computational cost and algorithmic complexity associated with meshing and remeshing as the particles move. Some other promising computational methods include dissipative particle dynamics [52] and force coupling methods [53].

Recently, lattice-Boltzmann method (LBM) has gained much attention in fluid flow problems involving particulate suspensions [54, 55, 56, 57]. LBM is a mesoscopic simulation method that solves the Navier-Stokes equations for the fluid and Newton's equation of motion for the particles. Unlike Stokesian Dynamics, LBM is capable of simulating flow at finite Reynolds number, and is also flexible analysis of disperse particles. Compared with FEM, the LBM algorithm is relatively simple and because of its spatial locality, it is an ideal candidate for parallelization. The capability of LBM in computing near-field particle interactions has been demonstrated previously [57, 58, 59]. As a result, it has been exploited to examine the pair motion [60] and the viscosity of concentrated suspensions [61, 62, 63].

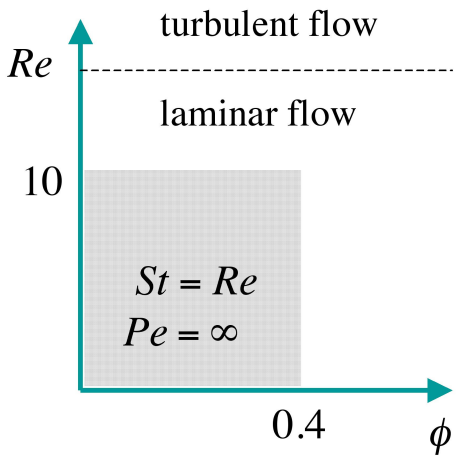

Figure 1.1: Sketch of parameter space and the domain of validity (shaded region) of our study.

1.2 Goals and outline

From the overview of previous section, it is clear that many fundamental problems concerning the role of fluid inertia on particle motion are yet to be examined. In this work, we systematically study those problems that are basic to the development of suspension mechanics at finite Reynolds number. To keep the description simple, we limit our parameter space and address the inertial effects exclusively. For this reason, we assume non-Brownian ($Pe \to \infty$), neutrally-buoyant ($St = Re$) and monodisperse particles. The fluid is Newtonian with density ρ and viscosity μ. The conditions are chosen such that bulk flow is laminar and well below the turbulent regime. A sketch of the parameter space and the domain of validity of our work is shown in figure 1.1.

We chose to work with the lattice-Boltzmann method to generate the numerical results presented in this study. LBM as developed for particulate suspensions is described in chapter 2. The development of the three-dimensional LBM model, inherent fluid mechanics and the solid-fluid boundary conditions are discussed. The lubrication correction, which is an important aspect of near-field pair hydrodynamics,

and the stresslets that are related to particle contribution to bulk stress are addressed briefly.

Chapter 3 investigates the motion of a single particle and pair of particles of equal radii when subjected to simple shear flow, $\boldsymbol{u} = (\dot{\gamma}y,\ 0,\ 0)$, where $\dot{\gamma}$ is the shear rate. The Reynolds number on particle scale is defined as $Re = \rho\dot{\gamma}a^2/\mu$. First, we analyze the three-dimensional flow around the single particle at finite Re in order to understand the in-plane and out-of-plane spiraling streamlines in the vicinity of particle. It also provides some guidance in consideration of pair motion which is the main focus of the chapter. In the subsequent sections we delineate the nature of pair trajectories in the range $0 \leq Re \leq 1$ with a focus on inertia at $Re = O(0.1)$. A key finding of our work is that the topology of pair trajectories is altered from that predicted at $Re = 0$, as closed trajectories found in Stokes flow vanish and new forms of trajectoreis: *reversing* and *spiraling* appear. We map in three-dimension the regions of pair-space yielding open, reversing and the spiraling trajectories.

In chapter 4, we address the inertia-driven lateral motion of particles when the imposed flow is parabolic in nature. Specifically, we examine the case of pressure-driven flow in a rectangular conduit. The real motivation for the problem comes from recent studies on application of inertial microfluidics in particle separation or filtration. We present a comprehensive examination of equilibrium positions of a single particle in the rectangular cross-section. The parameters that affect particle migration include the size of particle relative to the channel, the channel geometry (aspect ratio) and the Reynolds number on particle scale. The dependence of each parameter on migration is studied separately by varying one parameter keeping others fixed. We typically consider particles of size one-tenth of the channel width or larger in order to investigate finite-size effects. Quite remarkably, we find that in a 2:1 channel when particle is one-third of channel width the particle migrates to the center of the

longer side. The scaling of rate of migration with the Reynolds number is studied.

The final section of chapter 4 is devoted to the investigation of particle interactions at finite inertia that lead to the formation of ordered chains. We perform LBM simulations of a randomly distributed dilute suspension in a 2:1 channel. Under the application of pressure-driven flow, the particles migrate to their equilibrium positions and rearrange to form well-defined structures. We analyze the streamlines in the vicinity of a single particle and the pair motion to elucidate the underlying physical mechanism.

The finite Reynolds number rheology of a sheared suspension of mono-disperse and non-Brownian particles is examined in chapter 5. The numerical simulations are performed in a wall-bounded geometry. Again the Reynolds number is defined as $Re = \rho\dot{\gamma}a^2/\mu$. Using Batchelor's formulation we first outline a procedure to calculate the particle stresslets, Reynolds stress and acceleration stress associated with particle contribution to the total stress. A complete set of time-averaged viscometric functions: relative viscosity, normal stress differences and particle pressure are then presented for $0 \leq Re \leq 5$ and $0.05 \leq \phi \leq 0.3$. To our knowledge, such rheological data is not available in the liturature. In the subsequent sections, a statistical description of suspension at microscale is provided by the microstructural study using the pair distribution function. The structural aniosotropy at elevated particle fractions and inertia facilitate the understanding of normal stresses.

The last chapter is devoted to the development of a continuum description of particulate two-phase flows under the influence of inertia. We propose a new constitutive stress law and introduce the lift force associated with lateral migration to include the finite Reynolds number effects. The proposed model is then used to solve for the particle concentration and the velocity profiles in a pressure-driven flow of dense suspensions.

Finally, it should be noted that most chapters are self-contained and have been (or will be) published as papers in scientific journals. A couple of minor changes have been made to make the thesis more comprehensible.

Chapter 2

Lattice-Boltzmann Method

2.1 Development of a 3D lattice-Boltzmann model

The solution of the combined particle motion and fluid flow problem is obtained by the lattice-Boltzmann technique. We use the approach of Ladd & co-workers [54, 64, 56, 57] for the lattice-Boltzmann method (LBM) to model the fluid motion in this work.

The LBM when applied to a suspension combines Newtonian mechanics for the solid particles with a discretized Boltzmann model for the fluid. The fluid phase is discretized in space and time and is taken to be made of fictitious particles (or 'LB particles') which are constrained to move on a regular lattice. The state of the system is characterized by the one-particle velocity distribution function $n_i(\boldsymbol{r}, t)$, which describes the number density of the LB particles moving with discrete velocity $\boldsymbol{c}_i$ at a lattice node $\boldsymbol{r}$ at time t. We have used the three-dimensional, 19-velocity, or D3Q19 [see figure 2.1, velocity model in which a particle can either rest or move to the nearest (directly along a lattice direction, e.g. [100]) or diagonally next nearest (e.g. [110]) neighboring node of a cubic lattice [57]. The mass density ρ, momentum density $\boldsymbol{j} = \rho\boldsymbol{u}$ and the momentum flux $\boldsymbol{\Pi}$ are defined by moments of the velocity

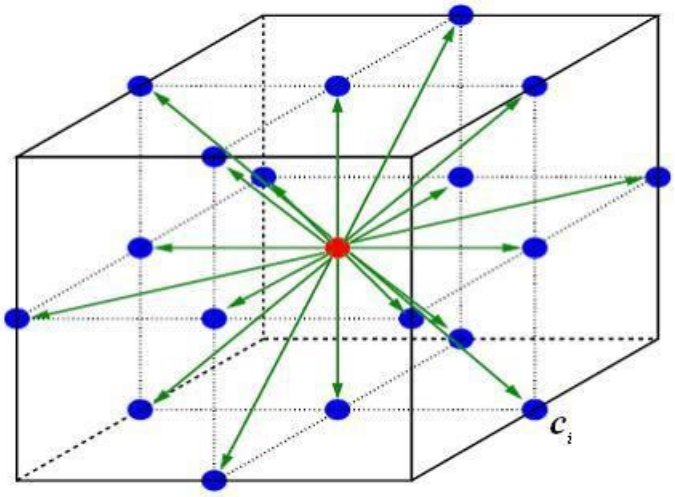

Figure 2.1: D3Q19 velocity model.

distribution function

$$\rho = \sum_i n_i, \qquad \boldsymbol{j} = \sum_i n_i \boldsymbol{c}_i, \qquad \boldsymbol{\Pi} = \sum_i n_i \boldsymbol{c}_i \boldsymbol{c}_i. \tag{2.1}$$

The lattice-Boltzmann equation for the evolution of $n_i(\boldsymbol{r}, t)$ is written as [54, 65, 66]

$$n_i(\boldsymbol{r} + c_i \Delta t, t + \Delta t) = n_i(\boldsymbol{r}, t) + \sum_j \Omega_{ij} n_j^{neq}, \tag{2.2}$$

where Δt is the time step and the collision operator Ω_{ij} describes the change in n_i due to collisions. The non-equilibrium distribution function is defined as $n_i^{neq} = n_i - n_i^{eq}$. The general form of equilibrium distribution is chosen to recover the Navier-Stokes equations for low Mach number flows ($Ma = u/c_s << 1$, where $c_s = \sqrt{1/3}$ is the speed of sound in lattice units) and can be written to $O(u^2)$ as [57]

$$n_i^{eq} = a^{c_i}[\rho + \frac{\boldsymbol{j} \cdot \boldsymbol{c}_i}{c_s^2} + \frac{\rho \boldsymbol{u}\boldsymbol{u} : (\boldsymbol{c}_i \boldsymbol{c}_i - c_s^2 \boldsymbol{I})}{2c_s^4}], \tag{2.3}$$

where $\boldsymbol{I}$ is the identity tensor and a^{c_i} are the coefficients of three speeds $0, 1$ and $\sqrt{2}$

associated, respectively, with LB particles remaining at the same node, moving to a nearest neighbor, or moving to a next-nearest neighbor. At equilibrium the density of LB particles moving in the [100] direction is twice that for the [110] direction and hence the coefficients, obtained from conservation constraints, are given by $a^0 = \frac{1}{3}, a^1 = \frac{1}{18}$, and $a^{\sqrt{2}} = \frac{1}{36}$. The post-collision distribution $n_i^*(\boldsymbol{r}, t)$ is written as a series of moments,

$$n_i^* = a^{c_i}[\rho + \frac{\boldsymbol{j} \cdot \boldsymbol{c}_i}{c_s^2} + \frac{(\rho \boldsymbol{u}\boldsymbol{u} + \boldsymbol{\Pi}^{neq,*}) : (\boldsymbol{c}_i \boldsymbol{c}_i - c_s^2 \boldsymbol{I})}{2c_s^4}]. \tag{2.4}$$

In the collision process mass and momentum remain conserved but the non-equilibrium momentum flux changes according to

$$\boldsymbol{\Pi}^{neq,*} = (1 + \lambda)\bar{\boldsymbol{\Pi}}^{neq} + \frac{1}{3}[1 + \lambda_v(\boldsymbol{\Pi}^{neq} : \boldsymbol{I})]\boldsymbol{I}. \tag{2.5}$$

where λ and λ_v are eigenvalues of the collision operator and are related to the shear and bulk viscosities. After the collision, the population densities are streamed to the neighboring node along velocity link $\boldsymbol{c}_i$.

The collision operator can be further simplified by assuming that the particle distribution function relaxes to its equilibrium state at a constant rate as

$$\Omega_{ij} = -\frac{1}{\tau}\delta_{ij}, \tag{2.6}$$

where τ is the relaxation time. This reduces equation (1.2) to

$$n_i(\boldsymbol{r} + c_i \Delta t, t + \Delta t) = n_i(\boldsymbol{r}, t) - \frac{1}{\tau}(n_i - n_i^{eq}). \tag{2.7}$$

This form of lattice-Boltzmann equation is called as a lattice BGK (Bhatnagar-Gross-Krook) equation. Because of its simplicity it has become the most popular form of

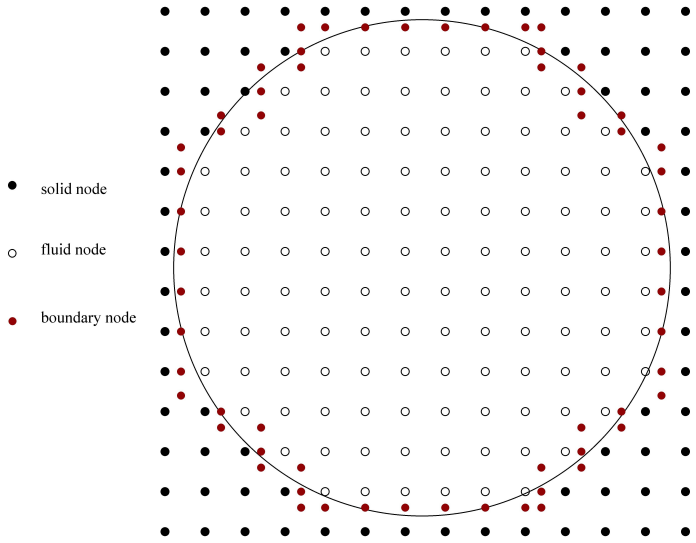

Figure 2.2: Mapping of a circular particle onto a square lattice.

collision operator in addressing particulate suspension [56, 67, 61].

External force density such as pressure gradient or gravitational field can be incorporated by applying a uniform force density $\boldsymbol{f}$ to the fluid. The LB equation is then modified as

$$n_i(\boldsymbol{r} + c_i\Delta t, t + \Delta t) = n_i(\boldsymbol{r}, t) + \sum_j \Omega_{ij} n_j^{neq} + f_i(\boldsymbol{r}, t) \tag{2.8}$$

2.2 Solid-fluid boundary conditions

In the LBM, solid particles are discretized in space and are defined by a surface that cuts some links between lattice nodes [see figure 2.2]. Following Aidun *et al.* [56], the fluid is removed from the interior of the particle. To implement solid-fluid boundary conditions the "link-bounce-back" rule, in which the boundary nodes are located midway between the solid and the fluid nodes, is applied. The population

densities of the fluid nodes just outside the solid surface are modified such that the fluid velocity is matched to the local solid velocity. We consider a set of fluid nodes at position defined by $\boldsymbol{r}$ and for each node all the velocities $\boldsymbol{c}_i$ such that $\boldsymbol{r} + \boldsymbol{c}_i \Delta t$ lies inside the particle surface. If $\boldsymbol{r}_b = \boldsymbol{r} + \frac{1}{2}\boldsymbol{c}_i \Delta t$ is a point inside the particle moving with translation $\boldsymbol{U}$ and angular speed $\boldsymbol{\Omega}$, then its velocity is

$$\boldsymbol{u}_b = \boldsymbol{U} + \boldsymbol{\Omega} \times (\boldsymbol{r}_b - \boldsymbol{R}), \tag{2.9}$$

where $\boldsymbol{R}$ is the center of mass of the particle. The population density is updated by

$$n_{-i}(\boldsymbol{r}, t + \Delta t) = n_i^*(\boldsymbol{r}, t) - \frac{2a^{c_i}\rho_0 \boldsymbol{u}_b \cdot \boldsymbol{c}_i}{c_s^2}, \tag{2.10}$$

where $-i$ denotes the velocity $\boldsymbol{c}_{-i} = -\boldsymbol{c}_i$. In this update momentum is exchanged between the solid and fluid particle, but the combined momentum is conserved. The force exerted at the boundary node is given by

$$\boldsymbol{f}_b(\boldsymbol{r}_b, t + \frac{1}{2}\Delta t) = \frac{\Delta x^3}{\Delta t}[2n_i^* - \frac{2a^{c_i}\rho_0 \boldsymbol{u}_b \cdot \boldsymbol{c}_i}{c_s^2}]\boldsymbol{c}_i, \tag{2.11}$$

where Δx is the lattice spacing. By summing over all the boundary nodes $\boldsymbol{r}_b$, we obtain the total force and torque acting on the particle as

$$\boldsymbol{F} = \sum_{\boldsymbol{r}_b} \boldsymbol{f}_b, \quad \text{and} \quad \boldsymbol{T} = \sum_{\boldsymbol{r}_b} \boldsymbol{f}_b \times \boldsymbol{r}_b. \tag{2.12}$$

The particle positions and velocities are then updated.

Since a suspended particle is represented discretely, it samples different numbers of nodes as it moves, and hence there is an effective hydrodynamic radius r_h which is greater than the prescribed radius a. This r_h depends only on a and fluid viscosity

[57]. As the particle becomes large, the difference between r_h and a grows small; r_h is calibrated by calculating the drag coefficient of a sphere in the Stokes flow regime [64].

2.3 Lubrication correction

An important part of the hydrodynamic interaction of two spheres involves near-field lubrication stresses, particularly due to squeeze flow associated with motion of a pair approaching contact along the line of centers. Though LBM can capture hydrodynamics down to one lattice spacing, the grid resolution may become insufficient to resolve the flow in the gap. To overcome this problem, [58] proposed the following normal force be added between the two spheres,

$$\boldsymbol{F}_{lub} = -\frac{6\pi\mu(ab)^2}{(a+b)^2}\hat{\boldsymbol{r}}\hat{\boldsymbol{r}}\cdot\boldsymbol{U}_{21}(\frac{1}{h}-\frac{1}{h_c}) \tag{2.13}$$

where a and b are the radii of the spheres, $\boldsymbol{r} = \boldsymbol{x}_2 - \boldsymbol{x}_1$ for particles centered at $\boldsymbol{x}_1$ and $\boldsymbol{x}_2$ with $\hat{\boldsymbol{r}} = \frac{\boldsymbol{r}}{|\boldsymbol{r}|}$, and $\boldsymbol{U}_{21} = \boldsymbol{U}_2 - \boldsymbol{U}_1$ is the relative velocity of the pair. The gap $h = |\boldsymbol{r}| - 2a$ (or $h = |\boldsymbol{r}| - a - b$ for unequal sizes) is between the points of closest approach of the surfaces with h_c a cut off for the added lubrication force: for gaps larger than h_c, $F_{lub} = 0$, and this cut off h_c is set empirically as $2/3$ of the lattice spacing.

The stresslets [see chapter 5] due to close-pair ($\boldsymbol{S}^{p-p}$) and particle-wall interactions ($\boldsymbol{S}^{p-w}$) are computed similarly by making use of the asymptotic forms of hydrodynamic interaction functions as tabulated in Kim & Karrila [68], with greater details

available in Nguyen & Ladd [58]. The total particle stresslet is then given by

$$\boldsymbol{S_i} = \boldsymbol{S}_i^0 + \boldsymbol{S}^{p-p} + \boldsymbol{S}^{p-w}. \tag{2.14}$$

Chapter 3

Pair-sphere trajectories in finite-Reynolds-number shear flow

3.1 Introduction

Suspension mechanics is based in large part upon understanding the hydrodynamic interactions between particles suspended in viscous fluid. For simplicity the particles considered are usually spherical. Hence, the relative motion of spheres is central to the study of suspension mechanics. Batchelor & Green [5] studied this problem for a pair of neutrally-buoyant spheres moving freely – that is, experiencing zero force and zero torque – in a linear Stokes flow. This work followed a body of studies which considered the specific case of hydrodynamic interaction of two spheres immersed in an ambient shear field [69, 70, 71, see for example]. The results of this work, directly and through formal extension to a system of hydrodynamic functions computed to high accuracy [7, 8, 10], provide the basis for not only analytical studies [13, 14, 72], but also for simulation tools such as Stokesian Dynamics [11] and related approaches [73] which address many particles at a wide range of solid fraction. Darabaner & Mason [74] experimentally addressed the hydrodynamic interaction of two spheres of equal as well

This chapter is published as *Pair-sphere trajectories in fintie-Reynolds-number shear flow*, P. M. Kulkarni and J. F. Morris, J. Fluid Mech. **596**, pp. 413-435 (2008)

as unequal size suspended in a circular Couette flow at low particle Reynolds number of $O(10^{-6})$. Darabaner & Mason showed that, depending on the separation between the two spheres, they will either orbit around each other (permanent collision) or separate, a result in agreement with the analysis of Batchelor & Green [5].

Viscous suspensions have thus been well-studied and there is now a body of understanding of their behavior, including the transport properties of rheology and self-diffusion, as well as such bulk flow phenomena as shear-induced migration. As a model two-phase material, the Stokes-flow suspension has played a valuable role in development of the study of mixture flow. However, progress in understanding of mixture flow at finite inertia has been slow [47]. New computational techniques have recently made examination of motions of interacting particles at finite Reynolds number feasible. Because of the computational costs involved, the conventional CFD methods such as finite element applied to the particle-laden flow [75, 76, 77] have to date largely examined 2-dimensional particle-laden flows with finite inertia [78, 50], with sedimentation the most commonly considered flow. Three-dimensional problems studied include the settling ellipsoid in a tube with boundary interactions accounted [49]. There is associated with the FEM the requirement of remeshing the fluid as the structure evolves, and the extremely small surface separations to which particles are driven in shear flow magnify this problem. We choose to work with the lattice-Boltzmann method (LBM) as developed for particulate flows [54, 64, 56, 57]. In this method, the particles move on a fixed mesh, which simplifies the problem relative to FEM, while allowing simulation of finite inertia fluid motion and thus providing capability not available in Stokesian Dynamics. The spatial locality of the lattice-Boltzmann equation, and the fixed grid provide ease of parallelization. A potential disadvantage of the LBM method is that because of its formulation it allows finite compressibility of the fluid, as discussed in chapter 2, and care must be taken when

simulating incompressible motions to ensure that the influence of compressibility is small. We present quantitatively the effect of finite compressibility on our results in § 3.4.1.

The problem addressed here is that of determining the relative motion of pairs of spheres in finite-Reynolds-number shear flow. Only the case of neutrally-buoyant particles will be considered. The Reynolds number characterizing the fluid inertia in shear is given by $\rho\dot{\gamma}a^2/\mu$, where a is the particle size (taken as the radius for a sphere), μ and ρ are the viscosity and density of the fluid, respectively, and $\dot{\gamma}$ is the shear rate. The particles, being of equal density to the fluid, have similar inertia to the fluid. However, we emphasize that Re is related to fluid inertia to distinguish it from the Stokes number, which may be written $St = (\rho_p/\rho)Re$ using ρ_p to denote the density of the particle; St characterizes particle inertia. Only recently has there appeared work addressing the influence of inertia on the relative motion of particle pairs in shear flow, and all of the work of which we are aware has considered cases different from the present study. This recent work is numerical and we know of no experiments addressing the issue, although the influence of finite-inertial hydrodynamic interactions has been suggested to play a role in experimentally-observed formation of chain-like structures in dilute pressure-driven suspension flow in a pipe by [79], a phenomenon replicated in square duct flow simulations [80]. The numerical work noted includes the case of $St > 0$ and $Re \equiv 0$ studied by [81] while $St > Re > 0$ was considered by [60]. Subramanian & Brady used well-known hydrodynamic interaction functions to determine the hydrodynamic force and torque on particles with finite values of St, corresponding perhaps to solid particles in gas, and observed a rich set of new features including limit cycles in the

Subramanian & Brady used $St^* = 2St/9$ and the same Re as presented in this work, but we prefer the definition of Stokes number given here as it indicates excess particle inertia if St exceeds Re, whereas the equivalent physically significant condition is found when $St^* > 2Re/9$.

pair trajectory space relative to the zero Re-zero St condition. The Kromkamp *et al.* study considered two-dimensional (2D) circular cylinders at $0 < Re \leq 0.51$, with $\rho_p/\rho = 3$ and 10 yielding $St = 3Re$ or $10Re$. The combined influence of fluid inertia and excess particle inertia (i.e. $St > Re$) results in behavior which differs from the neutrally-buoyant case examined in this study. Because the conditions of both the Subramanian & Brady and the Kromkamp *et al.* studies involved heavy particles, gravity was neglected in their work. Here, we study the case of neutrally-buoyant particles because it seems the first natural case to examine in order to isolate the role of inertia in shear-induced hydrodynamic interactions, and furthermore because the conditions are experimentally realizable in normal gravity.

The fluid flow around a single sphere in simple-shear flow at finite inertia has been studied analytically [45], experimentally [41] and numerically ([82] by finite volume; [42] by finite element). An important aspect of the flow characteristics of this simplest system was missed in these prior studies, as shown by the recent analysis of [43, 44]. These authors showed that the streamline topology at finite Re changes qualitatively from that at $Re = 0$. In particular, the fluid elements close to the freely-rotating sphere spiral outward rather than forming a closed streamline region. This leads to the prediction that the suspended particles significantly enhance heat and mass transfer, by introducing a convective mechanism rather than diffusion through the closed-streamline zone. We apply the lattice-Boltzmann method to gain further insight into the finite-Re streamline pattern around a single sphere in support of the primary goal of understanding pair-sphere trajectories in shearing flows. Pair trajectories at small Re are found to be similar in their structure, even for equal sized spheres, to the streamlines around the single sphere.

In § 3.2, we define the problem and present a brief outline of the methods used in our study. We then present our simulation results, examining the streamlines around

a single sphere (§ 3.3) and pair trajectories of spheres (§ 3.4) in simple-shear flow at finite inertia.

3.2 Problem statement and solution method

3.2.1 Governing equations

Our interest is in the motion of neutrally-buoyant solid spherical particles suspended in a Newtonian fluid subjected to simple-shear flow with finite fluid inertia. The governing equations in non-dimensional form for the fluid phase are

$$\boldsymbol{\nabla} \cdot \boldsymbol{u} = 0 \tag{3.1a}$$

$$Re(\frac{\partial \boldsymbol{u}}{\partial t} + \boldsymbol{u} \cdot \boldsymbol{\nabla} \boldsymbol{u}) = -\boldsymbol{\nabla} p + \nabla^2 \boldsymbol{u} \tag{3.1b}$$

where length has been made dimensionless with the radius of the sphere a, time by the inverse of the shear rate $\dot{\gamma}^{-1}$, fluid velocity by $\dot{\gamma} a$, and the pressure by $\mu\dot{\gamma}$. The shear flow Reynolds number is defined as $Re = \rho\dot{\gamma}a^2/\mu$, where μ and ρ are, respectively, the viscosity and density of the fluid. Particle translations ($\boldsymbol{U}_i$) and rotations ($\boldsymbol{\Omega}_i$) are governed by Newtonian dynamics,

$$m_i \frac{\partial \boldsymbol{U}_i}{\partial t} = \boldsymbol{F}_i \tag{3.2a}$$

$$I_i \frac{\partial \boldsymbol{\Omega}_i}{\partial t} = \boldsymbol{T}_i, \tag{3.2b}$$

where the net force $\boldsymbol{F}_i$ and net torque $\boldsymbol{T}_i$ act on the particle i, which has mass and moment of inertia m_i and I_i, respectively. We shall focus on the relative motion of a pair of neutrally-buoyant spherical particles, with certain results presented for a single sphere to facilitate understanding of the pair problem.

3.2.2 Limiting behavior: Stokes solutions

Before proceeding to the solution method, we recall the well-known limiting behavior obtained analytically at $Re = 0$ for the isolated sphere and a pair of equally sized spheres. At $Re = 0$, the flow field around a sphere suspended in simple shear flow may be obtained analytically via superposition of vector harmonic functions [3]. The velocity field in the fluid around the sphere is given by [42] as

$$u_x = \frac{1}{2}y(1-r^{-5}) + \frac{1}{2}y(1-r^{-3}) - \frac{5}{2}x^2y(r^{-5}-r^{-7}) - \frac{\Omega y}{r^3} \tag{3.3a}$$

$$u_y = \frac{1}{2}x(1-r^{-5}) - \frac{1}{2}x(1-r^{-3}) - \frac{5}{2}y^2x(r^{-5}-r^{-7}) + \frac{\Omega x}{r^3} \tag{3.3b}$$

$$u_z = -\frac{5}{2}xyz(r^{-5}-r^{-7}). \tag{3.3c}$$

If the sphere rotates freely (zero torque), it has steady angular velocity, made dimensionless with $\dot{\gamma}$, of $\Omega = 1/2$, matching the vorticity of the undisturbed flow. The inertialess streamline configuration around the freely-rotating sphere is shown in figure 3.1*a*. The flow is characterized by a region of closed streamlines which extends infinitely in both the flow and vorticity directions. Outside this closed streamline region, open streamlines begin from upstream infinity, and proceed past the particle to downstream infinity – for example beginning from $(x \to -\infty, y > 0)$ and proceeding to $(x \to \infty, y > 0)$. The streamline form is mirrored through the plane $y = 0$. All streamlines, whether open or closed, also have fore-aft symmetry about the plane $x = 0$, owing to the linearity and reversibility of the Stokes equations.

The relative trajectories of a pair of particles in Stokes flow have a number of similarities to the streamlines around an isolated sphere. Two spherical particles suspended freely in simple-shear flow at $Re = 0$ follow one of two kinds of pair trajectories. These are illustrated for equally-sized spheres in figure 3.1*b*. One type

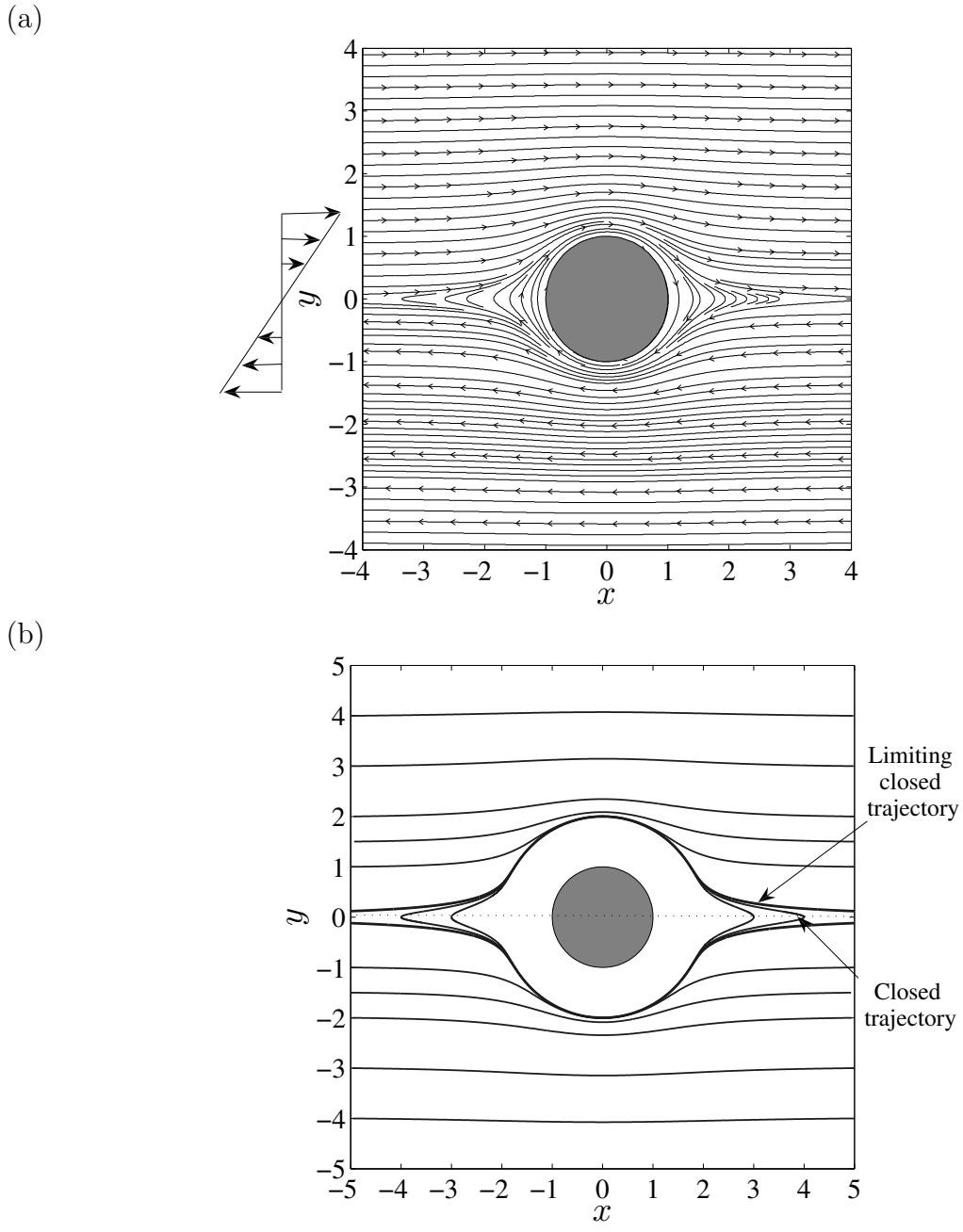

Figure 3.1: (a) Streamline configuration around a freely-rotating sphere in simple-shear flow at $Re = 0$. (b) Pair trajectories of two force-free spheres in simple-shear flow at $Re = 0$ obtained from analytical solution of Batchelor & Green [5]: The curves describe the motion of a second sphere relative to the origin instantaneously fixed at the center of the first (as indicated by the gray circle at the origin). For both (a) and (b) shear flow of form $u_x = \dot{\gamma} y$ is as indicated in (a).

are the 'open' trajectories in which one particle starts far upstream with an offset in the gradient direction, approaches and passes over the other particle and returns to the same offset far downstream. The second are 'closed' trajectories in which the particles are captured in permanent orbits around each other. The region occupied by the closed trajectories has infinite volume [5]. Nonetheless, the set of closed trajectories are compressed to a very narrow band where the pair separation is only slightly greater than two radii on closest approach, as seen in figure 3.1*b*. A closed surface, symmetric about the planes $x = 0$ and $y = 0$, separates these two regions in trajectory space; the same symmetries about these planes hold for all pair trajectories in Stokes flow. The open and closed trajectories are found for arbitrary size ratio of the two spheres, i.e. a and $b \neq a$, and in the limit of $b/a \ll 1$ the smaller sphere should asymptotically follow the fluid motion around an isolated sphere. There is thus a continuous variation from the streamline about a single sphere to the trajectory of a pair of equal sized spheres.

3.3 Single particle at finite Re

It has recently been shown that for a single sphere rotating freely in simple-shear flow, the closed streamline structure present at $Re = 0$ is destroyed by weak inertia [43, 44]. The fluid elements close to the sphere spiral around it before departing the vicinity of the sphere to proceed "downstream." As shown below, the exit of the vicinity of the particle can be in either of the two possible directions associated with the shear flow $u_x = y$ depending upon which streamline is considered, i.e. there is an interlacing of streamlines which depart in the two directions. The rate of spiraling depends upon the value of Re. Accompanying the spiraling motion, mass conservation demands a net flux of the fluid along the vorticity direction toward the sphere, and

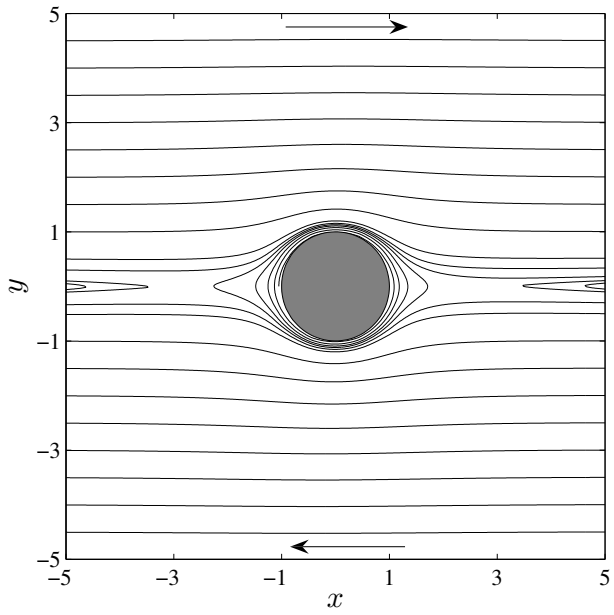

Figure 3.2: Computed streamline configuration in the plane of shear around a freely-rotating sphere in simple-shear flow at $Re = 0.1$.

these streamlines also spiral outward. Fluid outside the envelope of the spiraling region may either pass the body on an open streamline, or reverse its path; the reversal zone, discussed in detail by Mikulencak & Morris [42], is associated with small gradient direction offsets sufficiently far upstream of the body to be outside the spiraling streamline region. A similar picture prevails as one considers planes of constant z, i.e. progressing in the vorticity direction, although the cross-section in the local $x - y$ plane of the spiraling trajectories diminishes in size with increasing z. Streamlines in the plane of shear ($z = 0$), with the flow computed by the LBM, around a freely-rotating sphere at $Re = 0.1$ are shown in figure 3.2. Note that the streamlines near the body make circuits and then depart from the particle toward infinity, and that reversing streamlines are evident at the left and right of the figure.

As Re increases, the reversing region approaches the particle [42] and the spiraling region collapses. This behavior of the streamline pattern is quite similar to the case of a cylinder in two dimensional flow [39, 40]. However, in the 2D flow, the constraints of

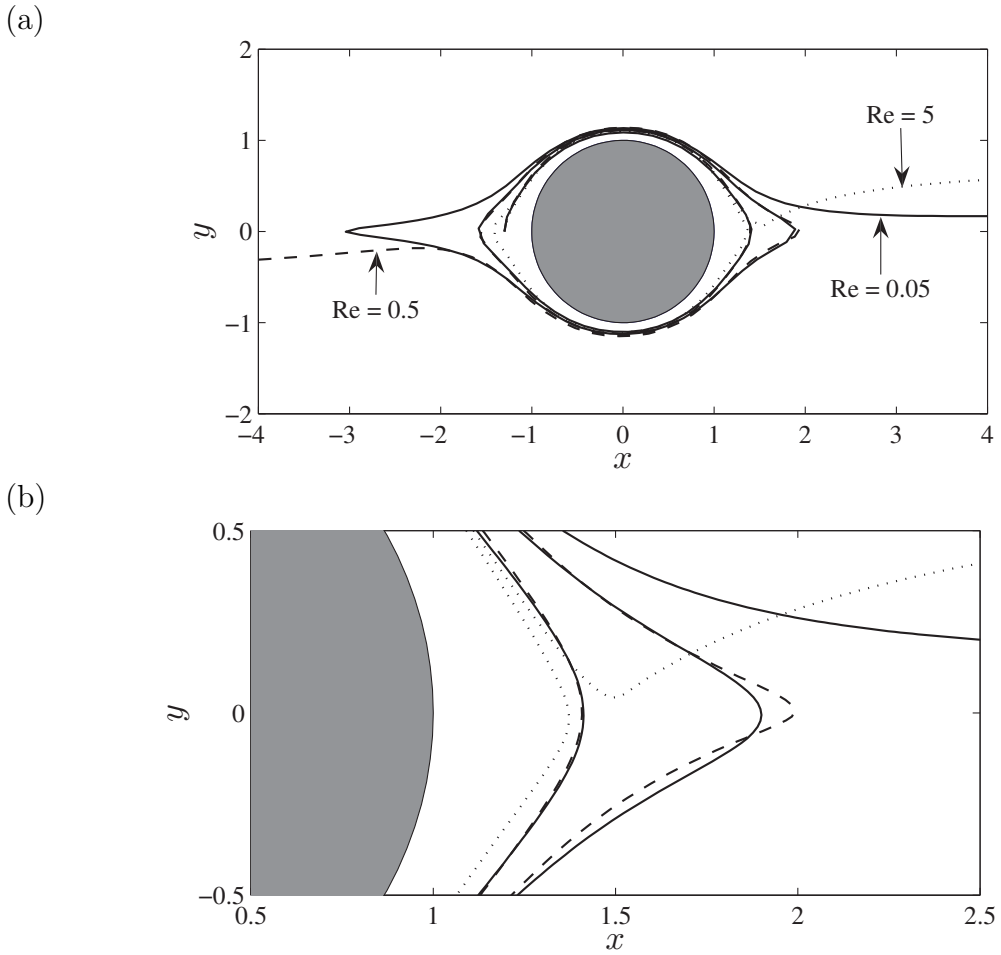

Figure 3.3: (a) Streamlines starting from (-1.3,0,0) for $Re = 0.05, 0.5$ and 5 in simple-shear flow around a freely-rotating sphere. (b) Expanded view of the region ($0.5 \leq x \leq 2.5, -0.5 \leq y \leq 0.5$).

symmetry and incompressibility ensure that the streamlines close to the cylinder are closed. We plot in figure 3.3 fluid streamlines starting from the same point, specifically $(x, y, z) = (-1.3, 0, 0)$, for $Re = 0.05$, 0.5 and 5. At lower Re, a fluid element makes more circuits around the sphere before it moves away permanently, and the direction of departure may be either left or right depending on the precise location of the initial point and the level of inertia. Figure 3.4 shows that the out-of-plane reversing (1) and open (2) fluid paths always tend to have a net displacement away from the shear plane while a spiraling streamline (3) comes closer to the shear plane before it departs the vicinity of the particle. Note that when they approach closely to the sphere, the spiraling paths have a portion on each circuit moving away from the sphere, but the net motion on a circuit is toward the body until the final circuit. On this final circuit, the net z-directed motion is slightly away from the body, and this will be echoed in the particle pair trajectories. The three-dimensional picture of the various forms of streamlines is illustrated in figure 3.5 for $Re = 0.5$, where single open, reversing, in- and out-of-plane spiraling fluid paths are plotted.

3.4 Pair trajectories at finite Re

Here, the aim is to determine the finite-Re trajectories of two spheres freely suspended in simple-shear flow. In most of the simulations discussed, two neutrally-buoyant spheres of equal radius a are placed symmetrically in a computation box of size $L \times H \times W$, as illustrated in the sketch of figure 3.6; in some instances, we consider unequal spheres of a and $b < a$. The shear flow is set by moving the top and bottom walls in opposite directions at equal speed. Periodic boundary conditions are applied in the flow and vorticity directions; as in the prior discussion, x, y and z denote the flow, gradient and vorticity directions of the undisturbed flow,

(a)

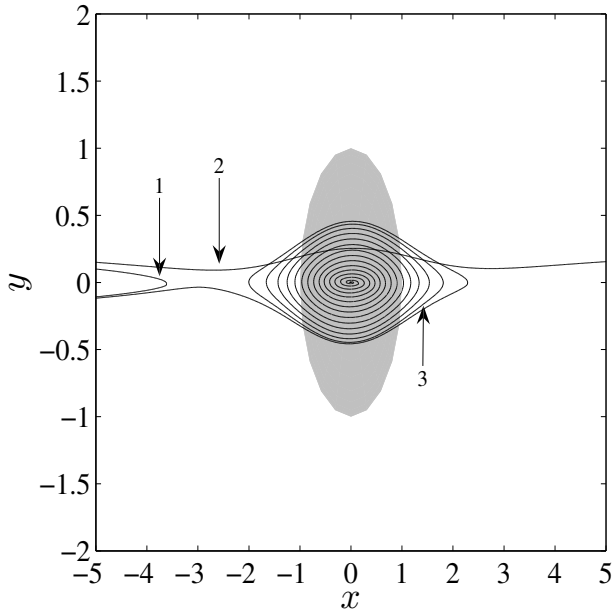

(b)

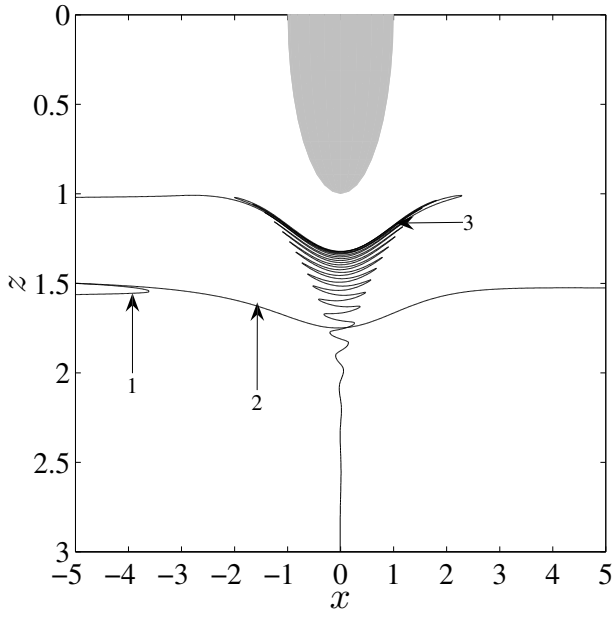

Figure 3.4: Off-plane fluid streamlines for $Re = 0.1$ around a freely-rotating sphere in simple-shear flow: (a) xy-projection (b) xz-projection. (1) Reversing streamline originating from $(-5, 0.1, 1.5)$. (2) Open streamline originating from $(-5, 0.15, 1.5)$. (3) Spiraling streamline originating from $(-0.01, 0, 3.0)$. The spherical particle is shown as a shaded ellipse because of the stretched y or z coordinate.

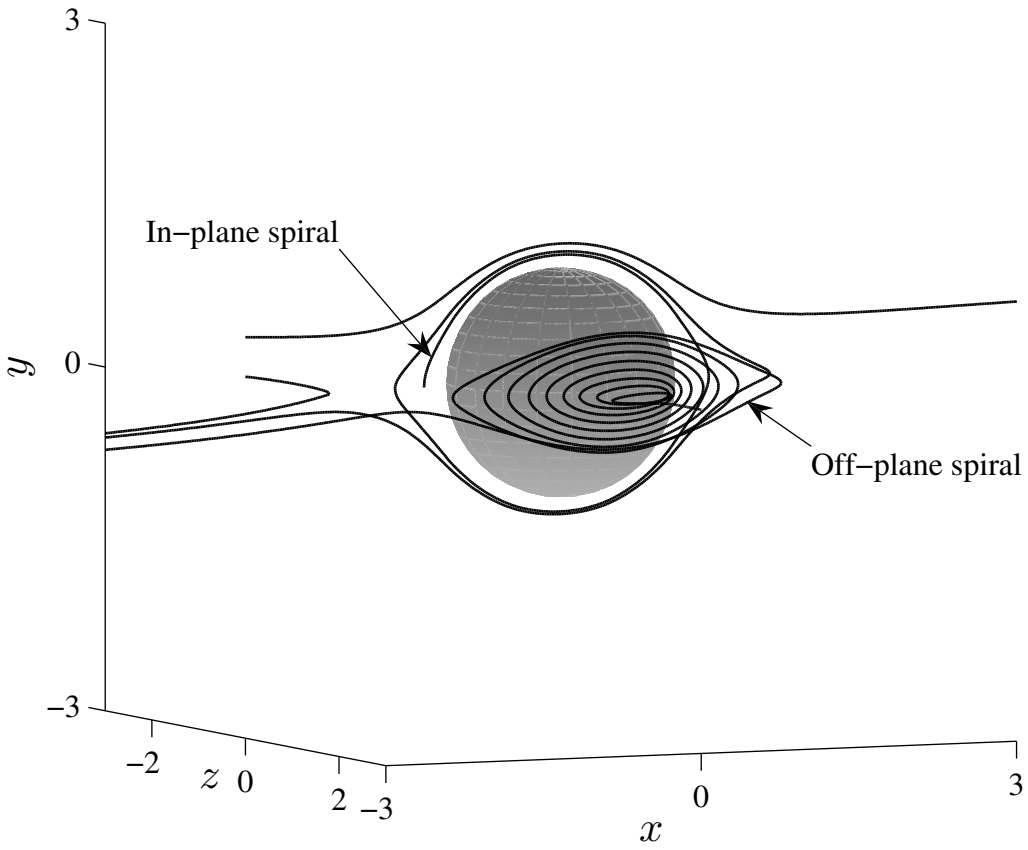

Figure 3.5: Three-dimensional streamline configuration around a freely-rotating sphere in simple-shear flow at $Re = 0.5$ obtained by the LBM. Single open and reversing streamlines are shown, with one in-plane and one out-of-plane spiraling streamline also illustrated.

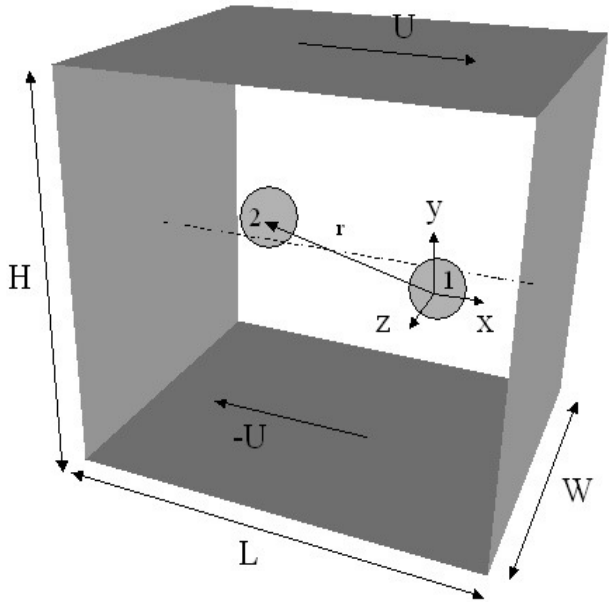

Figure 3.6: Sketch defining terms used in describing the pair-sphere motion in simple shear.

respectively. The spheres, initially separated by some displacement, are first allowed only to rotate until they achieve a steady flow field and are then released. The Mach number is defined $Ma = \dot{\gamma}H/(2c_s)$, where $\dot{\gamma}H/2$ is the wall velocity. We maintain $Ma < 0.1$ in order to minimize compressibility effects. The constraint may be written $Ma = (\mu Re)/(\rho c_s a) \times (H/a) < 0.1$, which means that one has to decrease viscosity of the fluid in order to increase Re for fixed a/H.

Primary interest here is in the role of fluid mechanical inertia upon the pair relative trajectory, and hence the shear Reynolds number Re is the key parameter determining the structure of the trajectory space. However, because we compute the motion in a periodic and wall-bounded domain, the nature of trajectories depends to some degree upon the domain size. Issues include the fact that walls suppress the rotation of a single particle in the shear flow by creating stronger flow reversal regions [83]; also, the particles interact with their periodic images, which gives rise to a dependence of trajectories on the size of the domain in flow and vorticity directions. Even in the

absence of inertia, the presence of nearby walls will cause flow reversal of streamlines for a single sphere and of the relative trajectory for a pair; this phenomenon has been examined for pair interactions by [84]. Results will be presented below which address the influence of domain size in our work.

We have chosen a mesh density of 6.2 lattice nodes per radius of the sphere, and a computational domain of $20a \times 20a \times 20a$. Results have been found qualitatively independent of increase in the density of the lattice. To sample the trajectory space, we vary the initial positions of the spheres, with the pair symmetrically placed (except in cases of unequal spheres) about the central point in the computational domain. We will usually describe the pair trajectories in terms of the time variation of the separation of the centers of the pair of spheres, $\boldsymbol{r}(t) = \boldsymbol{x}_2(t) - \boldsymbol{x}_1(t)$, with initial separation denoted by $\boldsymbol{r}_0 = (r_{0x}, r_{0y}, r_{0z})$.

Fluid inertia alters the topology of the trajectories of neutrally-buoyant particles relative to the Stokes flow results outlined in §3.2.2. The trajectory space transitions from having two regions (open and closed) at $Re = 0$ to three types at any finite Re. These three trajectory types mirror the form of the streamlines of the steady finite-Re flow around a sphere and will again be termed open, reversing and spiraling. The motion is, of course, unsteady. We outline here the general results to be detailed in the following.

The *open trajectories* at finite Re are largely similar to those predicted for Stokes flow, starting from upstream infinity and progressing in the x (streamwise) direction in the same sense at every point, with some deflection of the trajectory when the pair is close. The open trajectories form the majority of the pair space, because the other types require significant particle interaction. Note that this does not imply closely approaching pairs will not have open trajectories: as seen below, spheres of equal size may approach to surface separations below a percent of a radius on open trajectories.

The *reversing trajectories* are much like the reversing (termed recirculating by Subramanian & Koch (2006 a,b)) streamlines about a single sphere discussed in detail by [42]. A pair with an initial offset ($r_{0x} < 0, r_{0y} > 0$) will approach and then reverse their relative positions in y and hence reverse their relative motion in x to recede toward ($r_x < 0, r_y < 0$).

The *spiraling trajectories* are divided into the in-plane and out-of-plane trajectories depending upon whether the pair lie at the same or different z coordinates, respectively. For particles starting with a finite r_{0z} and lying near the vorticity axis (z), the pair approach one another along a path which spirals outward when projected onto the x–y plane, eventually leaving the mutual 'zone of influence' and moving away in x. For a pair lying at the same z, i.e. in the plane of shear, there is no z-directed motion because of the symmetry. There is a small region of pair space adjacent to contact in which the particles simply spiral around and away from one another, and then depart the close interaction. We note that the spiraling trajectory motion toward the shear plane is much like that of the fluid flow around a single sphere, where it is a requirement of mass conservation as material is being spun outward on and near the plane of shear and must be replaced by an inflow down the vorticity axis. The spiraling pair relative motion can thus be seen as an inertial hydrodynamic interaction driven by the centrifugal ejection of fluid in the equatorial plane region of the reference sphere.

Before we address the computational results, we present an argument which allows a fairly ready rationalization of the vanishing of closed trajectories for any $Re > 0$. This behavior may be seen as a direct consequence of the loss of fore-aft symmetry, known from single-sphere shear flow studies at finite inertia [45, 42, 43, 44], where the asymmetry is reflected in two diametrically opposed wakes in the downstream quadrants. As a result, streamlines which would form a closed circuit around a

freely-rotating sphere at $Re = 0$ and thus must cross the $y = 0$ plane at the same distance from the sphere (at say $\tilde{x}$ and -$\tilde{x}$), will at small Re suffer a slight streamwise displacement at each passing by the sphere. Because of the antisymmetry of the velocity on reflection through the origin, namely $\boldsymbol{u}(\boldsymbol{x}) = -\boldsymbol{u}(-\boldsymbol{x})$, a similar behavior will occur at the next passage of the fluid element around the rotating sphere – the result of this is an outward spiral. Similarly, at small Re a pair will have a fore-aft asymmetric interaction; even if the trajectories make circuits, these will cross the $y = 0$ plane at progressively larger values until the pair spiral away to infinite separation.

3.4.1 Finite Re trajectories in the shear plane

We begin by considering particles of equal size confined to the shear plane, $z = 0$. If the two particles start with large initial separation in x and y, only open and reversing trajectories will be observed. Figure 3.7 illustrates the nature of in-plane trajectories at $Re = 0.1$, beginning with small r_{0y} and $r_{0x} = -9.7$, i.e. a separation of almost ten radii in the streamwise direction. In this case, we illustrate both particle trajectories, with x_i and y_i denoting the coordinates of particle i ($i = 1$ or 2). The observed bumpiness in the trajectories is related to the mesh density of the sphere and resulting perturbations in the flow field due to the uncovering of the solid nodes as the particles move.

For a given Re, there is a critical gradient displacement, r_{0y}^c, that separates the two types of configurations. In the case of an open trajectory, the particles show evidence of fluid inertia, as there is a local deflection toward the zero-velocity ($y = 0$) plane upon close approach, and a net positive displacement in the gradient direction ($\Delta y > 0$) through the complete interaction which depends on r_{0y}: for smaller $r_{0y} > r_{0y}^c$, the

particles come closer and experience a greater net displacement Δy. It is of interest to note that [60], in 2D simulations, found a net displacement of the opposite sign, i.e. $\Delta y < 0$, for pairs interacting on open trajectories for $St > Re > 0$; Subramanian & Brady (2006) considered $Re = 0$ and finite St and found a negative gradient displacement scaling as $St^{1/2}$ for small St. These results both lead to the conclusion that approaching particles at elevated inertia relative to the surrounding material, *i.e.*, $St > Re$, reach smaller separations when resisted only by viscous stresses, and considering the results of the Stokes pair trajectory of figure 3.1*b*, it is natural that they exit the interaction at a smaller y displacement than they had upstream of the interaction.

A closer examination of the trajectory asymmetry is made by considering the separation between sphere surfaces $(|\boldsymbol{r}| - 2a)/a$. These are plotted against the x coordinate of the particle 2 in a frame fixed on particle 1 in figure 3.8 for three open trajectories. The closeness of approach leads to concern that the key feature of the gradient offset may be due to inaccurate computation of the lubrication force. However, for trajectory 1 the surface separation between the particles remains greater than 0.7 lattice units, so that modeled lubrication forces do not become active in the simulation of the motion. This trajectory is the least asymmetric of the three but shows a gradient offset nonetheless, and the lack of lubrication indicates that fluid inertia is responsible for the asymmetry.

Upon increasing the Reynolds number, keeping all other parameters fixed, r^c_{0y} increases: there is a larger region of reversing pair trajectories as Re increases, and this is consistent with the region of reversal approaching the particle more closely with increasing Re [42]. To illustrate the implications of increasing Re for this region of trajectory bifurcation, trajectories for $Re = 0.1$ and 0.2 initiated at the same three positions are shown in figure 3.9 for three cases. Hereafter, results are presented in

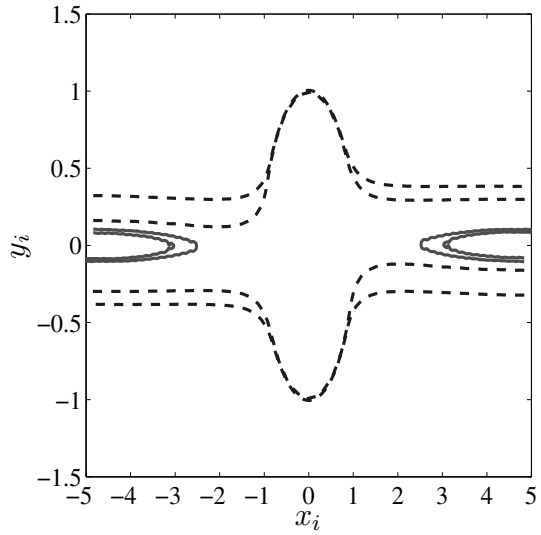

Figure 3.7: In-plane trajectories of a pair of equal-sized spheres of radius 1 in simple-shear flow at $Re = 0.1$ starting at the same streamwise but different gradient separations. Open trajectories are denoted by dashed lines and reversing by solid lines. Note that, in this figure the frame of reference is fixed at the center of computation box to get the idea of motion of the two particles.

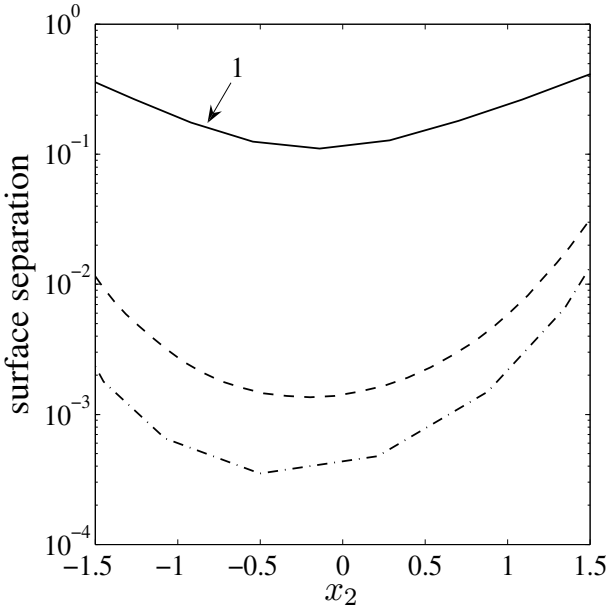

Figure 3.8: Surface separation $((|\boldsymbol{r}| - 2a)/a)$ between the spheres for different open trajectories at $Re = 0.1$. The trajectory labeled 1 does not involve modeled lubrication (surface separation $> 2/3$ lattice spacing) while the others do.

the relative form, $\boldsymbol{r} = \boldsymbol{x}_2 - \boldsymbol{x}_1$; the figure shows the reference particle 1 as a shaded elliptical region because of the stretching of the y coordinate. When particle 2 starts at A, $\boldsymbol{r}_0 = (-9.7, 0.65, 0)$, the higher Re trajectory brings it closer to the x axis before it passes over the reference particle. For the particle starting at B, $\boldsymbol{r}_0 = (-9.7, 0.3, 0)$, this tendency to move toward the x axis is carried to the point of a flow reversal: at $Re = 0.1$ this initial condition lies on an open trajectory, while at $Re = 0.2$ it lies on a reversing trajectory. The particle starting at C, $\boldsymbol{r}_0 = (-9.7, 0.2, 0)$, with $Re = 0.1$ travels a greater horizontal distance before it reverses its direction than does the $Re = 0.2$ particle. It should be noted that the stagnation point associated with closest approach of a pair exhibiting trajectory reversal is found closer to contact with increasing Re [41, 42]. The trajectories emanating from point C do not contradict this point, but there is potential for confusion. The reader should note that the width in y of the reversal zone at a given r_x increases with Re and this brings trajectories closer to contact as Re increases; comparing the B trajectory at $Re = 0.2$ with the C trajectory at $Re = 0.1$ helps in seeing this point. This is further illustrated in figure 3.9*b*, where we plot the trajectory-bifurcation point r^c_{0y} with Re for $x = -9.7$. The error bar indicates the numerical precision in the measurement of r^c_{0y}. The value of r^c_{0y} increases roughly as $Re^{0.3}$ for $Re = 0.01$ - 1, but for $Re \leq 0.01$ wall effects start to affect the nature of trajectories and for $Re > 0.5$, trajectories are increasingly influenced by the periodic images of the particles.

As noted, the boundaries may play a role in generating reversing trajectories even in Stokes flow as shown in [84], and may also alter the rotation rate of a single particle at finite Re [83, 85, 42]. To assess the influence of the walls, we performed simulations with $H = 30$ (nondimensionalized by radius of the sphere a) rather than 20 at $Re = 0.1$, keeping other parameters constant and found that the trajectories were indistinguishable. With an increase in size of the computation box in the flow

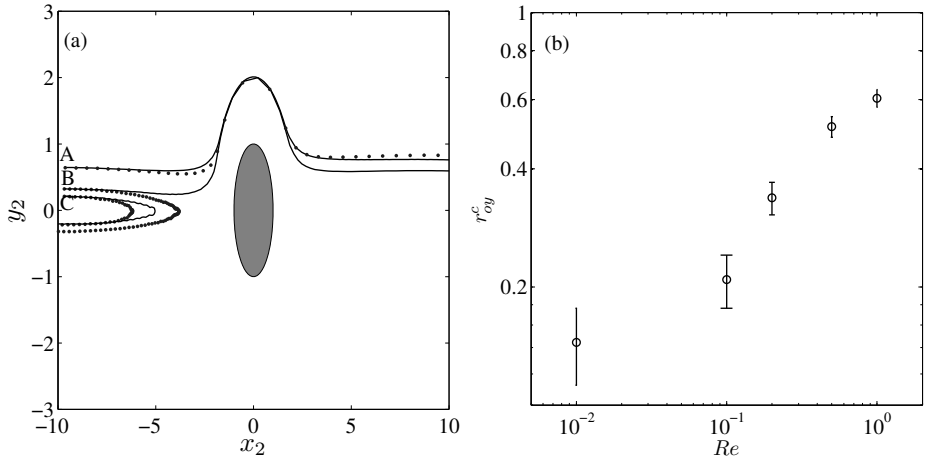

Figure 3.9: (a) In-plane trajectories of a pair of equal-sized spheres of unit radius in simple-shear flow at $Re = 0.1$ (solid lines) and $Re = 0.2$ (dotted lines). A trajectory for each of the two Re commences from A, $\boldsymbol{r}_0 = (-9.7, 0.65, 0)$; B, $\boldsymbol{r}_0 = (-9.7, 0.3, 0)$; and C, $\boldsymbol{r}_0 = (-9.7, 0.2, 0)$. (b) Log-log plot of the trajectory-bifurcation point r^c_{0y} separating open and reversing trajectories with Re for $x = -9.7$.

direction to $L = 30$, r^c_{0y} increases, but the qualitative picture remains the same. With an increase in the domain size in the vorticity direction to $W = 30$, the trajectories are found to be unchanged.

Compressibility is inherent in the LB method as employed here and its influence upon our results was checked by simulation of a single particle and a pair of particles in simple-shear flow at various Mach numbers $0.007 \leq Ma < 0.3$. As a technical matter, note that to vary Ma while keeping Re and a/H fixed, it is necessary to change the viscosity of the simulated fluid. The case of a single particle at $Re = 0.1$ is considered in figure 3.10a. The difference velocity in the flow direction is defined $\Delta u_x = u_x(Ma = 0.0225) - u_x(Ma)$ and values of $Ma = 0.045$, 0.135, and 0.27 are considered; the difference velocity along a line passing through the center of the particle, $\Delta u_x(x = 0, y, z = 0)$ is plotted (for $y > 0$ only due to symmetry of the flow). It is seen that Δu_x grows considerably with Ma in the vicinity of the particle, but tends rapidly to zero away from the surface. In the case of a pair of particles, reversing

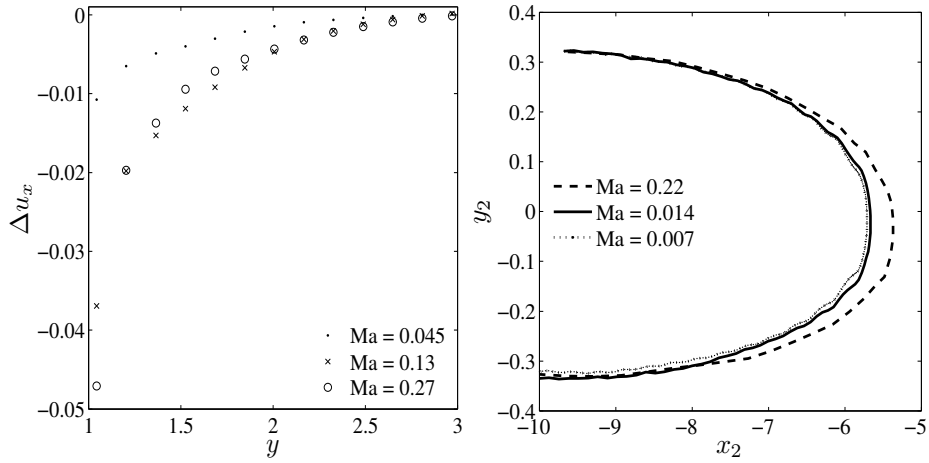

Figure 3.10: (a) The difference velocity in the flow direction $\Delta u_x(x = 0, y, z = 0)$ at $Ma = 0.0225$ and at $Ma = 0.045, 0.13$ and 0.27 plotted with y coordinate for a single particle in simple-shear flow at $Re = 0.1$. (b) The reversing pair trajectories at $Re = 0.5$ for $Ma = 0.007, 0.014$ and 0.22.

pair trajectories are considered suitable for the comparison at different Ma, for the reason that they do not involve modeled near-field lubrication forces to complicate the analysis further. Figure 3.10*b* shows the reversing trajectories for $Ma = 0.007, 0.014$ and 0.22 at $Re = 0.5$. The pair at higher Ma approaches more closely in the flow direction before reversing its path. To suppress such effects, we keep $Ma < 0.1$ in our simulations, but it is important to bear in mind that small but non-negligible effects of compressibility remain down to $Ma = O(0.01)$.

We consider now the spiraling trajectories. If the two particles begin with a very small separation in the shear plane, the expectation is that they spiral around each other before departing the close interaction. However, it is unclear that for equal or nearly equal radius spheres the in-plane spiraling motion is present at $Re = 0.1$. The spiraling trajectories in the plane of shear are, if present, compressed to an extremely small volume of trajectories which begin from pairs essentially in contact. When the Reynolds number is decreased, the reversal zone does not approach the contact surface so closely, and the expected spiraling trajectories are more readily

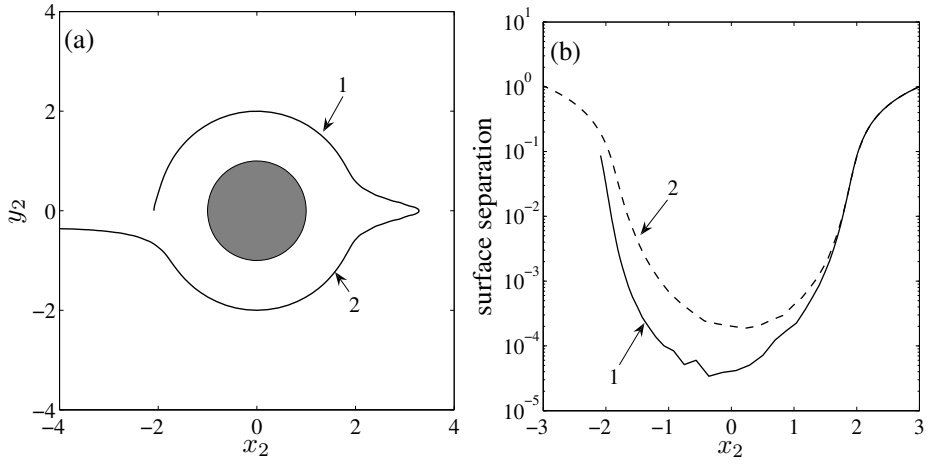

Figure 3.11: (a) The in-plane spiraling trajectory of equal radius spheres originating from $\boldsymbol{r}_0 = (-2.16, 0, 0)$ for $Re = 0.01$ in simple-shear flow. (b) Surface separation from this trajectory. The labels 1 and 2 denote segments progressing in the same sense with respect to the x direction.

observed. For $Re = 0.01$, figure 3.11a shows a spiraling trajectory originating from $\boldsymbol{r}_0 = (-2.16, 0, 0)$, a surface separation of 0.16 radii, as it makes a partial circuit and then departs to infinity. The minimum surface separation between the spheres for this case is seen in figure 3.11b to be 3×10^{-5}. For minimum surface separations of $O(10^{-4})$, the spheres are observed always to separate at this Re. We note that in Stokes flow, the minimum separation of in-plane closed trajectories is 5×10^{-5} radii [86]. It is also of interest to note that in the experimental study of Darabaner & Mason [74], in which the relative trajectories of two spheres in a circular shear flow under much weaker inertia of $Re = O(10^{-6})$ were studied, the need for this very close initial condition for "closed" trajectories was observed. In that study, if an electric field was used to bring the two spheres to apparent contact, in subsequent shearing the spheres were found to make permanent orbiting doublets of form similar to that predicted by the analysis of Batchelor & Green [5]. Without the application of electric field, the spheres did not reach the necessary minimum separation and hence separated immediately upon shearing.

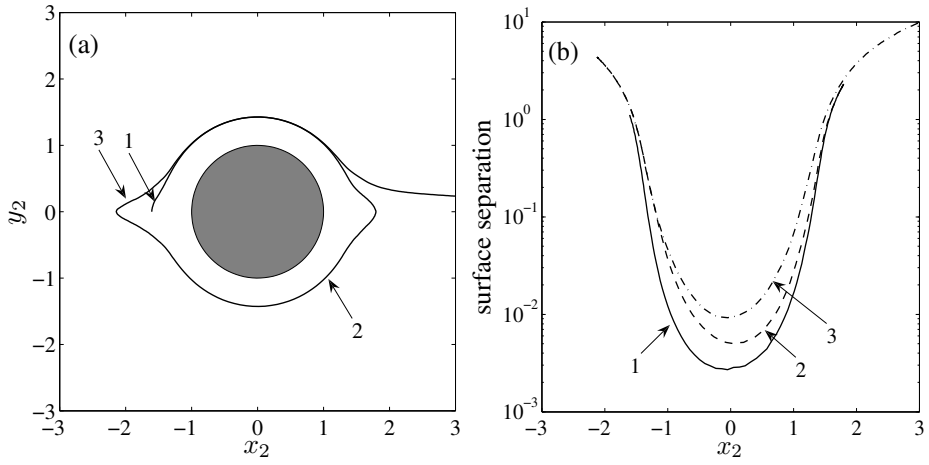

Figure 3.12: (a) The in-plane spiraling trajectory originating from $(-1.6, 0, 0)$ at $Re = 0.01$ for a pair of spheres with radius ratio of 2.3 in simple-shear flow (b) surface separation from this trajectory. The labels 1, 2, and 3 denote segments progressing in the same sense with respect to the x direction.

Figure 3.12a shows a spiraling trajectory for pair radius ratio 2.3 at $Re = 0.01$. The corresponding surface separation for various portions of the curve are labeled. These indicate the portions of the trajectory over which the relative velocity has the same sign in the x coordinate. As the pair makes a full circuit, the pair separation increases and this is seen in more detail in figure 3.12b.

3.4.2 Off-plane trajectories

We term the trajectories not residing in the shear plane "off-plane." At $Re = 0$, the xy-projection of the off-plane trajectories have a similar appearance to those in the shear plane, i.e. the presence of closed and open trajectories with a limiting closed trajectory separating the two. Over a complete circuit, these have zero displacement, $\Delta z = 0$. Any finite Re, however, breaks this symmetry and the trajectories are no longer closed. Again, there are three types of trajectories, namely reversing, open and spiraling. In the following discussion, the behavior of trajectories is described for $r_{0z} > 0$ and the arguments can be extended for $r_{0z} < 0$ from the symmetry across the

shear plane.

Reversing trajectories

For a fixed r_{0x} ($r_{0x} = -9.7$ was the usual case), various initial vorticity coordinates r_{0z} were studied. For $r_{0z} = 0$, the net vorticity displacement $\Delta z = 0$ as symmetry requires no motion in z. For small finite r_{0z}, the net vorticity displacement (Δz) of the reversing trajectories is negative while at higher r_{0z}, Δz changes sign and becomes positive. We present this observation without having sought to delineate the initial separation surface leading to $\Delta z < 0$ because of the domain dependence and dependence on the manner of releasing the particle (the initial condition).

Open trajectories

Following the arguments of in-plane trajectories, if the initial displacement in the flow direction is fixed, one expects a critical displacement $r_{0y}^c(z)$ for every z-plane which sets the reversing trajectories apart from the open ones; this initial separation point lies on the separatrix between open and reversing trajectories. We begin by looking at the vorticity displacement (Δz) of the off-plane open trajectories. All open trajectories with $r_{0z} > 0$ are found to have a net positive Δz, meaning they are displaced away from the shear plane through the pair interaction.

The xy-projection of the off-plane open trajectories is now considered. For small values of r_{0z}, the open trajectories are visually very similar to the open trajectories in the shearing plane for the same value of gradient displacement r_{0y}. As the initial separation is taken with larger r_{0z}, the pair trajectory exhibits a decreasing gradient displacement Δy, as illustrated by figure 3.13 for the off-plane open trajectories starting at $r_{0z} = 0, 0.032$ and 1.9.

(a)

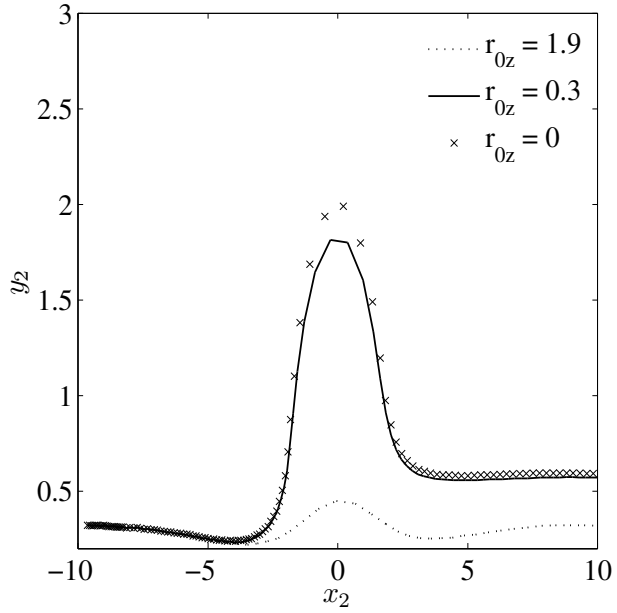

(b)

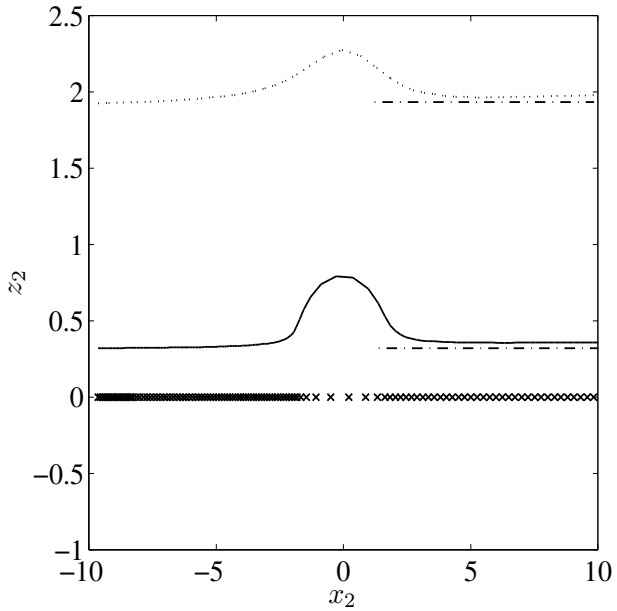

Figure 3.13: Open trajectories starting from $(-9.7, 0.3, r_{0z})$ for $r_{0z} = 0, 0.3$ and 1.9 at $Re = 0.1$ (a)xy-projection (b)xz-projection. For reference, the dashed-dotted line is at the original vorticity separation, and the deviation of the curves from this line illustrates the vorticity displacement Δz. For the trajectory with $r_{0z} = 0$, the points are equally spaced in time, and hence look denser upon approach than separation because of the positive gradient displacement.

Spiraling trajectories

The most visually prominent effect of inertia upon the pair trajectory space is the introduction of spiraling trajectories along the vorticity axis. The term spiraling refers to a trajectory which increases in distance from the z axis as the pair z separation decreases. An xy-projection of such a trajectory cuts the x axis successively, for example, at x_1 and x_2 with $|x_2| > |x_1|$, and a similar statement may be made for the crossing of the y axis in this projection. A pair originating from a point at separation in z of a few radii, and only slightly displaced from the z axis, will spiral towards the shear plane. Following their closest approach, the pair move away with the shear flow to infinite separation. Early in this trajectory, the motion has two components, along the z-axis towards the plane of shear and spiraling in the local xy plane. Suppose the initial displacement is $\boldsymbol{r}_0 = (0, r_{0y}, r_{0z})$. For a trajectory with smaller r_{0y}, the z-directed motion is more pronounced than the spiraling and thus there is a limiting trajectory that coincides with the z axis and does not spiral. This motion presumably would be unstable to any displacement outward (in x or y), which would yield a spiral motion.

Figure 3.14 shows trajectories with $\boldsymbol{r}_0 = (-0.0032, 0.016, 2.9)$. First consider figure 3.14a, b for $Re = 0.1$ in xy- and xz-projections, respectively. The two particles spiral toward one another along the vorticity axis. Following a close encounter, the particles move off toward infinite separation in opposite directions of the shear flow. Examination of the xz-projection of the trajectory shows that initially it has only negative z-velocity but as the pair becomes close, the z-directed relative motion changes sign during each circuit, while still bringing the pair closer over each full circuit. This motion is quite similar to that of a fluid element around a freely-rotating sphere seen in §3.3. Hence the streamline configuration around a single

sphere (shown in figure 3.5) should aid in understanding the pair behavior at Re larger than computed here.

We now consider the xz-projections of spiraling trajectories at $Re = 0.1, 0.2$ and 0.5, shown respectively in figure 3.14b, c and d. The strain undergone by the flow ($\dot{\gamma}t$) at points along the trajectories is labeled with $t = 0$ at the initial separation, $\boldsymbol{r}_0$. Note that the initial separation is the same for each of these conditions. For the trajectory at largest $Re = 0.5$, the advance along the z-axis is more rapid, and the particles approach one another and complete the close interaction at the smallest value of the strain. The observation of a larger strain to complete the close interaction at smaller Re is consistent with the $Re = 0$ prediction that the interaction would be a closed trajectory, and would take place at a bounded separation for infinite strain.

Before closing this section, we note that the finite Re pair trajectories are functions of initial conditions (history dependent). Our approach has been to allow the spheres to reach a steady rotation rate, i.e. the hydrodynamic torque relaxes to zero, at fixed $\boldsymbol{r}_0$ prior to allowing translation. The equilibration time scales as $\tau_{eq} = H^2/\nu$, the time required for diffusion of momentum from the walls to the center, where ν is the kinematic viscosity of the fluid. One could also set the body in motion with the velocity of the fluid which would be at its center point under the assumption this reduces the hydrodynamic force, but this is a poor condition for very close pairs such as those seen in the in-plane spiraling case. It was judged prudent to use the single initial condition of torque relaxation in all cases. This is admittedly not a completely accurate representation of the free trajectories, but we have found that the far-field open and reversing trajectories obtained with and without torque equilibration are indistinguishable.

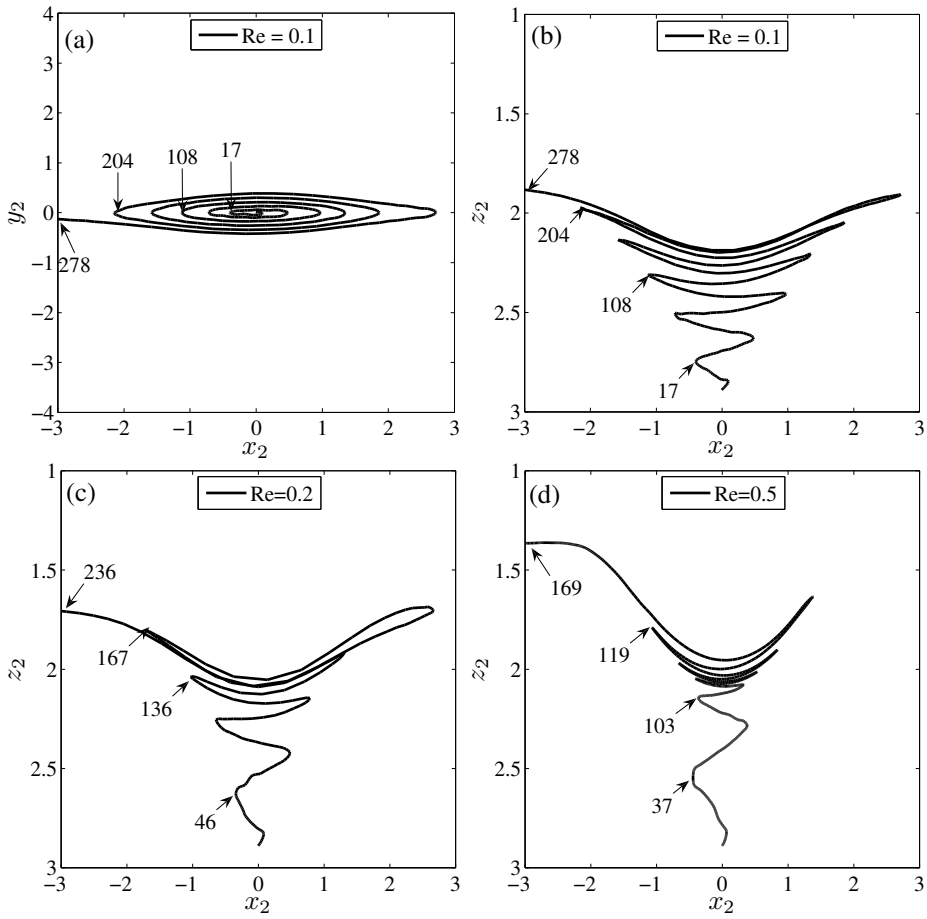

Figure 3.14: Off-plane spiraling trajectories starting from $\boldsymbol{r}_0 = (-0.0032, 0.016, 2.9)$ (a) $Re = 0.1$, xy-projection (b) $Re = 0.1$, xz-projection (c) $Re = 0.2$, xz-projection (d) $Re = 0.5$, xz-projection. The arrows indicate the strain ($\dot{\gamma}t$) values where the trajectory crosses $y = 0$ for $x < 0$ as illustrated in (a). Strain (or t) is zero at $\boldsymbol{r}_0$.

3.5 Conclusions

The hydrodynamic interactions of a pair of spherical particles suspended in simple-shear flow at finite Re is a basic issue important to development of the understanding of inertia in suspension mechanics. While it is not feasible to map the entire trajectory space numerically even for a single Re, by focusing on $Re = O(0.1)$, we have delineated the structure of the finite Re pair trajectory space for neutrally-buoyant spheres of equal size. The similarity of the various forms of trajectory seen in the pair space to the streamlines around a single freely-rotating sphere provides some guidance in considering the pair interaction at larger Re.

Using the lattice-Boltzmann method with a wall-bounded geometry with periodicity in the flow and vorticity direction, we have demonstrated the characteristics of finite inertial pair trajectories in simple-shear flow. The role of the boundary is found to be minimal for wall separations of ten particle diameters at $Re = O(0.1)$, while the periodicity in the flow direction has some quantitative effects. The periodicity in the vorticity direction has negligible effect upon the in-plane trajectories presented but may alter the quantitative results for off-plane trajectories.

For the range of Reynolds numbers $Re = O(10^{-2}) - O(1)$ studied, the simulated trajectories were qualitatively much different than those at $Re = 0$. The closed pair trajectories [5] present at $Re = 0$ vanish at finite inertia, a result which in hindsight can largely be deduced from the loss of the fore-aft symmetry of Stokes flow. The inertia gives rise to new classes of pair relative trajectories which are similar to the reversing [42] and spiraling [43, 44] streamlines around a freely-rotating sphere. The open trajectories occupy most of the pair trajectory space and are fore-aft asymmetric at finite Re, giving always a positive offset in the gradient direction for neutrally-buoyant particles. The reversing and spiraling trajectories, which replace the closed

trajectories predicted at $Re = 0$, occupy a smaller volume of pair-trajectory space. In fact, at $Re \geq 0.1$, the in-plane spiraling trajectories have not been observed in our calculations, although it is not expected that they completely vanish.

This study of particle interactions due to inertial hydrodynamics may have relevance to examination of structures seen in bulk suspension flows. In earlier work, the flow around a single sphere at finite Re, and in particular the reversing streamlines, was invoked to suggest pair trajectory reversal as a possible basis for the formation of trains of particles in pressure-driven flow in a pipe [79]. The reversing pair trajectories presented here provide a better guide to consideration of this issue. In more general terms, our study serves as a step towards developing theoretical understanding of the role of inertia at the particle scale in particle-laden flows.

Chapter 4

Inertial migration in a pressure-driven rectangular conduit flow

4.1 Introduction

Inertia-driven lateral migration of particles in a Poiseuille flow [31, 38, 33] has received greater attention in recent years due to proposed microfluidic-based applications in biology and medicine [87, 88, 89, 90, 91]. Segré & Silberberg [31] first observed that in a pressure driven pipe flow at small inertia, neutrally buoyant particles migrate to a distance $0.6R$ from the centerline, where R is the radius of the pipe. The physical mechanism of migration is based on the balance of two forces acting on the particle. These are 1. wall-induced lift force, directed away from the wall and 2. a force due to parabolic nature of the velocity profile, directed toward the wall [92]. The equilibrium position is a function of Reynolds number, Re and is found to shift towards the wall with Re for small particles [37, 38, 33, 93]. However, the analysis presented in these studies is based on point particles; as a result the finite size effects are not taken into account. It has been shown only recently that for larger particles, the Reynolds number dependence is more complex as there exists a critical

Re below which particles migrate closer to the wall and above which they migrate towards the centerline [33, 94]. This is particularly important in microfluidics where particle diameter is often a large fraction of the channel dimension.

Lateral migration in non-axisymmetric geometries is also reported in experiments [87, 95, 89, 90, 91] and numerical simulations [80, 96]. The spatial asymmetry in such geometries gives rise to multiple equilibrium positions. Simulations of Chun & Ladd [80] predict 4 to 8 particle equilibrium locations in square channels depending on Re. Edd *et al.* [89] reported two focusing positions in a 2:1 channel. óHowever, a complete understanding of parametric dependence of particle migration is still lacking.

In a dilute suspension flow, inertial interactions of particles lead to the formation of ordered chains at their equilibrium positions [79, 89]. For example, in a high aspect ratio microchannel Edd *et al.* [89] reported that 1. particles are self-organized into an array that alternated from one side of the channel to the other, and 2. each particle is separated from its nearest neighbor by a uniform spacing in the flow direction. But no explanation was suggested for this behavior.

In this chapter, first we study different parameters that affect particle migration in rectangular channels. Those include channel aspect ratio $\xi = H/W$, size ratio $\lambda = W/d$ and the Reynolds number on the particle scale Re_p. The evolution of stable particle positions in the channel is discussed in this parameter space. Secondly, we address the self-organized structures of particles in a dilute suspension flow and illustrate the underlying physical mechanism by analyzing streamlines around an isolated particle. We perform single, two and many-body simulations to generate the results reported in this paper. For numerical simulations we use the lattice Boltzmann method developed for particulate suspensions [57, 97].

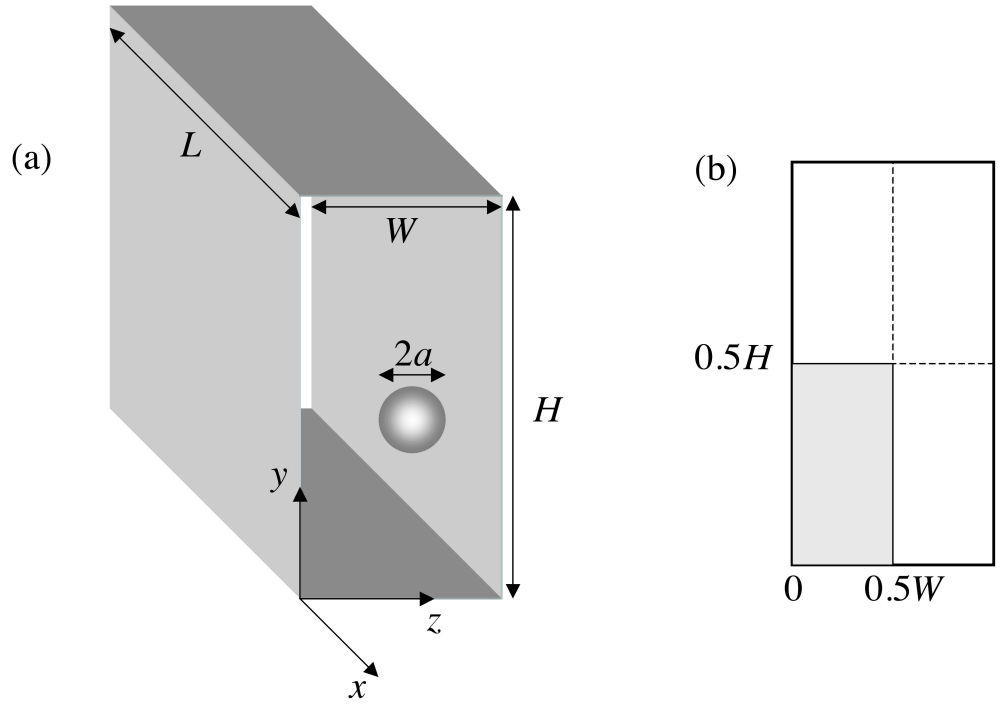

Figure 4.1: (a) Schematic for the problem of a rigid sphere in a rectangular channel studied in this work. (b) Only a quarter of the cross-section is considered as the problem has mirror symmetry in other quarters.

4.2 Problem statement and dimensionless parameters

We consider the pressure-driven flow of a Newtonian fluid of density ρ and viscosity μ in a rectangular conduit. Here, our aim is to find the equilibrium position (or positions) of a non-Brownian and neutrally buoyant particle in the rectangular cross-section. The computational domain is a box of $L \times H \times W$ as shown in figure 4.1. In the lattice-Boltzmann method, the pressure-gradient is implemented as a constant force density. Periodic boundary conditions are applied in the flow (x) direction [see figure 4.1]. The particle has a diameter $d = 10$ lattice units (LU) and the length of the box is $L = 24d$.

The dimensionless parameters governing the particle motion are

Reynolds number $Re = \rho U D_h/\mu$,

particle Reynolds number $Re_p = Re(\frac{a}{D_h})^2$,

aspect ratio, $\xi = H/W$,

size ratio, $\lambda = W/d$,

where $D_h = 2WH/(W+H)$ is hydraulic diameter of the channel and U is the average axial fluid velocity.

We shall focus on the parameters Re_p, ξ and λ. The rationale behind choosing these parameters is explained below. At $Re = 0$, reversibility of the Stokes flow prohibits cross-stream migration of the particle. However, the nonlinearity in the finite Reynolds number flow gives rise to a lateral force. For a pressure-driven flow in a plane channel, the lateral force yielding migration is zero at a distance $0.2L_c$ from the wall for $Re_p \ll 1$ and $\lambda \gg 1$ i.e. for a point particle. The migration velocity, associated with the lateral force, is obtained from the Stokes drag law ($3\pi\mu d V_m$) and is given by [36, 38]

$$\frac{V_m}{U} = Re(\frac{d}{L_c})^3\psi = Re_p\frac{d}{L_c}\psi \tag{4.1}$$

where, ψ is some scaled function and L_c is the characteristic length scale of migration (H or W here). Note that ψ is a function of particle position across the channel height and Re. The Reynolds number dependence of ψ can be disregarded when $1 < Re < 100$ which is typical range of Re in the present study. In a square geometry (i.e. $\xi = 1$), the particle has equilibrium positions at the corner and at the center of each side due to uniformity in the shear rate gradients [80, 91]. But in a rectangular conduit ($\xi > 1$), the kinematics of the flow is altered and the short dimension of the channel becomes the dominant direction of shear. It is therefore expected to give rise to a preferential motion of the particle. Next, since we simulate motion of the particle in a confined geometry, size of the particle relative to channel dimension plays

an important role, as can be seen from equation (4.1). Issues include the fact that the particle is interacting not only with the closest boundary but also with the opposite boundary and the corner. Recent experiments and simulations in a square geometry reveal distinct particle dynamics and complex scaling of the lateral force for different size ratios [96].

In the next section, the dependence of particle equilibrium locations on each parameter Re_p, ξ and λ is studied separately by varying one parameter keeping the others fixed.

4.3 Single particle migration

Only a quarter of the cross-section is considered [see figure 4.1b], since particle motion in the other quadrants follow the mirror-symmetry. We run separate simulations of the particle starting with different initial positions (z_0, y_0) in the cross-section. The equilibrium position is achieved when the particle migrates to (z_e, y_e) such that it experiences zero hydrodynamic lift and undergoes no further cross-stream motion.

Let us first understand particle motion in the rectangular geometry by looking at the trajectories. We limit our discussion to $Re_p = 1.25$, $\xi = 2$ and $\lambda = 3$ i.e. particle diameter is one-third of channel width. Figure 4.2a shows the trajectories of a single particle placed at various positions in the cross-section. The grey region is for the excluded volume. Note that the actual trajectories advance in 3-D, but to facilitate the understanding we project them on to 2-D. For example, the downstream distance traveled by the corner trajectory before reaching its final position is approximately $50L$. The figure shows that the particle eventually reaches a stable position located at $(0.27W, 0.5H)$ i.e. at the center of the longer side and approximately midway

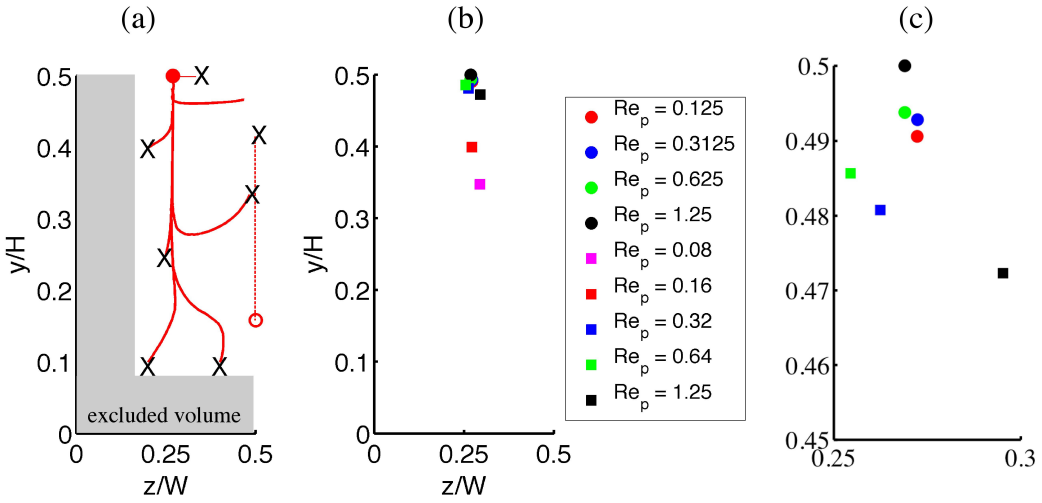

Figure 4.2: (a) Trajectories of an isolated particle with different initial positions (marked by X) eventually reaching the center of the larger edge for parameters, $\lambda = 3$, $\xi = 2$ and $Re_p = 1.25$. The stable and unstable equilibrium states are denoted by filled and open circles respectively. (b) Stable equilibrium positions of a particle in the cross-section for varying Re_p obtained experimentally (squares) and numerically (circles). (c) Expanded view of $0.25 \leq z \leq 0.3$ and $0.45 \leq y \leq 0.5$.

between wall and centerline in the short direction. Each trajectory has two common features: 1. it travels faster in the small dimension thereby reaching a steady z_e, and then 2. it travels along a line parallel to the longer edge before reaching its final position at (z_e, y_e). Note that there is also an unstable equilibrium state on the mid-plane of short side for initial positions $(0.5W, y_0)$. Any perturbation around the mid-plane is observed to lead to the stable position. It is therefore interesting to note the initial tendency of a particle to move towards the unstable point before changing its direction in some parts of the cross-section.

In figure 4.2 (b-c), it is shown that the final equilibrium position is unchanged upon varying Re_p. Thus in the full rectangular domain, there are four particle focusing positions (one in each quarter). We also compare the steady state particle positions with experimental results of Humphry [98]. The experiments used polystyrene particles of $d = 10$ μm introduced at 0.1% solid fraction in a PDMS microchannel

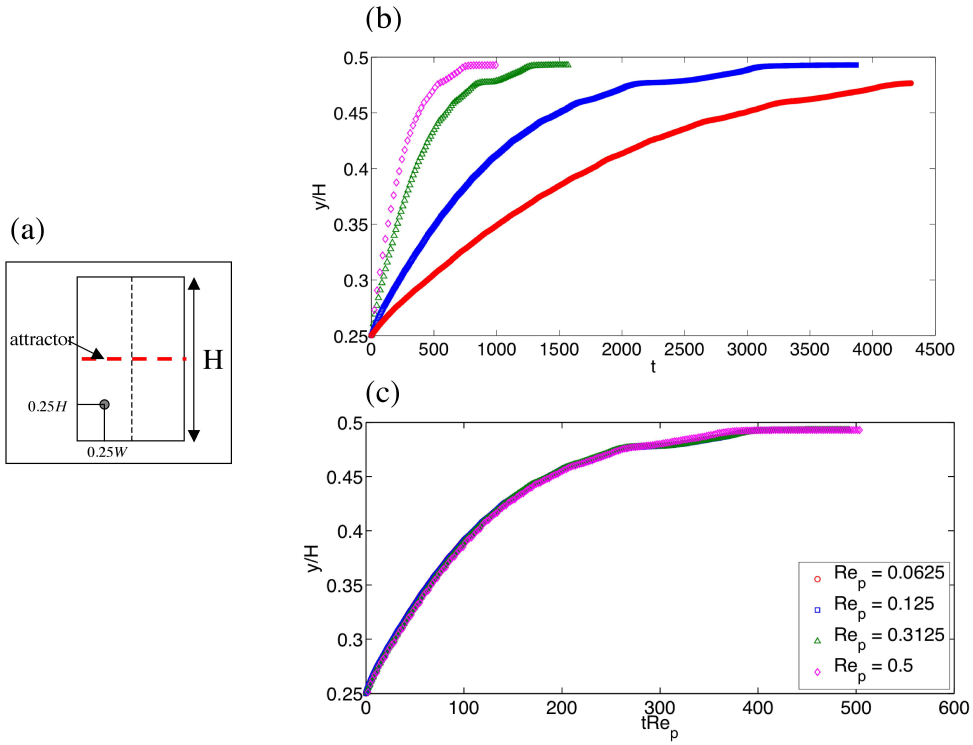

Figure 4.3: Migration velocity scales linearly with Re_p. (a) Sketch of the initial particle position in the cross-section (b) The vertical displacement of the particle toward the attractor as a function of time for varying Re_p. (c) Modified normalization of time as tRe_p so that the displacement data collapse on a single curve.

of $L = 5$ cm, $W = 25$ μm and $H = 50$ μm. The Reynolds number, Re_p, was varied by changing the flow rate and the measurements of particle positions were taken at a distance of 4.8 cm downstream. The experiments indicate that a particle migrates to the center only when $Re_p \geq 0.3$. This discrepancy is argued based on entry length, which is length of the channel required for the complete migration. The entry length is longer when the migration velocity is small. The issue is discussed further in the following paragraph.

Using the numerical simulations, we inferred that the particle migration velocity scales linearly with Re_p. To investigate this, we choose one representative initial position of the particle located at $(0.25W, 0.25H)$ in the cross-section and track

its motion with time toward the attractor (marked by thick dotted line in figure 4.3a). Here, we disregard the particle motion in the smaller dimension as it changes insignificantly with Re_p. In figure 4.3 (b), the vertical displacement, y/H, of the particle is plotted as a function of time t, non-dimensionalized using the average shear rate U/H, for varying Re_p. It is seen that the time required for the particle to migrate to the attractor goes on increasing with Re_p and it is highest for $Re_p = 0.0625$. Note that the slope of y/H vs t is related to the migration velocity at that position. The migration velocity is thus constant initially, but then goes on decreasing before it becomes zero at the steady state. When the time is instead plotted as tRe_p, the data collapse on a single curve as shown in fig 4.3c. For the plane channel flow, the linear relationship between the transverse velocity and Re_p can be obtained in the limit of point particle and low Re_p from equation (4.1), but appears to hold here for $Re_p = O(1)$.

Figure 4.4c suggests that a particle reaches its stable position when $tRe_p \approx 400$. Referring to the experiments of Humphry [98], $tRe_p = 400$ is achieved for $Re_p \approx 0.4$, as a result the particles have not reached their stable positions completely when $Re_p < 0.4$.

Next, we study the effect of channel aspect ratio on particle migration. To accomplish this, the width of the channel is fixed at $W = 3d$ and height is varied from $H = 3d$ to $6d$. Thus the aspect ratio under consideration is between $\xi = 1$ to 2. The Reynolds number and particle size ratio are kept constant at $Re_p = 1.25$ and $\lambda = 3$. To demonstrate the preferential motion of the particle, a sample initial position is chosen as $(0.25W, 0.25H)$ which is equidistant from mid-plane and wall in both dimensions. The snapshots of the final particle configuration are shown in figure 4.4a for varying ξ. Due to symmetry, the particle in square geometry ($\xi = 1$) travels on the diagonal before reaching its equilibrium position placed at $(0.29W, 0.29H)$.

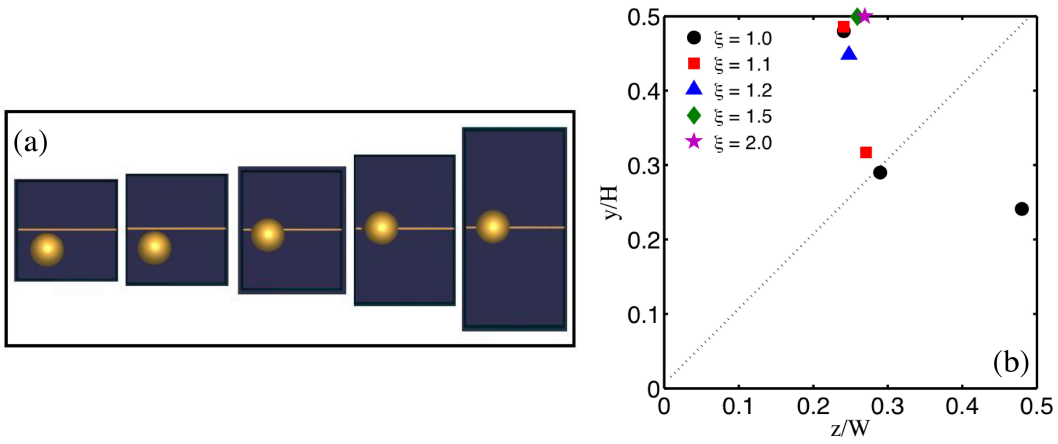

Figure 4.4: (a) Snapshots of the steady state particle configuration in a rectangular duct flow for varying aspect ratio. The mid-plane in y is shown by the solid yellow line. The starting position of particle in all cases was located at $(0.5W, 0.5H)$. (b) Stable equilibrium positions of the particle, obtained by trajectory analysis, in the cross-section for varying aspect ratio. Note that normalization for y for each ξ is different according to H.

For $\xi = 1.1$, it is shifted slightly toward the center at $(0.27W, 0.32H)$. As ξ increases from 1 to 2, the particle prefers to migrate toward the center of the long side.

In the square channel, Chun & Ladd [80] reported stable equilibrium states on the diagonal $(0.13W, 0.13H)$ and at the center of each face $(0.5W, 0.13H; 0.13W, 0.5H)$ for a size ratio of $\lambda = 9$ and Reynolds number $Re_p = 1.0$. In the present study, the stability of the position along the diagonal is analyzed by running simulations with starting position slightly displaced around the symmetry line. We find that the particle reaches to the same point reported above. Recently, DiCarlo *et al.* [96] performed finite element simulations of particle in the square channel. They reported the equilibrium positions at the center of each face but not on the symmetry line. This is not true for a particle that starts on the symmetry line as it cannot choose a side and should stay on it. It is therefore to be noted that their finding was based on the lateral force on the particle as a function of its position in the cross-section whereas our study is based on time-integrated particle trajectories with given initial

Table 4.1: Particle equilibrium locations as a function of channel aspect ratio.

W/d	H/W	Equilibrium locations	W/d	H/W	Equilibrium locations
3	1.0	corner center-long edge center-short edge	5	1.0	corner center-long edge center-short edge
3	1.1	corner center-long edge	5	1.1	center-long edge center-short edge
3	1.2	center-long edge	5	1.2	center-long edge center-short edge
3	1.5	center-long edge	5	1.5	center-long edge center-short edge
3	2.0	center-long edge	5	2.0	center-long edge center-short edge

position.

The stable equilibrium states at the the center of short side vanish as the aspect ratio increases but reappear upon increasing λ [see table 4.1]. This is in agreement with DiCarlo *et al.* [96] who also performed confocal imaging experiments with 10 μm particles in nearly square and high aspect ratio microchannels. The authors observed four focusing locations, one at the center of each side, in a 50×40 μm (i.e. $\xi = 1.2$) channel and two focusing locations, centered at the mid-point of long side, in a 50×20 μm (i.e. $\xi = 2.5$) channel.

Finally, we show that the aspect ratio is not the only parameter responsible for the existence of the attractor at centerline. The size of the particle relative to the channel dimension is equally important. As will be shown below, for small particles we find multiple steady states in the channel. In numerical simulations, the particle size is

kept constant, whereas W and H are varied. In figure 4.4, equilibrium positions are shown for 3 size ratios $\lambda = 3, 5$ and 10. As discussed earlier for $\lambda = 3$, the centerline is the only stable position. It is slightly displaced from centerline at $(0.24W, 0.45H)$ for $\lambda = 5$, but there is an additional point on the center of the shorter side. For $\lambda = 10$, the final position of the particle is found to be a strong function of its initial position; as a result we report many equilibrium positions, notably along $z = 0.17W$ and between $y = 0.1 - 0.5H$. This is consistent with experimental finding of Bhagat *et al.* [91] who utilized 50×20 μm channels and particles of size 2 μm ($\lambda = 10$). The authors demonstrated a focusing line of particles at a distance of $0.15W$ from the larger edge with the help of high-speed fluorescent imaging.

To aid the understanding of multiple coexisting attractors, we borrow concepts from theory of dynamical systems and chaos. The particle motion in the channel is described by a set of differential equations. The state of the system is described by the current position of the particle, (z, y), and the initial position, (z_0, y_0), in the cross-section. Given an initial point, the time evolution of the system, called as 'trajectory', is determined by parameters λ, ξ and Re_p. The attractor is then the state of the system in the limit $t \to \infty$ and a basin of attraction is a set of initial conditions that lead to a particular attractor. The idea of basin of attraction is illustrated in figure 4.5b-c, where we show vector maps of initial particle displacements for $\lambda = 3$ and 10. The arrows indicate the magnitude and the direction of particle migration. The vector maps for the two differ significantly near the attractors for $\lambda = 10$. In the present system, there is a bifurcation point as we change the parameter $\lambda = 3$ to $\lambda = 10$. The qualitative behavior of the system changes.

From figure 4.5c, it is seen that for the case of $\lambda = 10$, the initial particle displacements are perpendicular to the longer edge in most parts of cross-section except near the corner. As the aspect ratio increases, the axial velocity is practically

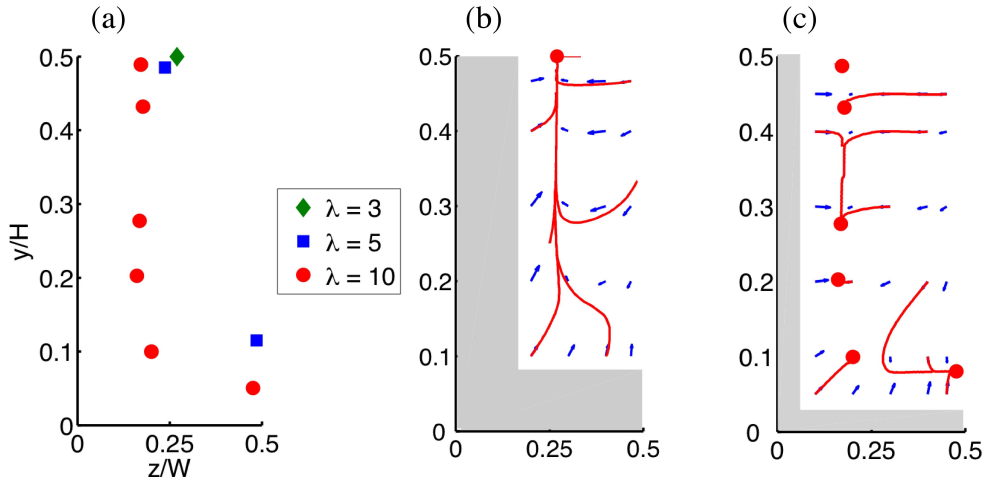

Figure 4.5: (a) Equilibrium positions of a particle in the cross-section for $\lambda = W/d = 3, 5,$ and 10. (b-c) Vector map of initial displacement of a particle in the cross-section for $\lambda = 3$ (b) and $\lambda = 10$ (c). The arrows indicate the direction and magnitude of the migration velocity. The solid lines represent the trajectories.

uniform along the height and the short dimension becomes the dominant direction of shear. This is in accordance with the limit of plane channel flow (or $\xi \to \infty$) in which particles migrate only in the direction of shear.

Before proceeding to the next section, we present a brief summary of the results on single particle migration. In the Stokes flow limit, no attractors are present in the geometry, since a particle on an initial streamline stays on it forever. Therefore finite inertia is a necessary ingredient for the existence of the attractors in the system. In a two-dimensional channel flow the attractors are located at the Segré-Silberberg equilibrium positions and in the pipe flow the attractor is a circle of radius $0.6R$. The symmetry of the circle breaks in the case of a square channel and particle equilibration takes place at eight points in the cross-section. Upon increasing the aspect ratio, the migration occurs much faster in the short dimension and multiple attractors exist at roughly Segré-Silberberg distance from the mid-plane in short dimension. When the size of particle is increased, only two focusing points are obtained. This is illustrated

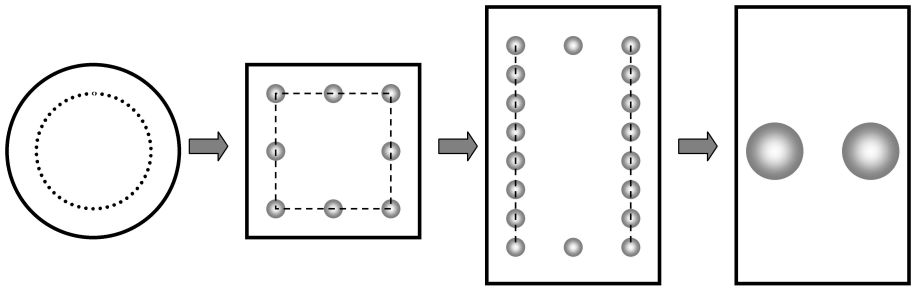

Figure 4.6: Summary of single particle migration in the range $Re \leq 100$. The dotted circle represent Segré-Silberberg attractor at a distance $0.6R$ from the center. The circles denote the final equilibrium locations while the dashed line represent weak attractors at low Re.

in figure 4.6.

The inertial migration of rigid particles in rectangular conduits have numerous applications in size-based filtration and bioseparations [88, 89, 91, 99]. Our extensive examination of particle equilibration will provide essential protocols in design of such systems.

4.4 Self-ordering

In this section, we investigate the self-ordered structures of particles in pressure-driven flow in rectangular conduits. Our interest in the problem is inspired by recent experimental observations [89, 98]: particles at their equilibrium positions arrange themselves in uniformly spaced zig-zag chains that are aligned in the flow direction. We attempt to reproduce the structure by running multi-particle simulations in a box of $24d \times 6d \times 3d$ with $d = 10$ lattice units (LU). The conditions are chosen so as to match the experiments and hence the discussion is limited to $Re_p = 1.25$. A random distribution of 9 particles ($\phi \approx 1\%$) is chosen as the initial configuration [see figure 4.7]. The left and the right section in figure 4.7 represent the side and top view of the channel respectively. As discussed in the previous section, the overall rectangular domain has two attractors located at the center of the larger edge. Therefore as the

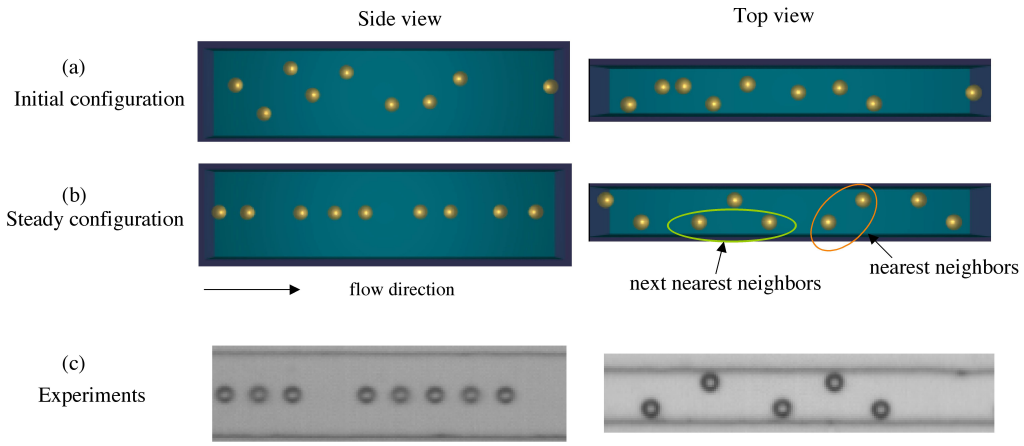

Figure 4.7: A randomly distributed initial configuration (a) of 9 particles in a 2 : 1 rectangular conduit when subjected to the pressure-driven flow, evolves into an ordered structure (b). At steady state, the particles are located at equilibrium positions and exhibit uniform separation in the flow direction. (c) Experimental images of Humphry, 2009 [98] in a 50×25 μm channel with 10 μm diameter particles. The left and the right section represent the side view and the top view of the channel.

system evolves in time, the particles first undergo lateral migration to occupy their nearest equilibrium positions. The particles then interact with each other such that they exhibit uniform axial spacing with the nearest neighbor and the next nearest neighbor located on the other and same side of mid-plane, respectively. This is illustrated in the top view of the steady state configuration. Once formed, the chains persist in time with all particles moving forward at the same speed. The simulated structure of particles in the conduit is found to match quite well with the experiments.

The uniformly spaced chains of particles at Segré-Silberberg equilibrium positions have also been observed in the pipe flow [79] above pipe Reynolds number $Re \geq 100$. It was suggested that the chaining was associated with the hydrodynamic interactions of particles in finite-inertia shear flow. The axial separation between the particles decreased upon increasing Re_p, a finding that indicated the role of disturbance shear flow seen by the particle. The experiments utilized relatively small particles such that

the ratio $D/d \geq 17$, where D is the pipe diameter. In the present study, however, particles are relatively large and span a large fraction of the small channel dimension.

In order to get further insight into the structure, we compute the steady disturbance flow around an isolated particle with the help of lattice-Botlzmann method. A particle size of $d = 24$ LU is chosen to achieve a higher mesh density and size of the computational box is $10d \times 6d \times 3d$. In figure 4.8, we plot the streamlines around a single particle in the xz plane passing through $y = 0.5H$. Note that the streamlines shown are of the velocity relative to the particle motion. The topology of the flow in the vicinity of the particle is similar to the one seen in the case of a simple shear flow at $Re_p = O(1)$ [42, 43, 97]. It is characterized by the open, and reversing streamline regions in addition to the near-field spiraling region. Herein, due to confinement the particle also disturbs the flow in the other half of the channel, thereby generating the flow reversal zones accompanied by two stagnation points, A, B and a saddle point, C. The fluid particles in the surrounding region shall tend to accumulate near the stagnation points. In the case of a simple shear flow, it has been found that the nature of the pair trajectories is qualitatively similar to the fluid streamlines around the particle in both Stokes [5] and finite Reynolds number flows [97]. It is therefore expected that at steady state the neighboring particle would migrate to one of the stagnation point in the flow set by the first particle. The suggested positions of adjacent particles centered at points A and B are shown by open circles in figure 4.8. It is to be noted that the adjacent particle will again disturb the flow and favor the position of third particle at location D. The axial spacing between nearest and next nearest neighbors is thus obtained as $2.5d$ and $5d$.

To support our argument, we simulate the motion of a pair of particles separated by different distances in the flow direction but located roughly at their equilibrium points [see figure 4.8b]. In figure 4.8c, we plot the axial spacing between the two

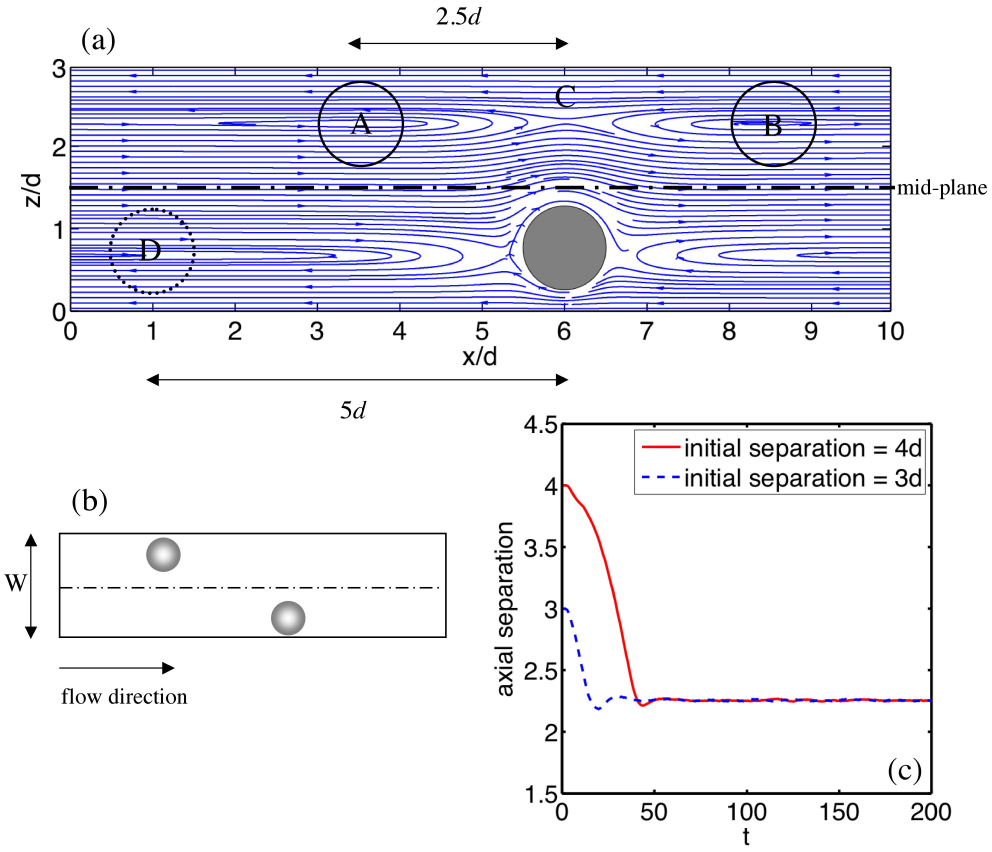

Figure 4.8: Suggested mechanism for particle arrangement. (a) Streamlines around an isolated particle in the xz plane. The open and dotted circles represent the favored positions of adjacent particles. (b) Simulation geometry for the pair problem: two particles with arbitrary initial separation in flow direction and located roughly at their equilibrium positions. (c) Axial separation between the pair as a function of time.

Table 4.2: Axial spacing between particles that are aligned in the flow direction in pressure-driven rectangular conduits.

finding	particle spacing
experiments [89, 98]	$2.4d$
streamlines, present study	$2.5d$
pair simulations, present study	$2.25d$

particles as a function of time t for two different initial separations. It is seen that the pair eventually reaches a steady longitudinal spacing of $2.25d$. A comparison of particle spacing, obtained by different methods, is shown in table 4.2.

We do not aim to study the dependence of axial separation on various geometric and flow parameters. It is clear, nonetheless, that particle size ratio is crucial to disturb the flow significantly across the mid-plane. Another parameter that naturally comes into play is particle concentration ϕ. However, a more relevant parameter is the number density per unit length, χ. Based on our finding, we determine the critical number density, $\chi_c = 0.57$ per particle diameter, below which the steady state particle spacing remains unchanged. But beyond χ_c, the near-field particle interactions disturb the structure and clusters of closely-spaced particles are formed [98]. A case of $\chi = 0.75$ is illustrated in figure 4.9 and compared with experimental results of Humphry [98].

4.5 Conclusions

We have examined inertia-driven transverse migration of neutrally-bouyant particles in the rectangular conduits via lattice-Boltzmann simulations. The evolution of the particle position in the cross-section is found to have a complex dependence on aspect ratio (H/W) and channel to particle size ratio (W/d). First, by focusing on a

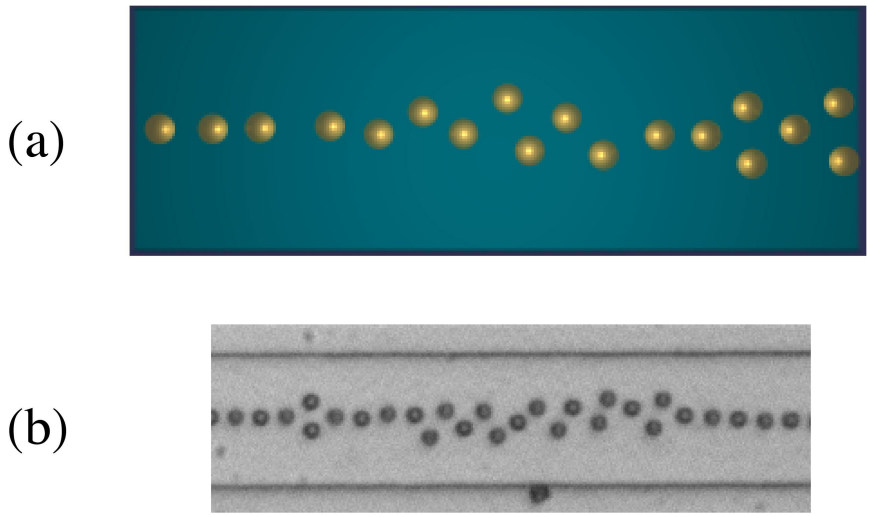

Figure 4.9: Side view of the steady particle configuration obtained for $\chi = 0.75$ in a $3:1$ conduit and $W/d = 3$. (a) Simulation (b) Experiments [98].

$2:1$ channel and particle of size one third of channel width, we have delineated the nature of particle trajectories with different starting positions. The particle always migrates to the center of larger edge and the rate of approach is found to scale linearly with particle Reynolds number. In a square geometry, due to uniformity of shear rate gradients the particle has steady state positions at the center of each face and on the diagonals. Upon increasing the aspect ratio, however, the shear rates become inhomogeneous and the particle has preferential direction of migration. The size of particle plays an important role and is found to give to rise to multiple coexisting attractors of different strengths.

We have also addressed the structure of particle arrangement when a dilute suspension is subjected to the pressure-driven flow in a $2:1$ rectangular conduits. While the multi-particle simulations confirmed the presence of self-ordering of particles, the analysis of streamlines around an isolated particle and the pair motion provided the mechanical basis for it. We believe that our study will serve as guide in interpreting the results of recent experiments [89, 98].

Chapter 5

Microstructure and rheology of a sheared suspension at finite inertia

5.1 Introduction

The rheological properties of suspensions are important in design of operations in many fields of industry, e.g. suspension coating and slurry transport. Much progress has been made towards understanding viscous suspensions at low particle Reynolds numbers. Under dilute conditions hydrodynamic interactions between the particles can be neglected and the suspension exhibits Newtonian rheology, with a relative viscosity $\mu_r = \frac{\mu_s}{\mu} = 1 + 2.5\phi$, where μ_s is the effective viscosity of the suspension and μ is the viscosity of the suspending fluid [4]. Deviations from Newtonian behavior are observed at higher ϕ. Experimental findings show the presence of normal stresses exhibited by viscous suspensions at low Reynolds numbers [20, 21, 22], as well as shear thickening [100]. These experiments were primarily carried out for concentrated suspensions ($\phi \geq 0.3$) where the normal stresses become large enough for reliable measurement. The isotropic particle stress, termed the particle pressure (Π), was disregarded in earlier studies [4, 101], but has been reported in recent study [21].

This chapter is published as *Suspension properties at finite Reynolds number from simulated shear flow*, P. M. Kulkarni and J. F. Morris, Phys. Fluids **20**, pp. 040602 (2008)

Computer simulations have significantly improved our understanding of viscous suspensions. Brady and co-workers [11, 12] have developed the Stokesian Dynamics, a method for simulating suspensions at low Reynolds number which can accurately capture many-body hydrodynamic interactions. An important issue which simulation has probed is that of particle microstructure in flow, an issue experimentally considered by Parsi & Gadala-Maria [19]. Simulation studies have explored the structural asymmetry [14] and related this to the shear-induced normal stresses [15, 16, 18]. Simulations of Sierou & Brady [18] by Stokesian Dynamics showed that both first (N_1) and second (N_2) normal stress differences are negative for $0.1 \leq \phi \leq 0.5$, with $N_1 \approx N_2$ and increasing in magnitude with the concentration. They found generally good qualitative agreement for N_1, N_2 and Π with experimental results of Zarraga *et al.* [21] and Singh *et al.* [22], with Π inferred rather than directly measured experimentally, although the experiments show $|N_2|/|N_1|$ to be larger than found in simulation. Issues related to the normal stresses in concentrated suspensions include particle migration in curvilinear [28] and pressure-driven flows [102, 25].

Our understanding of Stokes-flow suspensions is much more advanced than that of suspensions with finite inertia at the particle scale, implying nonzero $Re = \rho\dot{\gamma}a^2/\mu$, where a is the radius of a spherical particle, $\dot{\gamma}$ is the shear rate and ρ is the fluid density. In the dilute limit, simple shear flow with finite inertia over a sphere was analyzed using matched asymptotic expansions for $Re \ll 1$; weak inertia was found to cause an increase in the particle contribution to the viscosity of $O(Re^{3/2})$ and by breaking the symmetry of Stokes flow to give rise to $O(Re)$ normal stresses [45]. Full solution of the Navier-Stokes equations for finite-Reynolds-number flow in suspensions of mobile particles is challenging. Conventional computational fluid dynamical techniques such as the finite element method allow the refinement of grids near the particle surfaces and have largely examined 2-dimensional particulate flows when inertia is considered

[78, 50]. In FEM, the requirement of remeshing the fluid as particles move leads to increased computational costs and greater complexity of the algorithm. We choose to work with the lattice-Boltzmann method (LBM) as developed for particle-laden flows [54, 64, 56, 57]. In the LBM, the particle and fluid motion are computed on a fixed grid, and finite inertia does not present added difficulty. The spatial locality of the lattice-Boltzmann equation and the fixed grid provide ease of parallelization. Several LB-based studies of suspensions have been reported. These include studies of two-dimensional systems [60, 103], in which pair motions have been examined, as well as studies which have shown an increase in the effective viscosity of dense suspensions with Re [61, 62, 63]. Shakib-Manesh *et al.* [61] developed a method that allows computation of the solid- and fluid-phase contributions to the total shear stress. From 2D LB simulations they found that the shear-thickening is related to the enhanced contribution from the solid phase to the total shear stress as Re increases. Following a similar approach Raiskinmäki *et al.* [62] studied the clustering of particles in a sheared suspension over the range $0 < Re \leq 10$. The authors argued that increased particle clustering with Re leads to the rise in viscosity of the suspension. Considering the detailed motions of isolated bodies, the present authors have shown that fluid inertia alters the topology of the pair trajectories in simple shear flow [97]. The closed trajectories [5] predicted at $Re = 0$ vanish to be replaced by spiraling and reversing trajectories.

As will be discussed in § 5.3, inertia introduces novel mechanisms for momentum transport, namely Reynolds stress due to fluctuational motion and stress due to particle acceleration. Using the LBM, we evaluate all of these to determine the total relative viscosity, normal stress differences and suspension pressure for $\phi = 0.05 - 0.3$ and $Re = O(1)$. The results are presented in § 5.4, preceded by the problem formulation and a description of the method for extracting the bulk stress

from the simulations.

5.2 Problem formulation

5.2.1 Governing equations and computational domain

Our interest is in the motion of neutrally-buoyant solid spherical particles of radius a suspended in a Newtonian fluid of density ρ and viscosity μ. The governing equations in non-dimensional form for the fluid phase are

$$\boldsymbol{\nabla} \cdot \boldsymbol{u} = 0 \tag{5.1}$$

$$Re(\frac{\partial \boldsymbol{u}}{\partial t} + \boldsymbol{u} \cdot \boldsymbol{\nabla} \boldsymbol{u}) = -\boldsymbol{\nabla} p + \nabla^2 \boldsymbol{u} \tag{5.2}$$

where length has been made dimensionless with the radius of the sphere a, time by the inverse of the shear rate $\dot{\gamma}^{-1}$, fluid velocity by $\dot{\gamma} a$, and the pressure by $\mu\dot{\gamma}$. Particle translations ($\boldsymbol{U}_i$) and rotations ($\boldsymbol{\Omega}_i$) are governed by Newtonian dynamics,

$$m_i \frac{\partial \boldsymbol{U}_i}{\partial t} = \boldsymbol{F}_i \tag{5.3}$$

$$I_i \frac{\partial \boldsymbol{\Omega}_i}{\partial t} = \boldsymbol{T}_i, \tag{5.4}$$

where the net force $\boldsymbol{F}_i$ and net torque $\boldsymbol{T}_i$ act on the particle i, which has mass and moment of inertia m_i and I_i, respectively. The parameters governing the problem are the shear flow Reynolds number, defined as $Re = \rho\dot{\gamma}a^2/\mu$ and solid-volume fraction ϕ. The suspension is subjected to wall-bounded simple-shear flow. In the numerical simulations, we consider a computation box of size $L \times H \times W$ in the flow (x), gradient (y) and vorticity (z) directions, respectively, with the standard condition being $L = H = W = 20a$. The x-directed shear flow is set by moving top and bottom

walls with normal in y in opposite directions at equal speed. Periodic boundary conditions are applied in the x and z directions. We keep the domain size fixed and change the number of particles, N, to vary ϕ.

5.3 Average suspension properties

To determine the full set of viscometric functions associated with the simulated shear flow, we apply the procedure developed by Batchelor [4] to compute the bulk stress generated by a flowing suspension in terms of volume averages. In this formulation, the suspension is considered as statistically homogeneous, implying the average properties of a suspension in volume V, containing many particles, do not vary appreciably. The presence of boundaries in the system studied implies some spatial variation and we address the limitations associated with this below.

The volume and surface of a typical particle are denoted by V_p and A_p, respectively. At a material point $\boldsymbol{x}$, we denote by $\boldsymbol{u}$ and $\boldsymbol{\sigma}$ the velocity and stress fields, respectively. Without any restriction on solid-volume fraction and Reynolds number of the motion, the bulk stress (non-dimensionalized by $\mu\dot{\gamma}$) can be written as

$$\boldsymbol{\Sigma} = \frac{1}{V}\int_{V_f} -p\boldsymbol{I}\, dV + (\boldsymbol{\nabla U} + \boldsymbol{\nabla U}^T) + \boldsymbol{\Sigma}^p, \tag{5.5}$$

where V_f is the volume occupied by the fluid, and $\boldsymbol{\nabla U}$ is the volume average of the local velocity gradient. $\boldsymbol{\Sigma}^p$ denotes the particle contribution to the bulk stress and is given by

$$\boldsymbol{\Sigma}^p = \frac{1}{V}\sum_i \boldsymbol{S}_i - \frac{Re}{V}\sum_i \int_{V_p} \frac{1}{2}(\boldsymbol{ax} + \boldsymbol{xa})\, dV_i - \frac{Re}{V}\int_V \boldsymbol{u'u'}\, dV, \tag{5.6}$$

where summations are over all the particles in volume V. The first term represents the stresslet, or symmetric first moment of surface stress, exerted by a particle i, given for a rigid particle by

$$\boldsymbol{S}_i = \int_{A_p} \frac{1}{2}(\boldsymbol{x}\boldsymbol{\sigma}\cdot\boldsymbol{n} + \boldsymbol{\sigma}\cdot\boldsymbol{n}\boldsymbol{x})\, dA_i, \tag{5.7}$$

where $\boldsymbol{n}$ is the normal directed outward from the particle surface into the fluid phase. The second and third terms in the expression of particle stress denote the stress due to acceleration of the particles and the Reynolds stress, respectively. The acceleration stress originates from the non-linear convective terms $\boldsymbol{u}\cdot\boldsymbol{\nabla}\boldsymbol{u}$ in the Navier-Stokes equations. Note, acceleration of the material point $\boldsymbol{x}$ residing in particle i is $\boldsymbol{a} = \boldsymbol{a}_i + \boldsymbol{\alpha}_i\times\boldsymbol{x} + \boldsymbol{\Omega}_i\times(\boldsymbol{\Omega}_i\times\boldsymbol{x})$, where $\boldsymbol{a}_i$ and $\boldsymbol{\alpha}_i$ are linear and angular accelerations of the particle. The presence of particles disturbs the mean bulk motion of the fluid ($\overline{\boldsymbol{u}}$) and the resulting velocity fluctuations ($\boldsymbol{u'} = \boldsymbol{u}-\overline{\boldsymbol{u}}$) at the microscale cause momentum transfer across a surface element. These velocity fluctuations are concealed by the averaging process, but are taken into account through the Reynolds stress [4]. The expression (5.6) shows directly that the contributions to the bulk stress from the acceleration and Reynolds stress are dependent on Re; the stresslet is dependent on Re through the flow solution. For a dilute suspension, the interactions between the particles can be neglected and the solution for a single particle can be used to calculate the particle stress. Using matched asymptotic expansions, Lin *et al.* [45] obtained the flow field around a single particle at small but finite Re and deduced that inertia gives rise to normal stresses with a negative first normal stress difference and positive second normal stress difference. Finite element calculations [42] confirm the validity of the theory at $O(Re)$.

It is an objective of this study to calculate the particle stress ($\boldsymbol{\Sigma}^p$) for a suspension

in simple-shear flow over a range of ϕ and Re. At each time step, the acceleration and Reynolds stresses are computed from the knowledge of particle velocities and the velocity field. The stresslets are computed from (2.14). The time-averaged quantities of interest are relative viscosity μ_r, the normal stress differences N_1 and N_2, and the particle pressure Π, defined as

$$\mu_r = 1 + \frac{< \Sigma^p_{xy} >}{\mu\dot{\gamma}}, \tag{5.8}$$

$$N_1 =< \Sigma^p_{xx} > - < \Sigma^p_{yy} >, \tag{5.9}$$

$$N_2 =< \Sigma^p_{yy} > - < \Sigma^p_{zz} >, \tag{5.10}$$

$$\text{and} \quad \Pi = -\frac{1}{3}(< \Sigma^p_{xx} > + < \Sigma^p_{yy} > + < \Sigma^p_{zz} >), \tag{5.11}$$

where <> denotes the time averaged quantity.

5.4 Simulational results

5.4.1 Bulk stress

Here, we provide the numerically-determined bulk rheological properties of suspensions at varying ϕ and Re. Simulations start with the particles placed randomly in the simulation domain. The walls are set in motion with the mixture in a resting state. We simulate flows which generate total strains of $\dot{\gamma}t = 100$ – 300 depending on Reynolds number. Data from the first 20-30 strain are discarded so that the initial condition and bulk acceleration do not affect the reported properties. We present the time-averaged properties for $0.01 \leq Re \leq 2$ and for $0.05 \leq \phi \leq 0.3$, with these solid fractions corresponding to $N = 77 - 516$ particles in the unit cell. Rheological quantities are calculated using (5.6) and (5.8-11). Before addressing the

(a)

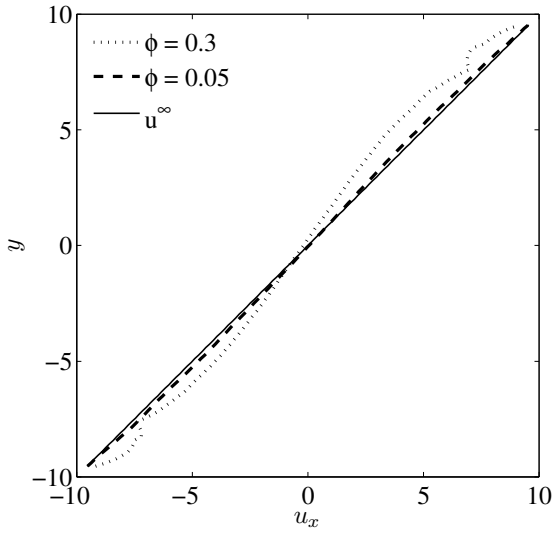

(b)

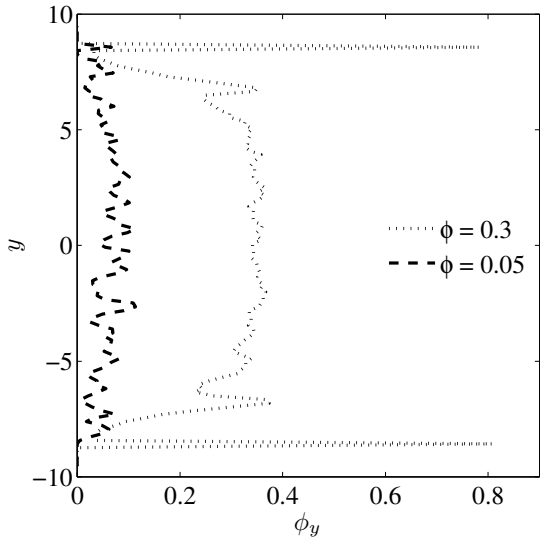

Figure 5.1: The time-averaged (a) axial velocity and (b) local solid-volume fraction ϕ_y along the height in a sheared suspension at $Re = 0.1$ and for $\phi = 0.05$ and 0.3. Note, ϕ_y is based on the center positions of the particles.

bulk rheology, we present the solid-volume fraction (ϕ_y) and the axial velocity (u_x), averaged over time and planes parallel to the walls as a function of y, the cross-stream coordinate. The results are shown in figure 5.1 for a suspension at $Re = 0.1$, with the plots arranged with y running vertically to suggest a horizontal channel. Note that the volume fraction is based on the center positions of the particles, resulting in zero ϕ near the walls. At lower ϕ a weak migration toward the center is seen, but the velocity profile is little changed from that of a linear shear flow. At $\phi = 0.3$, strong layering of particles near the walls is observed. The shear rate is no longer homogeneous near the walls and a relatively lower shear rate exists in the middle of the channel. There is thus a slip velocity on a macroscopic scale. This profile is found to develop at $\dot{\gamma}t \approx 20$ and is used for $\overline{\boldsymbol{u}}$ in the calculation of Reynolds stress (5.6).

In figure 5.2*a*, we plot the relative viscosity of the suspension as a function of ϕ for various Re. Also shown in the figure are the Eiler fit [21, 104]

$$\mu_r(\phi) = [1 + \frac{1.5\phi}{(1 - \frac{\phi}{\phi_m})}]^2 \tag{5.12}$$

with $\phi_m = 0.58$ and the dilute-limit analytical result of Batchelor & Green [105] ($\mu_r = 1 + 2.5\phi + 7.6\phi^2$), both of which are applicable at low Reynolds number. The viscosities compare well with these curves for $\phi \leq 0.2$. However μ_r departs from these predictions at higher ϕ. We have computed the viscosity directly from the shear force on the walls, as $\mu_r = F_{\mathrm{x,wall}}/(2\mu u_w/H)$ where u_w is the wall speed and H is the wall separation, in addition to the method outlined in §5.3. Viscosities at $Re = 0.1$, obtained from the two approaches for $\phi = 0.05$ and 0.3 are shown in figure 5.3 for an extended period of dimensionless time. For $\phi = 0.05$ we obtain a good agreement between the two results whereas for $\phi = 0.3$ deviations as large as 10% are observed, with the result based on the wall shear stress larger owing to the reduced shear rate

acting on the interior particles. The equivalent boundary calculation for normal stress differences is less direct and is not performed here. The effect of Re on the relative viscosity is shown in figure 5.2*b*, where we present μ_r as a function of Re for different ϕ. The general trend observed is that the viscosity of the suspension increases, *i.e.* it shear-thickens with Re, for $Re > 0.1$. The thickening for the range of Re considered here is not prominent at lower volume fractions, in agreement with results of 2D LB simulations of Kromkamp *et al.* [60] and Shakib-Manesh *et al.*[61]. It is also of interest to note that for $\phi = 0.3$, there is a small drop in the viscosity for low Re. The contributions from the acceleration and Reynolds stresses to the viscosity are found negligible compared to the stresslets, although both of them rise linearly with Re. We suggest that it is the combined effect of some ordering of the microstructure along the flow direction (as will be seen in §5.4.2) and increased single particle stresslet [42] at higher Reynolds numbers which leads to the drop and rise of the viscosity.

The first and second normal stress differences scaled by $\mu\dot{\gamma}$ are presented in figure 5.4 along with $Re = 0$ values predicted by Accelerated Stokesian Dynamics (ASD) simulation [18]. In the ASD simulations, a short range interparticle force was used to prevent overlaps of particles and it was found that both N_1 and N_2 are negative for all ϕ and $N_1 \approx N_2$. To our knowledge, no experimental data on normal stresses is available for $\phi < 0.3$, but it is worth noting that the experimental results for viscous conditions of Zarraga *et al.*[21] agree with the simulations in finding both N_1 and N_2 negative, but $|N_2|/|N_1| \approx 3.6$ from the correlation of experimental data at large ϕ. For finite Re, theoretical predictions [45] are available only in the limit of $\phi \to 0$, with $N_1 < 0$ and $N_2 > 0$, and both of $O(Re)$. For the range of ϕ considered in this study, N_1 is negative and $|N_1|$ increases with ϕ. At $Re = 0.01$, N_1 compares well with ASD simulation results for $\phi \geq 0.2$. At smaller ϕ, however, N_1 is relatively greater than the ASD values, possibly because at finite Re the single particle contributes a

(a)

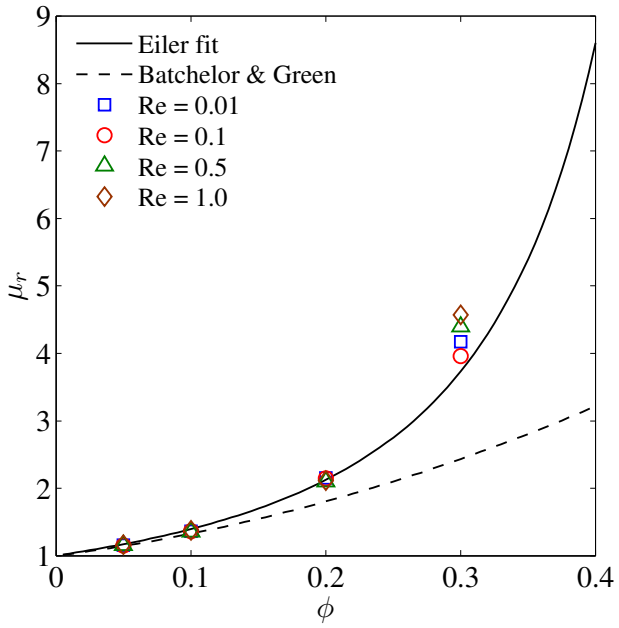

(b)

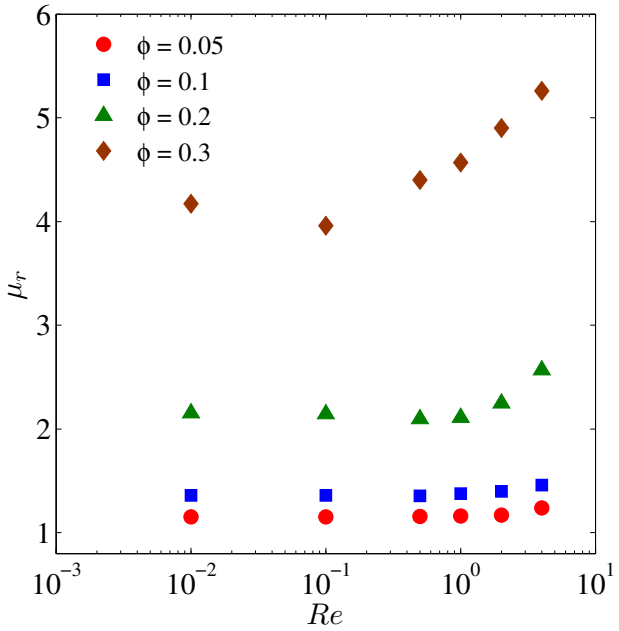

Figure 5.2: (a) The relative viscosity of a monodisperse suspension as a function of solid-volume fraction. The $Re = 0$ empirical model of Eiler [21] and analytical result of Batchelor & Green [6] are also shown. (b) The dependence of relative viscosity on Re for $0.05 \leq \phi \leq 0.3$.

(a)

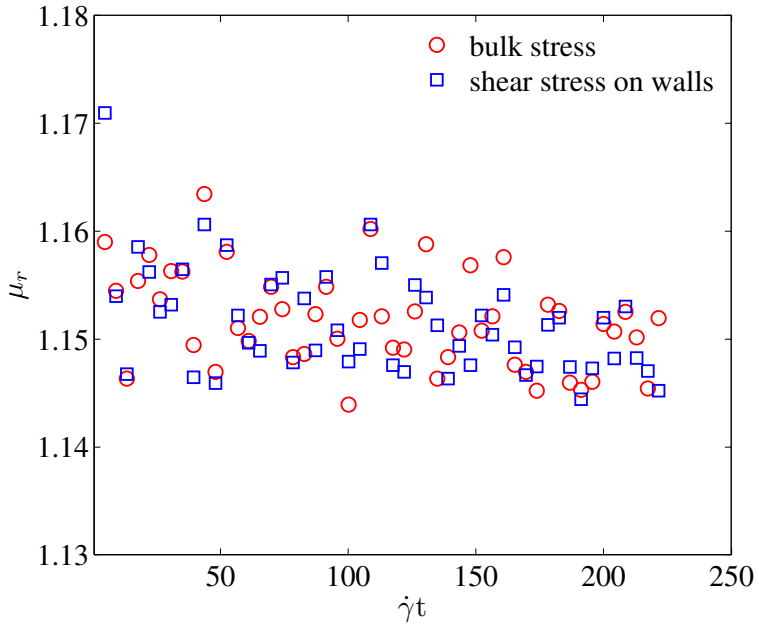

(b)

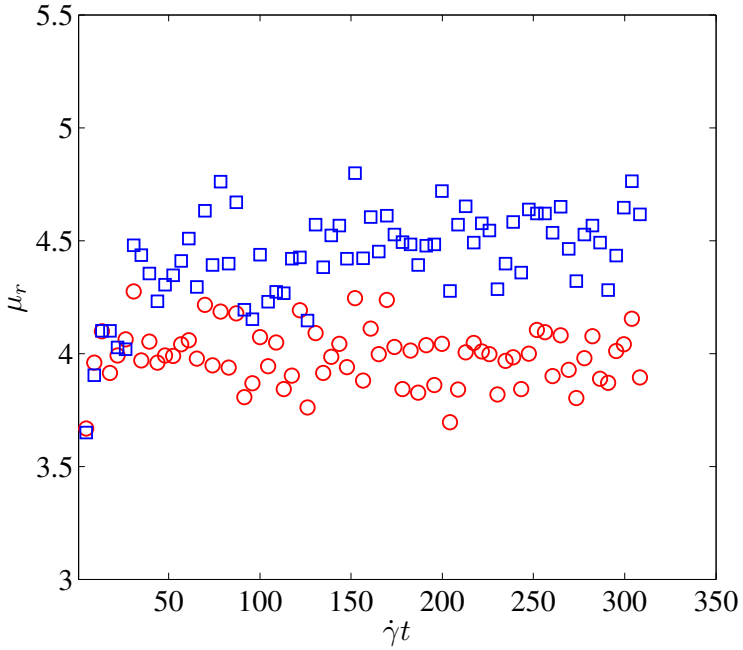

Figure 5.3: (a) The instantaneous relative viscosity of a sheared suspension at $Re = 0.1$ obtained from the bulk stress calculation and from the shear stress on the walls for (a) $\phi = 0.05$ and (b) $\phi = 0.3$, The legend applies to both plots.

finite normal stress difference. In the case of N_2, we observe a change in the sign. For $\phi \leq 0.1$, N_2 is positive for the entire range of Re, consistent with the theoretical predictions of Lin *et al.* [45] However, for a suspension with $\phi = 0.2$, N_2 is negative for $Re \leq 0.1$ and positive for $Re \geq 0.5$. For $\phi = 0.3$, N_2 is negative for all Re.

The Re dependence of N_1 and N_2 is shown in figure 5.5; the inset shows N_2 for $\phi = 0.05$ and 0.1. At low ϕ, both normal stress differences scale linearly with Re, in agreement with theoretical predictions [45] and numerical evaluation for a single sphere [42].

The particle pressure (Π), presented in figure 5.6, increases rapidly with ϕ. The agreement between LB simulations for $Re = 0.01$ and ASD results at $Re = 0$ is good at higher volume fractions. Similar to N_1 and N_2, the particle pressure is also found to be roughly $O(Re)$ for small ϕ for the range of Re studied (see figure 5.6*b*).

Before closing this section, we note that the numerical simulations suffer from certain limitations. First, in the LB method the particle surface is represented by lattice nodes, and hence one needs to choose a sufficiently large lattice density. Second, the motion is simulated in a periodic and wall-bounded domain; the bulk properties depend to some degree on L, W and H for a chosen mesh density of the sphere. The dependence on the number of particles N is equivalent to the dependence on the domain size. Effects of periodicity and domain size are not negligible at smaller volume fractions and that may explain discrepancy between LB results at $Re = 0.01$ and ASD results. Finally, finite compressibility is inherent in the LB method, but as long as $Ma < 0.1$, it does not generate qualitative differences and the quantitative effects are believed to be small.

(a)

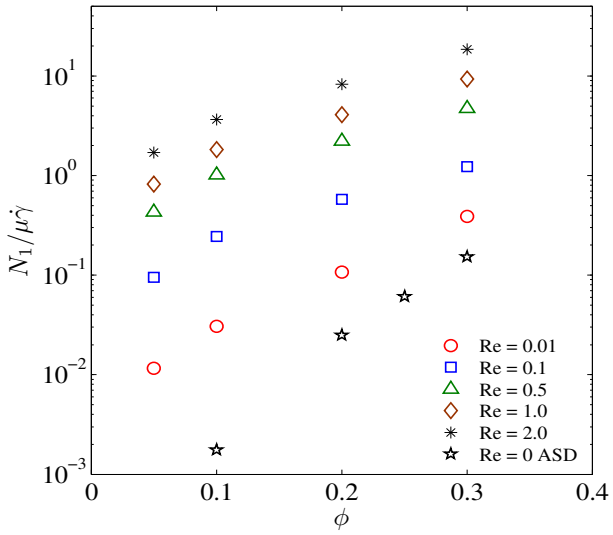

(b)

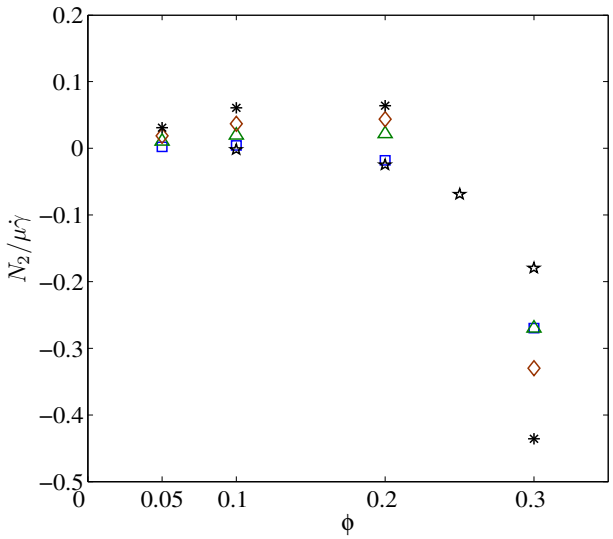

Figure 5.4: The dependence of normal stress differences on solid-volume fraction. (a) N_1, (b) N_2. Also shown are ASD simulation results for $Re = 0$. The legend applies to both plots.

(a)

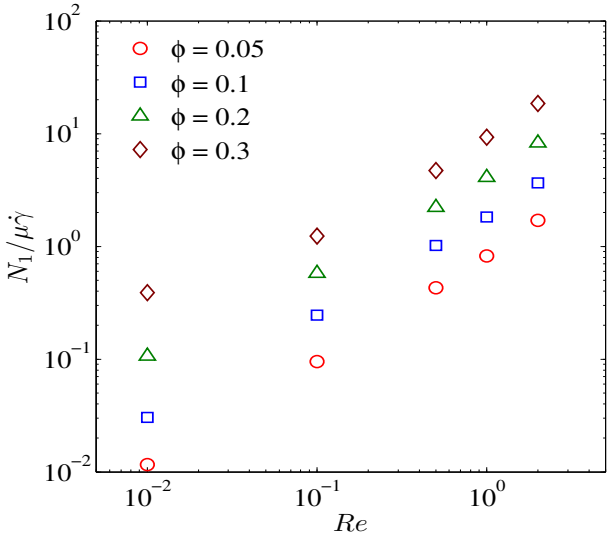

(b)

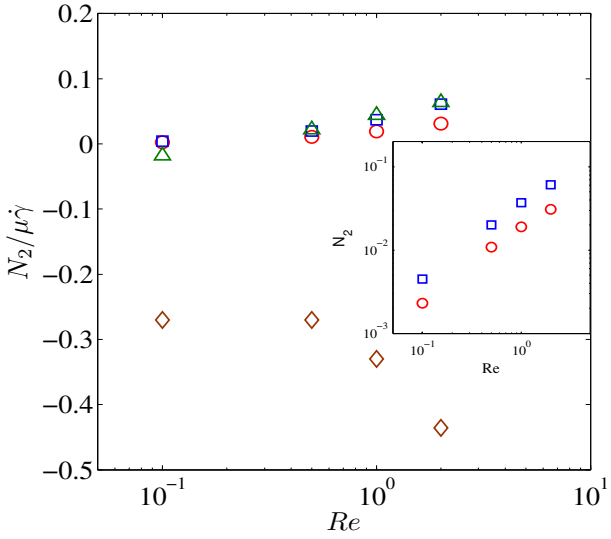

Figure 5.5: The dependence of normal stress differences on Re for $0.05 \leq \phi \leq 0.3$. (a) N_1, (b) N_2. The legend applies to both plots.

(a)

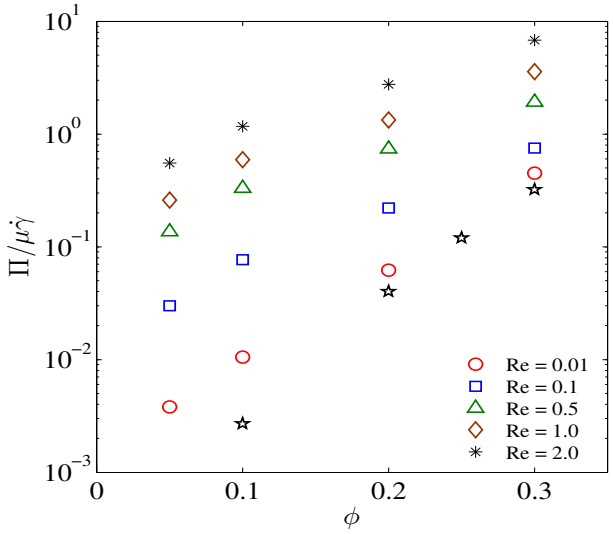

(b)

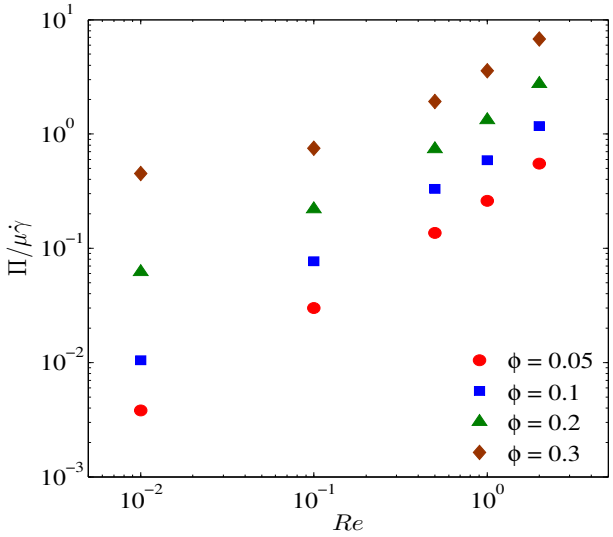

Figure 5.6: The particle pressure as a function of (a) solid-volume fraction, (b) Re. Also shown in figure a are ASD simulation results for $Re = 0$.

5.4.2 Microstructure

We consider the pair microstructure at finite Re in the simulated shear flows from which the foregoing stress results are obtained. The microstructure is described by the pair distribution function, defined as

$$g(\boldsymbol{r}) = \frac{P_{1|1}(\boldsymbol{r}|\boldsymbol{0})}{n}, \tag{5.13}$$

where n is the average particle number density and $P_{1|1}(\boldsymbol{r}|\boldsymbol{0})$ is the conditional probability of finding a particle at $\boldsymbol{r}$, given one at the origin $\boldsymbol{0}$. From the simulations, $g(\boldsymbol{r})$ is calculated as follows [16]. The pair space is discretized in (r, θ, ψ) with these coordinates sketched about a reference particle in figure 5.7, where θ is the polar angle, measured from the positive x axis and ψ is the azimuthal angle, measured from the positive z axis. At each sampling time, from the simulated particle configurations we obtain $N(N-1)/2$ pair separation vectors $\boldsymbol{r}$, where N is the number of particles. Each vector $\boldsymbol{r}$ is put into respective bin of volume $\Delta V = r^2 \Delta r \sin\psi \Delta\psi \Delta\theta$ and a running histogram $H(r, \theta, \phi)$ is built. The pair distribution function g is then calculated as

$$g(r, \theta, \psi) = \frac{H(r, \theta, \psi)}{n t_s \Delta V}, \tag{5.14}$$

where t_s is the total number of sampling points.

The particular goal here is to identify effects of fluid inertia on the microstructure in shear. We first consider the radial distribution function $g(r)$, which is $g(r, \theta, \psi)$ averaged over all possible orientations. Results are presented for $0.01 \leq Re \leq 2$ and $0.05 \leq \phi \leq 0.3$. At higher ϕ particles build up near contact because of volume exclusion and hence it is difficult to see the signature of inertia in $g(r)$. The inertial effects are expected to become more readily visible at smaller ϕ. In figure 5.8, we plot

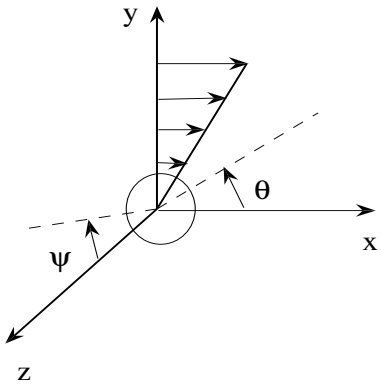

Figure 5.7: Definitions of the polar angle θ and the azimuthal angle ψ in simple shear flow $\boldsymbol{u} = (\dot{\gamma}y, 0, 0)$.

$g(r)$ for $\phi = 0.05$ at different Re along with the theoretical prediction for dilute ϕ and Stokes flow of Batchelor & Green [105], which predicts $g(r)$ is divergent at contact. The figure shows that except near contact the theoretical $g(r)$ remains smaller than the simulated values at finite Re, and $g(r)$ near contact increases with Re.

Next, we consider the angular variation of $g(\boldsymbol{r})$ adjacent to contact in the plane of shear ($\psi = \pi/2$). We recall that at $Re = 0$, $g(\boldsymbol{r})$ is fore-aft symmetric in the dilute pure hydrodynamic limit owing to the reversibility of Stokes equations. The symmetry can be broken by Brownian motion, interparticle forces or finite Re. In this study we are not considering the effect of the former two. The size of bin for r used here is relatively large at $\Delta r = 0.1$ to rapidly populate all bins at smaller volume fractions. Figure 5.9 shows angular variation of $g(2 \leq r \leq 2.1, \theta)$, termed $g(2)$, at $Re = 0.1$ for $0.05 \leq \phi \leq 0.3$. Note that $\theta > 90^o$ and $\theta < 90^o$ correspond to the compressional and extensional quadrants, respectively. The anisotropy in the pair microstructure is visible at all ϕ with elevated pair density in the compressional quadrant. However, $g(2)$ is almost constant in the range $\theta = 50^o - 130^o$, or 40^o to each side of the natural point of symmetry, 90^o. As ϕ increases, pair probability accumulates along the flow axis, *i.e.* near $\theta = 0^o$ and $\theta = 180^o$. At $\phi = 0.3$, the

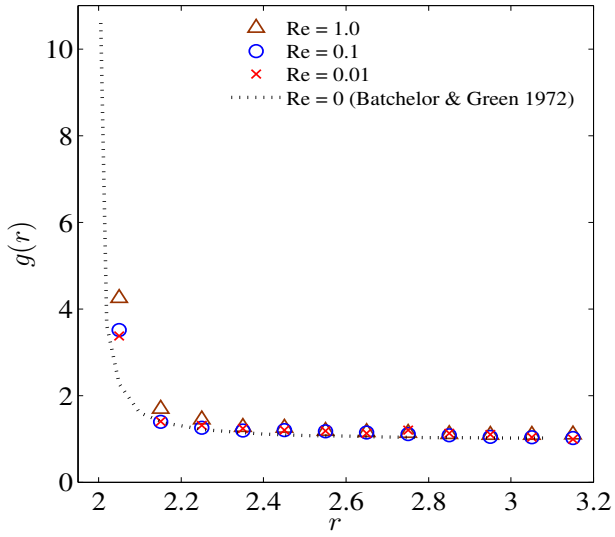

Figure 5.8: The pair distribution function $g(r)$ determined from LB simulations for a sheared suspension of $\phi = 0.05$ for $Re = 0.01, 0.1$ and 1.0.

primary peak is observed along the flow axis.

The Re dependence of $g(\boldsymbol{r})$ near contact is shown in figure 5.10, where we plot $g(2)$ in the plane of shear at $\phi = 0.1$ for $0.05 \leq Re \leq 2$. Also shown in the figure are the $Re = 0$ result obtained using Stokesian Dynamics simulations by Drazer *et al.* [106] for which the values are averaged over all ψ and for comparison, the LB result at $Re = 0.05$ likewise averaged over ψ; the data for the two cases is generally similar, and in fact differs very little over the angular range $50^o < \theta < 150^o$, with the finite-Re results somewhat elevated relative to the Stokes-flow results at the angles closer to the flow axis. Near symmetry of pair microstructure is seen at $Re = 0$ and as Re increases, the asymmetry in $g(2)$ increases substantially. In fact for $Re = 2$, the sampled pair probability at contact is zero for $5^o \leq \theta \leq 40^o$: no pairs were found in the near-contact region ($2 \leq r \leq 2.1$) for this range of angles. The maximum value of $g(2)$ observed over the contact surface also rises with Re.

The case of a suspension at $\phi = 0.3$ is considered in figure 5.11. Again, asymmetry

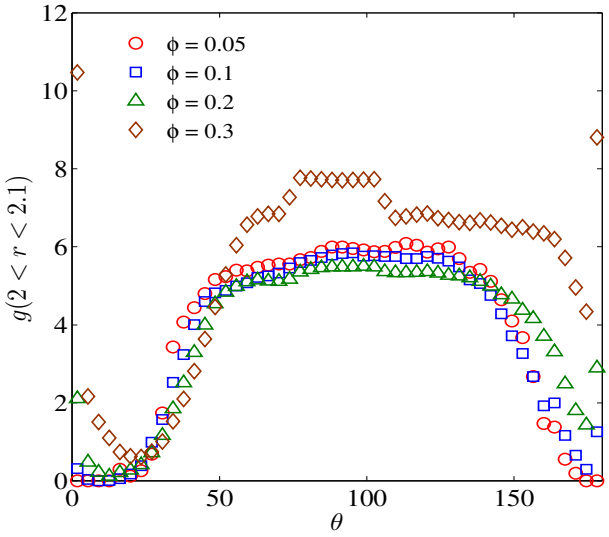

Figure 5.9: The angular dependence of pair distribution function at contact in the plane of shear for a suspension at $Re = 0.1$ for $0.05 \leq \phi \leq 0.3$ determined from LB simulations.

in $g(2)$ is observed to increase with Re, but the maximum value in the broad high-correlation region of the compressional quadrant does not vary in magnitude with Re. The notable variation in magnitude is that $g(2)$ along the flow axis increases quite rapidly with Re. This is not due to layering of particles near the wall, as layering is observed for all Re. Based on finite Re pair motion as mentioned in chapter 3, reversing trajectories may play a role in this structure, but we recall that at $\phi = 0.3$, the average surface separation between particles is well below a particle radius.

Finally, we note points where the pair microstructure may provide insight to the bulk rheology. The relationship is not so readily determined in a finite-Re suspension as in the case of $Re = 0$, as the stress associated with even an isolated pair interaction requires a time-consuming sampling of the pair space at the Re of interest, and this information is not yet available. However, certain known features of the single particle and interacting pair at finite Re may guide understanding. At low volume fractions ($\phi = 0.05$ and 0.1), a particle spends a significant fraction of the time well-separated from others and the theoretical predictions [45] for an isolated particle at finite Re

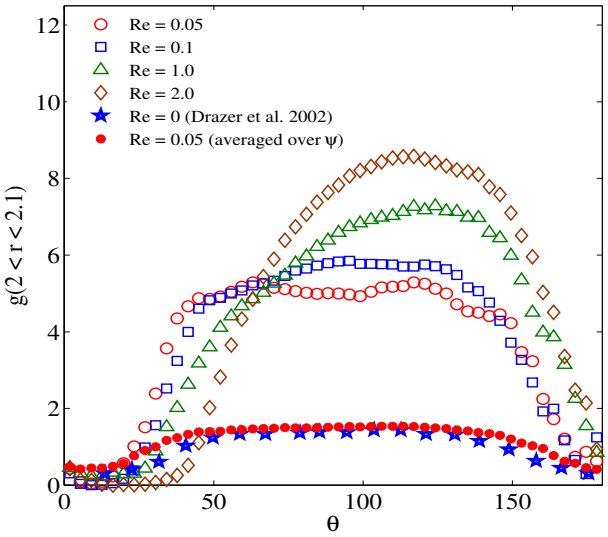

Figure 5.10: The angular dependence of pair distribution function at contact in the plane of shear for a suspension of $\phi = 0.1$ for $0.1 \leq Re \leq 2.0$.

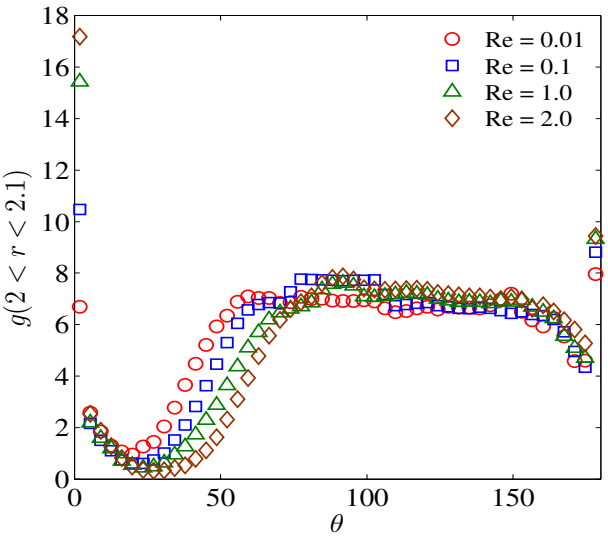

Figure 5.11: The angular dependence of pair distribution function at contact in the plane of shear for a suspension of $\phi = 0.3$ for $0.1 \leq Re \leq 2.0$.

appear to hold, namely we obtain negative N_1 and positive N_2 with both quantities scaling linearly with Re. At $\phi = 0.3$, however, the dominant contribution to the bulk stress comes from the particles near contact. Even at low Re there is a depletion of the pair probability on the downstream side of the pair interaction. If we now recall N_1 and N_2 as a function of pair orientation [21] within the plane of shear, described by θ, it appears that the structural asymmetry leads to negative N_1 and N_2.

5.4.3 Velocity fluctuations

In this section, we present probability density functions (PDF) of particle velocities in the gradient (U_y) and vorticity (U_z) directions. A single particle freely suspended in a simple-shear flow will move with the streamline at its center. The presence of a second particle forces a departure from the streamline, and U_y and U_z become nonzero. The statistics of these velocity fluctuations are probed here. The velocity PDFs fit a general form

$$P(U_i) \propto \exp[-\beta |U_i|^\alpha], \tag{5.15}$$

where $i = y$ or z, and β is a fitting parameter. The value of $\alpha = 1$ corresponding to an exponential distribution is found to describe low-ϕ data reasonably well, while $\alpha = 2$ corresponding to a Gaussian distribution is found at our largest ϕ. We do not attempt a complete fitting of the data at all conditions, as values of α intermediate between 1 and 2, as well as a mixture of the two distributions may be seen in different cases. Instead we present the data from a number of conditions and note the fitting to selected limiting cases. Figure 5.12 shows the measured PDF for U_y and U_z for $\phi = 0.05$, 0.1, 0.2, and 0.3 at $Re = 0.1$. Note that particles near the walls (surface separation from the wall less than a particle diameter) are not taken into account, and

the velocities are scaled as $\dot{\gamma}a$ using the bulk average shear rate. The width of $P(U_y)$ increases with ϕ and we see a gradual transition from an exponential to a Gaussian distribution as ϕ increases. The PDFs at $Re = 0$ obtained using Stokesian Dynamics simulations [106] exhibit a similar transition with ϕ: Drazer *et al.* argued that the addition of essentially random lubrication interactions at higher volume fraction is dominant in determining the dynamics of suspended particles at high ϕ and leads to a Gaussian PDF. At low ϕ, the particles may interact in a correlated fashion over extended periods with neighboring particles through long-range hydrodynamic fields and this results in a quite different exponential distribution.

We plot in figure 5.13 the PDFs for $\phi = 0.05$ at $Re = 0.01$ and 1. The data at $Re = 0.01$ fits the expression (20) with $\alpha = 1$ and $\beta = 11$. It also shows a good agreement with Drazer *et al.* [106] who obtained $\alpha = 1$ and $\beta = 11.4$ at $Re = 0$ and $\phi = 0.05$. We limit presentation of data to $Re = 0.01$ and 1.0 for clarity. At the higher Re, the distribution becomes narrower. Of added interest is the bell-shaped distribution at $Re = 1.0$ which has a sharp peak near $U_y = 0$. In the case of U_z, the PDF also becomes narrower with Re but no sharp peak is found at $Re = 1.0$. We consider the distributions at $\phi = 0.3$ in figure 5.14. The distribution is of Gaussian nature for U_y and decreases in width at higher Re. For U_z however, a Gaussian distribution fits the data for small velocity fluctuations, and an exponential distribution describes the data well for large fluctuations.

5.5 Conclusions

In this work, we have studied the behavior of a sheared neutrally-buoyant suspension at conditions yielding finite inertia at the particle scale. The numerical simulations were performed using the lattice-Boltzmann method in a wall-bounded

(a)

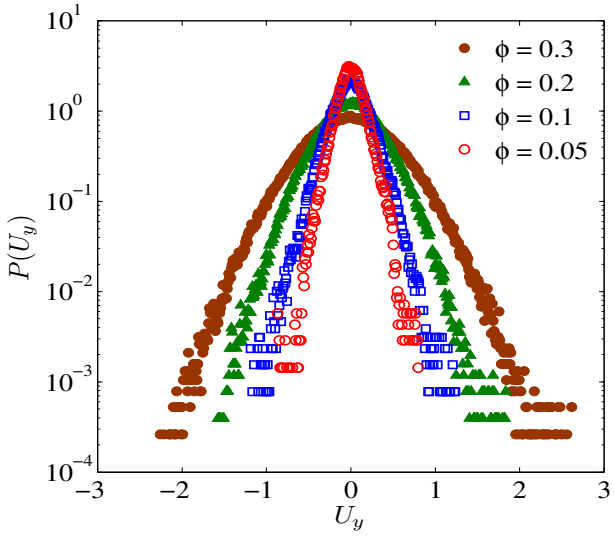

(b)

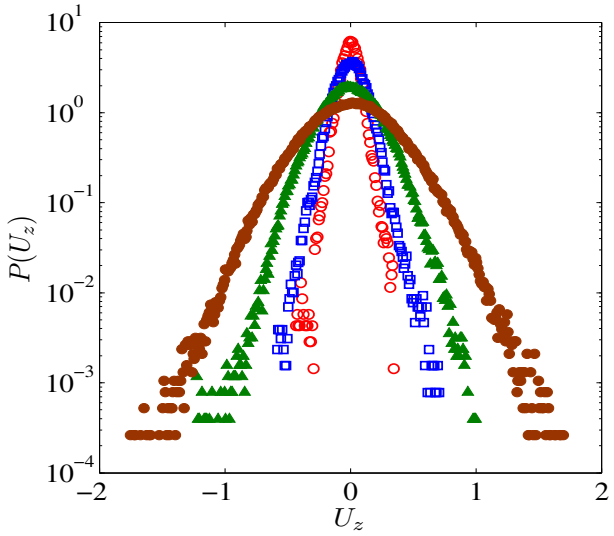

Figure 5.12: The probability density function of velocity fluctuations in the (a) gradient (y) and (b) vorticity (z) directions obtained by the LB simulations for a sheared suspension at $Re = 0.1$ for various volume fractions.

(a)

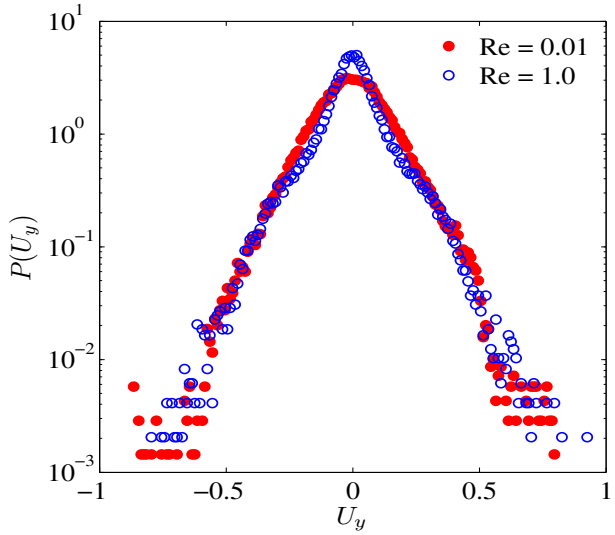

(b)

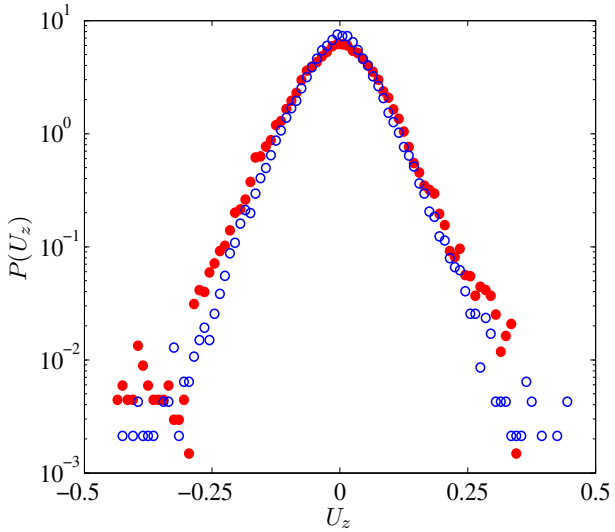

Figure 5.13: The probability density function of velocity fluctuations in the (a) gradient and (b) vorticity directions obtained by the LB simulations for a sheared suspension at $Re = 0.01$ and 1.0 and $\phi = 0.05$.

(a)

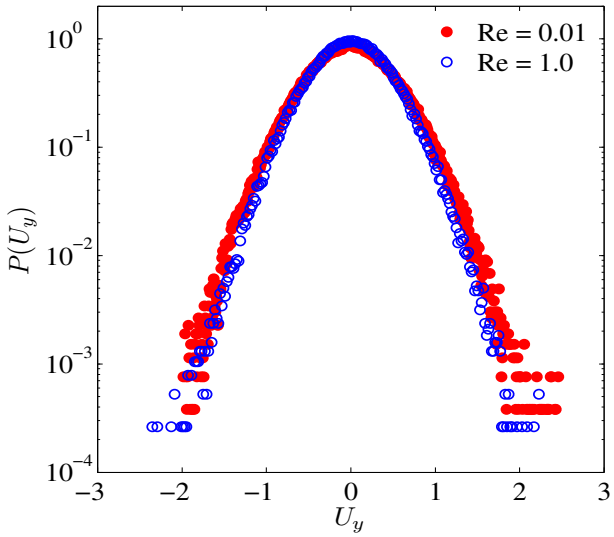

(b)

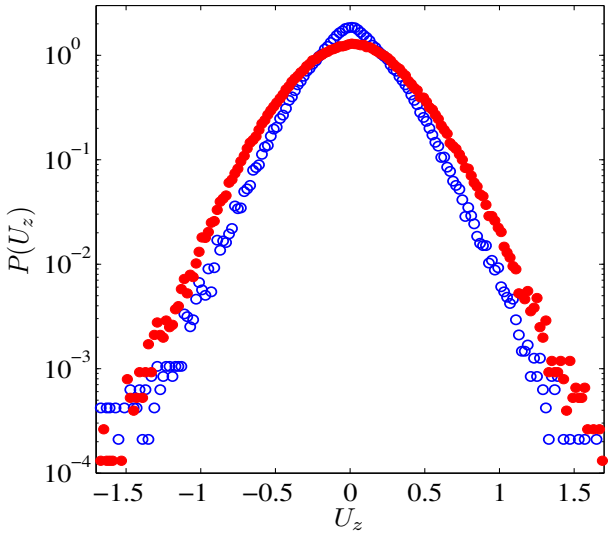

Figure 5.14: The probability density function of velocity fluctuations in the (a) gradient and (b) vorticity directions obtained by the LB simulations for a sheared suspension at $Re = 0.01$ and 1.0 and $\phi = 0.3$.

geometry with periodicity in the flow and vorticity directions. The study was restricted to dilute to moderately concentrated suspensions with $0.05 \leq \phi \leq 0.3$ and inertia at a particle-scale Reynolds number of $Re = \rho\dot{\gamma}a^2/\mu$ varying in the range $0.01 \leq Re \leq 5$. We have extracted from the simulations a number of quantities of interest from a suspension mechanical perspective, including bulk rheology, pair microstructure and velocity fluctuations.

Using Batchelor's formulation of the bulk stress, the results in this study show that inertia increases the particle contribution to the effective viscosity of the suspension and gives rise to a particle-phase normal stress. The signs of first (negative) and second (positive) normal stress difference for $\phi \leq 0.1$ are consistent with the dilute-limit low-Reynolds number theory [45] and numerics [42], and both increase in magnitude linearly with Re. A change in sign of N_2 is observed, as it becomes negative for $\phi = 0.3$. The particle pressure is positive for all ϕ and also scales linearly with Re.

Inertia breaks the fore-aft symmetry of the pair distribution function seen at dilute ϕ and $Re = 0$. The result is an anisotropic pair microstructure with elevated near-contact pair correlation in the compressional quadrant of the shear flow; the degree of asymmetry grows with Re. The microstructure found from the simulation undergoes a change at $\phi = 0.3$, as the primary peak is observed along the flow axis rather than in the compressional quadrant as seen at dilute ϕ. Such changes appear to qualitatively affect the non-Newtonian rheology of the suspension, as N_2 undergoes the noted sign change as ϕ increases.

Finally, the probability density functions of transverse velocities were reported. In general, the probability densities undergo a transition from exponential at low ϕ to a Gaussian distribution at relatively higher ϕ. For U_z, however, the Gaussian fit for low velocity fluctuations is accompanied by exponential tails at higher velocities. The

role of Reynolds number is to render the velocity distributions narrower in passing from $Re = 0$ to $Re = O(1)$.

We note that the LB method allows simulation of fluid motion with finite inertia, and thus provides a capability not available in Stokesian Dynamics. In the present formulation, the shear flow is implemented using walls in the gradient direction, with periodicity in the other directions. While this represents experiments better in some measure than a fully periodic model, we are nonetheless limited by this because the results are dependent on position relative to the walls. Hence it would be useful to compare the results obtained here with those from a LB model with Lees-Edwards boundary conditions [107].

Chapter 6

Constitutive modeling of suspensions with inertia

6.1 Introduction

Liquid-particle suspensions are encountered in many industries such as petroleum, paints, coatings, cosmetics, and minerals processing. It is often required to predict the flow and the distribution of the dispersed solid phase for the design and optimization of multiphase reactors, unit operations and waste disposal systems. On the microscopic level, the mechanics of the system is governed by the Navier-Stokes equation for the fluid (assumed to be Newtonian) coupled with the Newton's equations for the motion of particles. However, the solution techniques are mathematically complex and time-consuming. On the other hand for design purposes, the details of the flow at the particle scale are not required and the macroscopic or averaged information is generally sufficient. Thus to allow for modeling of realistic macroscopic problems, the suspension is viewed more conveniently as continuum. At minimum, this approach requires a set of averaged equations of mass and momentum balance for the particle and fluid phases and a constitutive law relating the mixture stress to the strain rate [108].

The modeling efforts to date have been limited to Stokes flow suspensions and largely aimed at describing the migration phenomena occurring in concentrated suspensions. Leighton & Acrivos [23] first observed that in a shear rate varying flow such as the wide gap Couette, the particles undergo cross-stream migration termed *shear-induced migration*. Since then it has been observed in many curvilinear [24] as well as pressure-driven flows in a pipe [25] and channel [109, 26]. Based on the non-Newtonian rheology of the suspensions Nott & Brady [102] developed a "suspension balance model" to demonstrate that the migration is driven by the normal stresses in the suspensions. Later on a new version of the model [28] successfully predicted the particle segregation in curvilinear and the pressure-driven flows [29].

The progress in understanding the role of inertia in suspensions has been limited to the single particle and dilute systems. Experimental findings show that small but finite inertia is the cause of interesting effects in a pressure driven pipe flow: particles migrate to an equilibrium position located at $0.6R$, where R is the radius of the pipe, with the position moving closer to the wall as pipe Reynolds number increases [31, 32, 33]. The theoretical analysis on a single particle in Poiseuille flow reveals the existence of a lateral force acting on the particle [35, 36, 38, 93]. This lateral force yielding migration is directed away from both the wall and the centerline and has a zero in between. The only experimental work, to our knowledge, concerning inertial migration of dense suspensions is by Han *et al.* [110]. The authors used magnetic resonance imaging to study concentration profiles at varying bulk concentrations ϕ_0 and particle Reynolds number Re. The authors observed that: 1. at low ϕ_0 and high Re, the concentration profile peaks at a distance $0.6R$ from the center, 2. for a moderately dense suspension at high Re, the concentration is maximum at the center but a local maximum develops in the profile midway between the center and the wall. Hampton *et al.* [25] reported different fully developed concentration profiles for the

different sized particles in pipe flow. The result is influenced by the inertial lift force as will be discussed in the present study. Recently, Yan & Koplik [111] performed lattice-Boltzmann simulations to understand the effects of inertia and buoyancy for $0.1 \leq \phi_0 \leq 0.35$ in pressure-driven channel flows.

Our interest here is to carry our understanding of inertia to the next level by developing the macroscopic equations for dense suspensions. Specifically, we seek to model the bulk migration phenomenon in situations where inertia is relevant. First we present the governing equations of the suspension balance model. The inertial effects are taken into account by introducing the lift force term in the particle phase momentum balance and proposing a constitutive law relating the mixture stress to the local rate of strain with Reynolds number effects on the stress included based on our prior work [112]. The validity of the proposed model is examined by comparison to experiments for the case of pressure-driven flow of a moderately concentrated suspension in a circular pipe.

6.2 Governing equations and constitutive model

In this section, we formulate a constitutive model that takes into account inertial effects in particulate two-phase flows. We choose to build on the suspension balance model proposed by Nott & Brady [102] and Morris & Boulay [28]. The model considers the suspension as a continuum consisting of solid and fluid phases. The fluid is Newtonian with density ρ and viscosity μ_0. The particles are non-Brownian, monodisperse and spherical with radius a. In the following equations $\boldsymbol{u}$ and $\boldsymbol{u}_p$ denote the bulk suspension and particle phase velocities, respectively. The particle migration flux relative to the bulk motion is then written as $\boldsymbol{j}_\perp = \phi(\boldsymbol{u}_p - \boldsymbol{u})$, where ϕ is the particle volume fraction. The suspension and particle phase averaged quantities are

denoted by $\langle\rangle$ and $\langle\rangle_p$. A summary of the governing equations, based on mass and momentum balances for the particle phase and the total suspension, is presented below.

1. Suspension mass and momentum balances

$$\boldsymbol{\nabla} \cdot \boldsymbol{u} = 0, \tag{6.1}$$

$$\langle\rho\rangle(\frac{\partial \boldsymbol{u}}{\partial t} + \boldsymbol{u} \cdot \nabla \boldsymbol{u}) = \boldsymbol{\nabla} \cdot \boldsymbol{\Sigma} + \langle\rho\rangle \boldsymbol{g}, \tag{6.2}$$

where $\boldsymbol{\Sigma} = \boldsymbol{\Sigma}^f + \boldsymbol{\Sigma}^p$ is the bulk suspension stress and $\langle\rho\rangle \boldsymbol{g}$ is the mean gravity force.

2. Particle-phase mass and momentum balance

$$\frac{\partial \phi}{\partial t} + \boldsymbol{u} \cdot \nabla \phi = -\nabla \cdot \boldsymbol{j}_{\perp}, \tag{6.3}$$

$$\langle\rho\rangle_p(\frac{\partial \phi \boldsymbol{u}_p}{\partial t} + \boldsymbol{u}_p \cdot \nabla \phi \boldsymbol{u}_p) = \boldsymbol{\nabla} \cdot \boldsymbol{\Sigma}^p + n\langle \boldsymbol{F}^H \rangle_p + n\langle \boldsymbol{F}^l \rangle_p + \phi \triangle \rho \boldsymbol{g}, \tag{6.4}$$

where, $\boldsymbol{\Sigma}_p$ is the particle stress and $n = 3\phi/4\pi a^3$ is the number density of particles. In the momentum balance equation the hydrodynamic drag force, $\langle \boldsymbol{F}^H \rangle_p$, the lift force, $\langle \boldsymbol{F}^l \rangle_p$ and the buoyancy force $\phi \triangle \rho \boldsymbol{g}$ arise due to interphase momentum transfer. The drag force is modeled similar to the drag in sedimentation and it is expressed as $\langle \boldsymbol{F}^H \rangle_p = 6\pi\mu_0 a f^{-1}(\boldsymbol{u}_p - \boldsymbol{u})$, where f^{-1} is the mean mobility of particle phase [28, 29]. Note that the lift force term considered herein arises in finite inertia flows and hence was neglected in the previous studies on the modeling of Stokes flow suspension [102, 28, 29]. The lift force acts perpendicular to the drag and is a complex function of the imposed flow, as will be discussed later.

The left hand side of equation (6.4) is taken as zero when the flow is quasi-steady

and axially invariant. One can then obtain an expression for the particle flux as

$$\boldsymbol{j}_{\perp} = \phi(\boldsymbol{u}_p - \boldsymbol{u}) = \frac{2a^2}{9\mu_0} f(\phi)[\nabla \cdot \boldsymbol{\Sigma}^p + n\langle \boldsymbol{F}^l \rangle_p + \phi \triangle \rho \boldsymbol{g}]. \tag{6.5}$$

3. Suspension stress law

The total suspension stress takes the form $\boldsymbol{\Sigma} = \boldsymbol{\Sigma}^f + \boldsymbol{\Sigma}^p$, where $\boldsymbol{\Sigma}^f$ and $\boldsymbol{\Sigma}^p$ are the fluid and particle phase contributions. The fluid phase stress is expressed as

$$\boldsymbol{\Sigma}_f = -\langle p \rangle_f \boldsymbol{I} + 2\mu \boldsymbol{E}, \tag{6.6}$$

where $\langle p \rangle_f$ is the average pressure in the fluid phase, $\boldsymbol{I}$ and $\boldsymbol{E} = \frac{1}{2}[\boldsymbol{\nabla u} + (\boldsymbol{\nabla u})^T]$ are the identity and local rate of strain tensors, respectively. Based on the rheology of a suspension at steady shear presented in chapter 5, we propose the constitutive models for the relative viscosity ($\mu_r = \Sigma/\dot{\gamma}$), normal stress differences ($N_1 = \Sigma - xx^p - \Sigma^p_{yy}, N_2 = \Sigma^p_{yy} - \Sigma^p_{zz}$) and particle pressure ($\Pi = -\frac{1}{3}[\Sigma^p_{xx} + \Sigma^p_{yy} + \Sigma^p_{zz}]$). Here, x, y and z are the flow, gradient and the vorticity directions, respectively, and $\dot{\gamma}$ is the shear rate.

The major findings of chapter 5 include rise of relative viscosity of the suspension with $Re = \rho\dot{\gamma}a^2/\mu_0$ and a change in the sign of second normal stress difference, N_2. Note that a Newtonian fluid does not exhibit normal stresses while the Stokes flow suspension exhibits negative N_2 for all ϕ. It is the inertia which induces positive N_2 in the dilute limit and negative N_2 at higher ϕ through the structural anisotropy. The first normal stress difference, N_1, is negative and the particle pressure, Π, is positive for all ϕ, and both scale approximately linearly with Re at low ϕ. The following models are obtained by curve-fitting the numerical data as a function of ϕ and Re in

the range $0.05 \leq \phi \leq 0.4$ and $0.01 \leq Re \leq 5.0$.

• *Relative viscosity*

$$\mu_r(\phi) = \mu[1 + 1.5\phi(1 - \frac{\phi}{\phi_m})^{-1}]^2, \tag{6.7}$$

Here we disregard the Reynolds number dependence of viscosity as it is weak for $Re \leq 0.5$ which is the typical value of Re considered in the present study. We take the maximum packing fraction as $\phi_m = 0.68$ to allow for some polydispersity in the system.

• *First normal stress difference and particle pressure*

$$\frac{N_1, \Pi(\phi, Re)}{\mu_0 \dot{\gamma}} = a_1 Re(\frac{\phi}{\phi_m})(1 - \frac{\phi}{\phi_m})^{-1.5} + a_2(\frac{\phi}{\phi_m})^2(1 - \frac{\phi}{\phi_m})^{-1.5}, \tag{6.8}$$

where a_1 and a_2 are the fitting parameters and are different for N_1 and Π. The form of second term is similar to the one proposed by Morris & Boulay [28] and recovers a finite value in the limit of $Re = 0$. As can be seen, the first term scales linearly with Re at low ϕ.

• *Second normal stress difference*

$$\frac{N_2(\phi, Re)}{\mu_0 \dot{\gamma}} = b_1 Re(\frac{\phi}{\phi_m})^{1.2} - b_2 Re(\frac{\phi}{\phi_m})^{0.8}(1 - \frac{\phi}{\phi_m})^{-2} - b_3(\frac{\phi}{\phi_m})^2(1 - \frac{\phi}{\phi_m})^{-2}. \tag{6.9}$$

The first term takes into account positive sign of N_2 and the linear scaling of Re for $\phi \leq 0.1$. The last term implies a negative N_2 at higher ϕ and the change of sign over the parameters ϕ and Re is governed by the second term.

The relative viscosity, the first and second normal stress differences and the particle pressure describe the particle stress tensor $\mathbf{\Sigma}^p$ completely for steady shear flow.

6.3 Problem description and solution method

We consider a steady but axially developing pressure-driven flow of a neutrally-buoyant suspension in a circular pipe of radius R. The sketch of the computational domain is shown in figure 6.1a. Our primary interest is in finding the fully developed profiles for the particle volume fraction ϕ and the axial velocity u_z. We assume one-dimensional mean flow and develop an approximate form of the governing equations presented in the previous section. For a steady flow, the evolution of solid fraction and the axial velocity along the length of pipe is governed by particle phase mass balance and the suspension mass and momentum balances and is given as

$$\boldsymbol{u} \cdot \nabla \phi = -\nabla \cdot \boldsymbol{j}_{\perp}, \tag{6.10a}$$

$$0 = \boldsymbol{\nabla} \cdot \boldsymbol{u}; \qquad 0 = \boldsymbol{\nabla} \cdot \boldsymbol{\Sigma} \tag{6.10b}$$

The variations along the axial direction ($\partial/\partial z$) are neglected compared to cross-stream direction ($\partial/\partial r$), as a result the above equations are reduced to

$$u_z \frac{\partial \phi}{\partial z} = -\frac{\partial j_{\perp,r}}{\partial r}, \tag{6.11a}$$

$$0 = -\frac{\partial p}{\partial z} + \frac{\partial \Sigma_{rz}}{\partial r}, \tag{6.11b}$$

where the migration flux is written as

$$j_{\perp,r} = -\frac{2a^2}{9\mu_0} f(\phi) [\frac{\partial \Sigma^p_{rr}}{\partial r} + \frac{N_2}{r} + nF^l]. \tag{6.12}$$

The above equation for particle flux when substituted into equation (6.10a) takes into account the combined mass and momentum balance for the particle phase. The inertial lift force that is responsible for the migration of a single particle midway

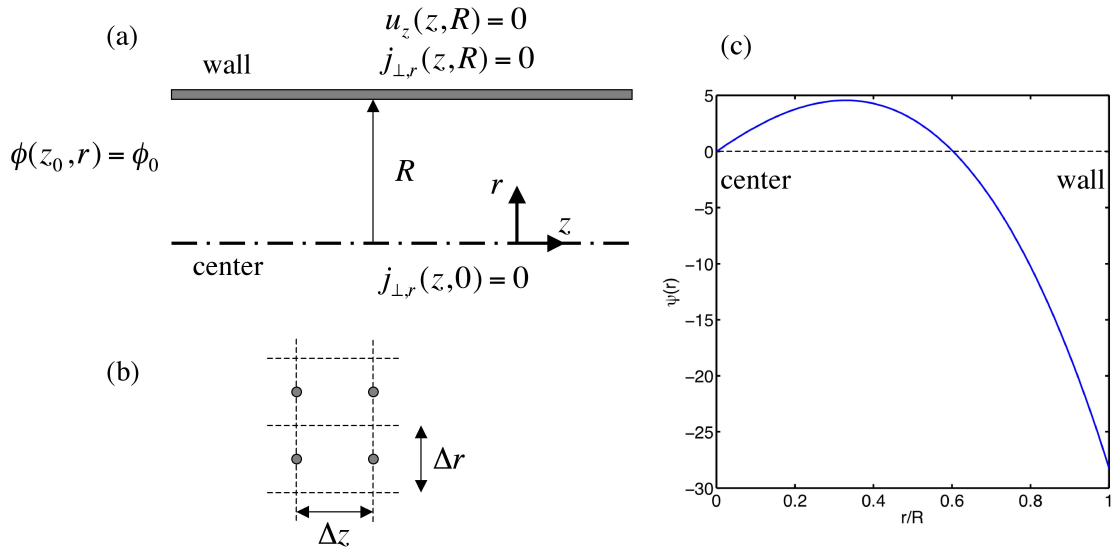

Figure 6.1: (a) Sketch of the pipe geometry and conditions imposed. (b) The staggered grid for cross-stream direction used in this work. The dashed line and circle denote the grid boundary and the midpoint of the grid, respectively. (c) The inertial lift force on a single particle as a function of dimensionless radial distance r/R [36].

between the center and the wall [32, 36, 38, 33] is modeled as

$$\frac{F_p^l}{U_m \mu_0 a} = Re_c (\frac{a}{R})^3 \psi(r), \tag{6.13}$$

where $\psi(r)$ is a scalar function known from Vasseur & Cox [36]. The sign and magnitude of ψ depends on the radial distance r/R, as illustrated in figure 6.1c. It is assumed that the lift force is not altered by the presence of other particles. In the above expression, $Re_c = 2\rho U_m R/\mu_0$ is the pipe Reynolds number based on the maximum velocity U_m at the center of pipe.

At the inlet $z = z_0$, the solid fraction is uniformly distributed with value ϕ_0. The no slip and the symmetry conditions are implemented at the wall and the centerline, respectively. The particle flux normal to the wall and the centerline is set equal to zero. To solve equation (6.11), we use an explicit Euler scheme with a staggered grid in the cross-stream direction (r) and a regular grid in the axial direction (z).

As illustrated in figure 6.1b, ϕ and $j_{\perp,r}$ are computed at the center of the grid and the grid boundary, respectively. We typically use $\triangle r = 0.01R$ and $\triangle z = 0.1\triangle r$, to generate the results presented in this chapter.

The solution for $\phi(z,r)$ and $u_z(z,r)$ is obtained as follows. With $\phi(z,r) = \phi_0$ at the starting axial position $z = z_0$, the pressure-driven velocity profile is computed from (11b). Now, in order to conserve the total mass flux (particle + fluid) at the next axial position ($z = z_0 + \triangle z$), the pressure drop $\partial p/\partial z$ is solved iteratively to get a new $\phi(z,r)$ and u_z. To conserve the particle flux, ϕ obtained is linearly rescaled as

$$\phi_{new} = \phi \frac{Q_0}{Q}, \tag{6.14}$$

where $Q = 2\int_0^R u\phi r dr$ and Q_0 denote the particle flux and the inlet particle flux. This ensures that the particle flux remains at the inlet value. The sequence is repeated until ϕ reaches its fully developed form ($\partial\phi/\partial z = 0$). This is the marching method solution of the axially developing profile presented in Miller & Morris [29].

The parameters governing the particle segregation in the pipe are the Reynolds number Re_c, the imposed bulk concentration ϕ_0 and the pipe to particle size ratio $\lambda = R/a$.

6.4 Results

In this section, we present our model predictions together with available experimental data at the same conditions. First, we consider the experimental study of Hampton *et al.* [25]. This work has often been compared to suspension flow models as a test case, assuming the flow is a Stokes flow. In fact, the Reynolds number is non-negligible based on our analysis using the data on conditions presented by the

authors. The experiments utilized particles of size 3175 μm and 650 μm in a pipe of diameter 50.8 mm and 25.4 mm, respectively. With the help of NMR imaging, the authors reported qualitatively different fully developed particle concentration profiles for two different pipe to particle size ratio ($\lambda = R/a$). They observed a sharp peak at the center and the wall for a small λ and a relatively broader profile accompanied by a gradual drop in concentration near the wall for a large λ. This effect was attributed to the finite size of the particles by Han *et al.* [110] but no physical interpretation was given. The recently developed Stokes flow suspension model [29] failed to capture the change in profile upon varying λ, but the authors identified the role of boundaries.

We have analyzed the experimental results by considering the lift on particles. In the present model, the lift force, given by Eq. (12), depends on the particle size ratio λ and Re_c and hence we expect to see the difference in fully developed profiles. We choose $\lambda = 16$ and 40 to match the conditions of experiments presented in Hampton *et al.* [25]. The inlet volume fraction is $\phi_0 = 0.2$ and the Reynolds number is $Re_c = 3$. Shown in figure 6.2a is the fully developed particle volume fraction as a function of radial distance, r/R. The particles migrate to the centerline where a sharp peak in concentration exists and then it drops steadily. For $\lambda = 40$, the present model and the Stokes flow model of Miller & Morris [29] compare well with the experimental data except at the wall ($r/R > 0.95$) where both models predict $\phi \approx 0.1$ whereas the experiments find zero ϕ. For $\lambda = 16$, the present model captures the gradual drop in concentration beyond $r/R \geq 0.6$ whereas a Stokes flow model fails to predict it. A notable difference is seen in the centerline concentration which is much smaller in the experiments ($\phi \approx 0.42$) than predicted by our model ($\phi = 0.58$).

Figure 6.2b illustrates the case for $\phi_0 = 0.3$. The suspension again reaches to different fully developed profiles for the two particle size ratios. There are only quantitative changes from the one for $\phi_0 = 0.2$. First, the centerline concentration is

(a)

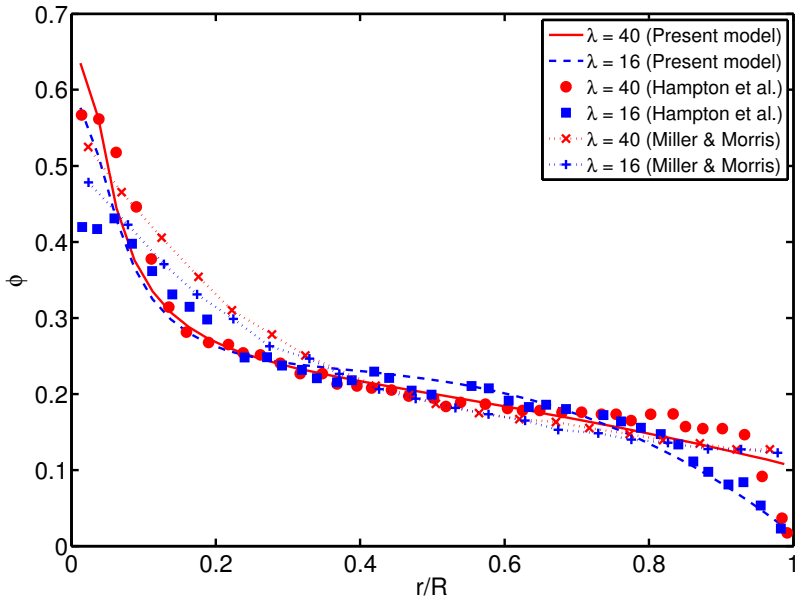

(b)

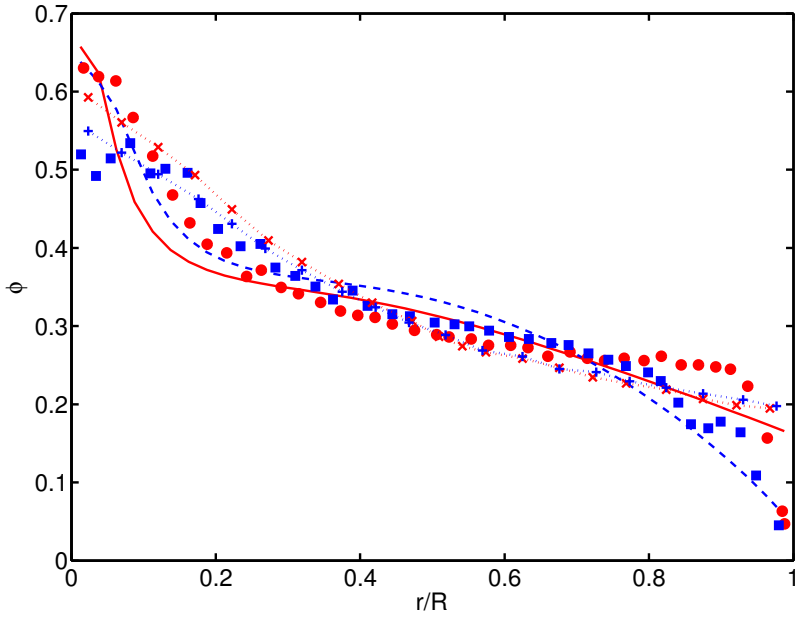

Figure 6.2: The fully developed concentration profiles in a circular pipe for differing $\lambda = R/a$ when (a) $\phi_0 = 0.2$, (b) $\phi_0 = 0.3$.

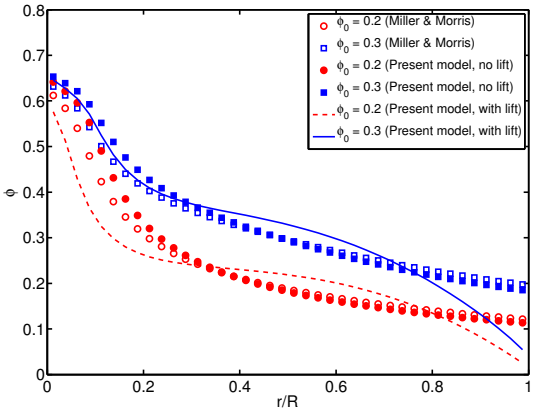

Figure 6.3: The model predictions of the fully developed concentration profiles in a circular pipe for $\phi_0 = 0.2$ and 0.3 when $\lambda = R/a = 16$. The results are presented for the lift-free Stokes flow rheology (open symbols), lift-free inertial rheology (closed symbol) and the complete model.

higher and second, the drop in ϕ for $r/R \geq 0.7$ is more evident. Again, we obtain a good match with the experiments.

It is to be noted that the broader profile and the drop in concentration near the wall are influenced by the inertial lift forces. As discussed in the previous section, the inertial lift force drives the particles away from both the centerline and the wall. To demonstrate this, we isolate the effect of lift force from the present model. In figure 6.3, we plot the concentration profiles with present rheological model with and without the lift along with the rheological model of Miller & Morris. The predictions of lift-free model with the inertial rheology and the Stokes rheology [28] are comparable, with the former predicting a slightly higher concentration at the center. When the lift is considered, concentration at the center and the wall drops leading to an 'S'-shaped profile.

Next, we consider the axial velocity for varying λ. Illustrated in figure 6.4a is the fully developed axial velocity as a function of radial distance, r/R, for $\lambda = 16$ and 40 when the imposed bulk concentration is $\phi_0 = 0.2$. For comparison the experimental

data from Hampton *et al.* [25] is also shown. The velocity values are normalized by the average axial velocity. The predicted velocity profile and the parabolic profile for a Newtonian fluid are shown by the solid and the dotted lines respectively. The departure of the velocity from the Newtonian behavior is evident. The present model predictions match very well with the experiments. The flattening of the profile is apparent when compared to parabolic profile. For small particles, the centerline velocity is ≈ 1.9 times the average velocity, but decreases further for large particles. The profiles almost collapse on a single curve beyond $r/R \geq 0.55$. Thus the degree of flattening increases with decreasing λ.

The axial velocity for the case of $\phi_0 = 0.3$ is shown in figure 6.4b. The non-Newtonian effects are enhanced as there is a greater deviation from the Newtonian behavior. For $\lambda = 40$, the match between the model and the experiments is good. However, for $\lambda = 16$, the model underpredicts the velocity in the region $0.1 \leq r/R \leq 0.5$ as the experiments reveal a much flatter profile.

We now briefly study the effect of Re_c and ϕ_0 on the fully developed concentration profiles in the pipe. The conditions are chosen to match the experiments of Han *et al.* [110]. The particle radius is one-tenth of the pipe radius ($\lambda = 10$). In figure 6.5a, the concentration distribution for $\phi_0 = 0.1$ is shown for $Re_c = 1.5, 7$ and 11. When $Re_c = 1.5$, the concentration peaks at the axis of pipe and decreases monotonically toward the wall. It is expected that at low Re_c, the inertial flux is weak and migration toward the center is predominantly driven by the normal stresses. When $Re_c = 7$, there is a sharp cusp at the axis but otherwise the suspension is almost uniformly distributed across the pipe. As Re_c increases further to 11, a transition pattern is seen in the profile. The concentration near the center drops rapidly and the particles accumulate in the region $0.5 \leq r/R \leq 0.9$. In all the cases we obtain a good match with the experiments. Note that the cusp at the axis was not seen in the experiments

(a)

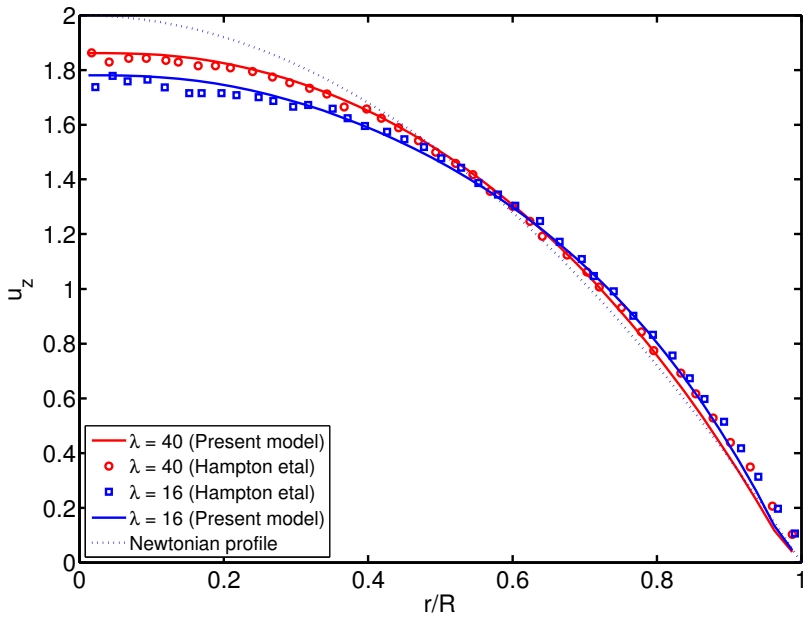

(b)

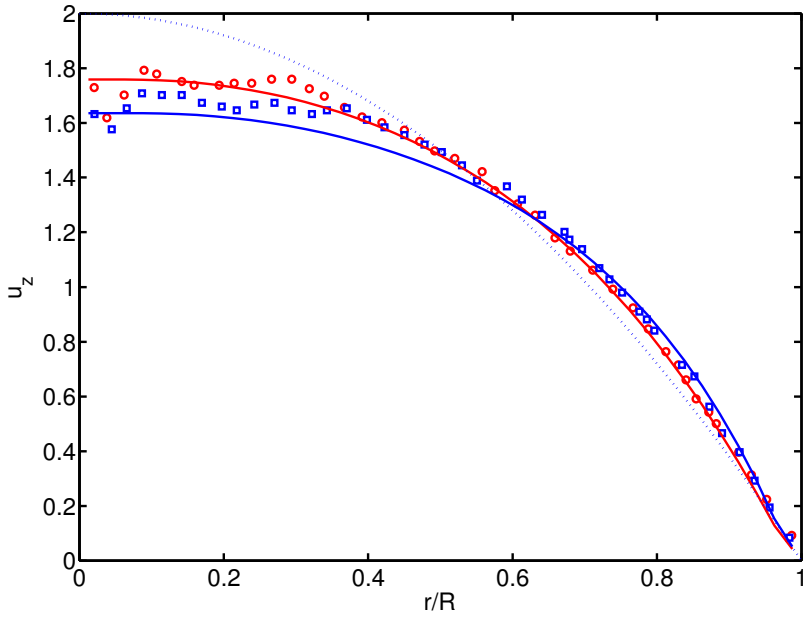

Figure 6.4: The fully developed velocity profiles in a circular pipe for differing $\lambda = R/a$ when (a) $\phi_0 = 0.2$, (b) $\phi_0 = 0.3$.

for $Re_c = 7$ as the spatial resolution of MRI was small but it was seen for $Re_c = 11$ where the inertial effects are large.

The model predictions for solid loading of $\phi_0 = 0.2$ are shown in figure 6.5b. Comparing to $\phi_0 = 0.1$, the transition pattern is qualitatively different as Re_c increases. The concentration always peaks at the axis. At low $Re_c = 1.2$, it decreases steadily from $\phi = 0.6$ at the center to $\phi = 0.06$ at the wall. The match with experiments is good except near the wall where the experimental data reveal absence of particles. For $Re_c = 4.0$, the model calculations show a sharp peak at the tube axis but ϕ is uniform in the region $0.1 \leq r/R \leq 0.7$ after which it drops. When Re_c is increased further to 8.0, a broader peak is obtained near $r/R \approx 0.6$ due to the strong inertial flux. It is seen that the model computes a profile that overestimates the effect of inertia compared to experiments which show that the concentration drops steadily from the center to $r/R = 0.4$ and then there is a small hump near $r/R = 0.6$.

The poor quantitative agreement with the experiments is expected to result from finite-size effects. It is to be noted that in the present model the lift force is computed from the asymptotic theory on a single particle. The key assumption of the theory is that the particle is too small to disturb the imposed Poiseuille flow. In the present case for $\lambda = R/a = 10$, the finite-size effects on the disturbance flow cannot be ignored even in the dilute limit. Recent finite element simulations on a particle in a square channel have revealed complex scaling of the lift force with the ratio of particle to channel size [96]. Furthermore, our model does not take into account the influence of other particles on the inertial lift force. To our knowledge, this information is not known in the literature and a future investigation in the area is warranted. Therefore we do not present the results for $\phi_0 > 0.2$.

(a)

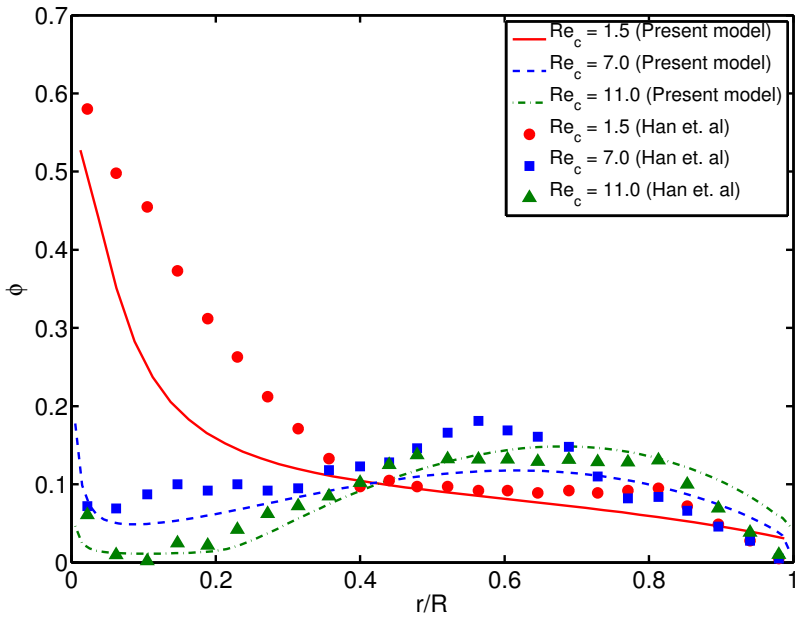

(b)

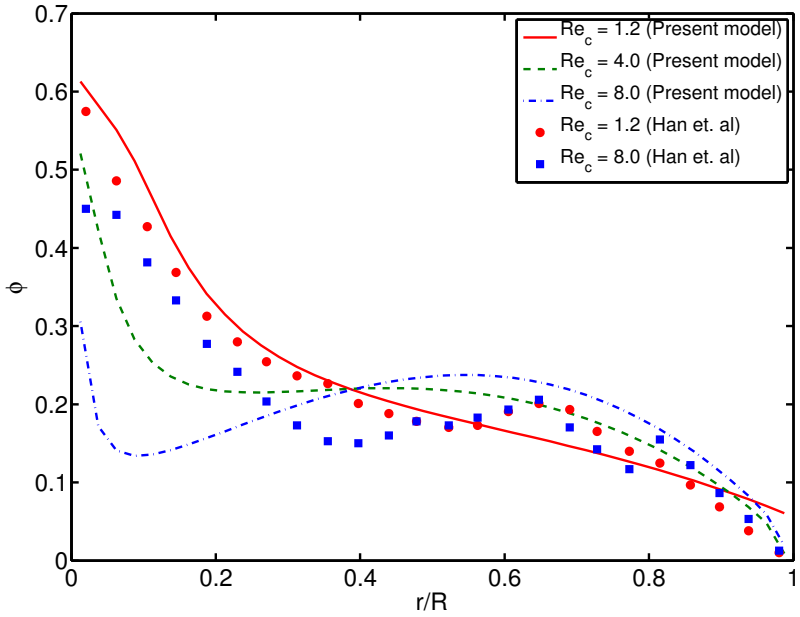

Figure 6.5: The fully developed concentration profiles in a circular pipe for differing Re_c when (a) $\phi_0 = 0.1$, (b) $\phi_0 = 0.2$.

6.5 Conclusion

We have examined the constitutive modeling of particulate two-phase flows under the influence of inertia. The study was divided into two parts. In the first part, following the suspension balance approach we presented the governing equations for the mass and momentum balances of the particle phase and total suspension. We introduced the lift force, that acts perpendicular to the drag and becomes non-negligible in finite-inertia flows. The bulk stress of the suspension is modeled as a function of solid fraction ϕ and the Reynolds number on particle scale Re_p using the numerical data on rheology at steady shear presented in chapter 5.

In the second part we evaluated the model by considering the pressure-driven flow of a moderately concentrated suspension in a circular pipe. The evaluation was facilitated by consideration of two case studies in the literature. In the first, we revisited the experimental study of Hampton *et al.* [25] that reported two different fully developed particle concentration profiles for varying particle sizes. We attributed the result to the influence of inertial lift force that scales with cube of the particle to pipe size ratio. This lateral force is responsible for driving the particles away from both the wall and the center, leading to an 'S'-shaped concentration profile that matched very well with the experiments. In the second case, we studied the effect of pipe Reynolds number Re_c and the solid loading ϕ_0. At low Re_c, the concentration is maximum at the center and decreases steadily toward the wall. The model predicts a transition pattern in the solid distribution as Re_c increases. For low ϕ_0, the particles develop a maximum midway between the wall and the tube axis. When ϕ_0 is high, the concentration peaks at the centerline but there is a hump in the profile at a distance of $0.6R$ from the tube axis due to the inertial flux. We obtained a qualitative match with the experiments of Han *et al.* [110].

Bibliography

[1] G. K. Batchelor, An Introduction to Fluid Dynamics, Cambridge University Press, London, U.K., 1967.

[2] J. Happel, H. Brenner, Low Reynolds Number Hydrodynamics, Pentice-Hall, Englewood Cliffs, U.S., 1965.

[3] L. G. Leal, Laminar Flow and Convective Transport Processes, Butterworth-Heinemann, U.K., 1992.

[4] G. K. Batchelor, The stress system in a suspension of force free particles, J. Fluid Mech. 41 (1970) 545.

[5] G. K. Batchelor, J. T. Green, The hydrodynamic interation of two small freely-moving spheres in a linear flow field, J. Fluid. Mech. 56 (1972) 375–400.

[6] G. K. Batchelor, J. T. Green, The determination of the bulk stress is a suspension of spherical particles to order c^2, J. Fluid. Mech. 56 (1972b) 401–427.

[7] D. J. Jeffrey, Y. Onishi, Calculation of the resistance and mobility functions for two unequal rigid spheres in low-Reynolds-number flow, J. Fluid. Mech. 139 (1984) 261–290.

[8] S. Kim, R. T. Mifflin, The resistance and mobility functions of two equal spheres in low-Reynolds-number flow, Phys. Fluids 28 (1985) 2033–2045.

[9] D. J. Jeffrey, Higher order corrections to the axisymmetric interactions of nearly touching spheres, Phys. Fluids A 1 (1989) 1740.

[10] D. J. Jeffrey, The calculation of the low Reynolds number resistance functions for two unequal spheres, Phys. Fluids 4 (1992) 16–29.

[11] J. F. Brady, G. Bossis, Stokesian Dynamics, Annu. Rev. Fluid Mech. 20 (1988) 111–157.

[12] A. Sierou, J. F. Brady, Accelerated Stokesian Dynamics simulations, J. Fluid Mech. 448 (2001) 115.

[13] G. K. Batchelor, The effect of Brownian motion on the bulk stress in a suspension of spherical particles, J. Fluid Mech. 83 (1977) 97–117.

[14] J. F. Brady, J. F. Morris, Microstructure of strongly sheared suspensions and its impact on rheology and diffusion, J. Fluid. Mech. 348 (1997) 103–139.

[15] D. R. Foss, J. F. Brady, Structure, diffusion and rheology of Brownian suspensions by Stokesian Dynamics simulation, J. Fluid Mech. 407 (2002) 167–200.

[16] J. F. Morris, B. Katyal, Microstructure from simulated Brownian suspension flows at large shear rate, Phys. Fluids 14 (2002) 1920.

[17] T. N. Phung, J. F. Brady, G. Bossis, Stokesian Dynamics simulation of Brownian suspensions, J. Fluid Mech. 313 (1996) 181–207.

[18] A. Sierou, J. F. Brady, Rheology and microstructure in concentrated noncolloidal suspensions, J. Rheol. 46 (2002) 1031.

[19] F. Parsi, F. Gadala-Maria, Fore-and-aft asymmetry in a concentrated suspension of solid spheres, J. Rheol. 31 (1987) 725.

[20] F. Gadala-Maria, The rheology of concentrated suspension, Ph.D. thesis, Standford University, US (1979).

[21] I. E. Zarraga, D. A. Hill, D. T. Leighton, The characterization of the total stress of concentrated suspensions of noncolloidal spheres in Newtonian fluids, J. Rheol. 44 (2000) 185.

[22] A. Singh, P. R. Nott, Experimental measurements of the normal stresses in sheared Stokesian suspensions, J. Fluid Mech. 490 (2003) 293.

[23] D. T. Leighton, A. Acrivos, The shear induced migration of particles in concentrated suspensions, J. Fluid Mech. 181 (1987) 415.

[24] A. W. Chow, S. W. Sinton, J. H. Kwamia, T. S. Stephens, Shear-induced particle migration in couette and parallel plate viscometers: NMR imaging and stress measurements, Phys. Fluids 6 (1994) 2561–2576.

[25] R. E. Hampton, A. A. Mammoli, A. L. Graham, N. Tetlow, S. A. Altobelli, Migration of particles undergoing pressure-driven flow in a circular conduit, J. Rheol. 41 (1997) 621–640.

[26] M. K. Lyon, L. G. Leal, An experimental study of motion of concenterated supension in two-dimensional channle flow part 1. Monodisperse systems, J. Fluid Mech. 363 (1998) 25–36.

[27] P. R. Nott, J. F. Brady, Pressure-driven flow of suspensions: theory and simulations, J. Fluid Mech. 157 (1994) 157.

[28] J. F. Morris, F. Boulay, Curvilinear flows of noncolloidal suspensions: the role of normal stresses, J. Rheol. 43 (1999) 1213.

[29] R. M. Miller, J. F. Morris, Normal stress driven migration and axial development in pressure-driven flow of concentrated suspensions, J. Non-Newtonian Fluid Mech. 135 (2006) 149.

[30] W. L. McCabe, J. C. Smith, P. Harriott, Unit Operations of Chemical Engineering, McGraw-Hill International Editions, Singapore, 1993.

[31] G. Segré, A. Silberberg, Radial particle displacements in Poiseuille flow of suspensions, Nature 189 (1961) 209.

[32] G. Segré, A. Silberberg, Behaviour of macroscopic rigid spheres in Poiseuille flow part 2. Experimental results and interpretation, J. Fluid Mech. 14 (1962) 136.

[33] J. Matas, J. F. Morris, E. Guazzelli, Inertial migration of rigid spherical particles in Poiseuille flow, J. Fluid Mech. 515 (2004) 171–195.

[34] P. G. Saffman, The lift on a small sphere in a slow shear flow, J. Fluid Mech. 22 (1965) 385–400.

[35] B. P. Ho, L. G. Leal, Inertial migration of rigid spheres in two-dimensional unidirectional flows, J. Fluid Mech. 65 (1974) 365.

[36] P. Vasseur, R. G. Cox, The lateral migration of a spherical particle in two-dimensional shear flows, J. Fluid Mech. 78 (1976) 385–413.

[37] J. A. Schrönberg, E. J. Hinch, Inertial migration of a sphere in Poiseuille flow, J. Fluid Mech. 203 (1989) 517–524.

[38] E. S. Asmolov, The inertial lift on a spherical particle in a plane Poiseuille flow at large channel Reynolds number, J. Fluid Mech. 381 (1999) 63.

[39] C. R. Robertson, A. Acrivos, Low Reynolds number shear flow past a rotating circular cylinder. Part 1. Momentum transfer, J. Fluid Mech. 40 (1970) 685–703.

[40] C. Kossack, A. Acrivos, Steady simple shear flow past a cirular cylinder at moderate Reynolds number: a numerical solution, J. Fluid Mech. 66 (1974) 353–376.

[41] G. G. Poe, A. Acrivos, Closed streamline flows past rotating single spheres and cylinders: inertia effects, J. Fluid. Mech. 72 (1975) 605–623.

[42] D. R. Mikulencak, J. F. Morris, Stationary shear flow around fixed and free bodies at finite Reynolds number, J. Fluid Mech. 520 (2004) 215–242.

[43] G. Subramanian, D. L. Koch, Centrifugal forces alter streamline topology and greatly enhance the rate of heat and mass transfer from neutrally buoyant particles to a shear flow, Phys. Rev. Lett 96 (2006) 134503.

[44] G. Subramanian, D. L. Koch, Inertial effects on the transfer of heat or mass from neutrally buoyant spheres in a steady linear velocity field, Phys. Fluids 18 (2006) 073302.

[45] C. J. Lin, J. H. Peery, W. R. Schowalter, Simple shear flow round a rigid sphere: Inertial effects and suspension rheology, J. Fluid Mech. 44 (1970) 1–17.

[46] A. S. Sangani, G. Mo, H.-K. Tsao, D. L. Koch, Simple shear flow ofdense gas-solid suspensions at finite Stokes number, J. Fluid Mech. 313 (1996) 309–341.

[47] D. L. Koch, R. J. Hill, Inertial effects in suspension and porous media flows, Annu. Rev. Fluid Mech. 33 (2001) 619–647.

[48] T. A. Johnson, V. C. Patel, Flow past a sphere up to a Reynolds number of 300, J. Fluid Mech. 378 (1999) 19–70.

[49] T. N. Swaminathan, K. Mukundakrishnan, H. H. Hu, Sedimentation of an ellipsoid inside an infinitely long tube at low and intermediate Reynolds numbers, J. Fluid Mech. 551 (2006) 357–385.

[50] P. Y. Huang, D. D. Joseph, Effects of shear thinning on migration of neutrally-buoyant particles in pressure driven flow of Newtonian and viscoelastic fluid, J. Non-Newtonian Fluid Mech. 90 (2000) 159–185.

[51] N. A. Patankar, H. H. Hu, Finite Reynolds number effect on the rheology of a dilute suspension of neutrally buoyant circular particles in a Newtonian fluid, Intl. J. Multiphase Flow 28 (2002) 409.

[52] P. J. Hoogerbrugge, J. M. Koelman, Simulating microscopic hydrodynamic phenomena with dissipative particle dynamics, Europhys. Lett. 19 (1992) 155.

[53] E. Clement, M. R. Maxey, Numerical simulations of random suspensions at finite Reynolds numbers, Int. J. Multiphase Flow 29 (2003) 579–601.

[54] A. J. C. Ladd, Numerical simulations of particulate suspensions via a discretized Boltzmann equation. Part 1. Theoretical foundation, J. Fluid Mech. 271 (1994a) 285–309.

[55] S. Chen, G. D. Doolen, Lattice-Boltzmann method for fluid flows, Annu. Rev. Fluid. Mech. 30 (1998) 329–364.

[56] C. K. Aidun, Y. Lu, E. J. Ding, Direct analysis of particulate suspensions with inertia using the discrete Boltzmann equation, J. Fluid Mech. 373 (1998) 287–311.

[57] A. J. C. Ladd, R. Verberg, Lattice-Boltzmann simulations of particle-fluid suspensions, J. Stat. Phys. 104 (2001) 1191–1151.

[58] N. Q. Nguyen, A. J. C. Ladd, Lubrication corrections for lattice-Boltzmann simulation of particle suspensions, Phys. Rev. E 66 (2002) 046708.

[59] N. Q. Nguyen, A. J. C. Ladd, Sedimentation of hard-sphere suspensions at low Reynolds number, J. Fluid Mech. 525 (2005) 73–104.

[60] J. Kromkamp, D. T. M. van den Ende, D. Kandhai, R. G. M. van der Sman, R. M. Boom, Shear-induced self-diffusion and microstructure in non-Brownian suspensions at non-zero Reynolds number, J. Fluid Mech. 529 (2005) 253–278.

[61] A. Shakib-Manesh, P. Raiskinmaki, A. Kopenen, M. Kataja, J. Timonen, Shear stress in a couette flow of liquid-particle suspensions, J. Stat. Phys. 107 (2002) 67.

[62] P. Raiskinmaki, J. A. Åstrom, M. Latva-Kokko, A. Kopenen, A. Jasberg, J. Timonen, Clustering and viscosity in a shear flow of a particle suspension, Phys. Rev. E 68 (2003) 061403.

[63] J. Hyvaluoma, P. Raiskinmaki, A. Kopenen, M. Kataja, J. Timonen, Strain hardening in liquid particle suspensions, Phys. Rev. E 72 (2005) 061402.

[64] A. J. C. Ladd, Numerical simulations of particulate suspensions via a discretized Boltzmann equation. Part 2. Numerical results, J. Fluid Mech. 271 (1994b) 311–339.

[65] U. Frisch, D. D'Humièrs, B. Hasslacher, P. Lallemand, Y. Pomeau, J. P. Rivet, Lattice gas hydrodynamics in two and three dimension, Complex Systems. 1 (1987) 649.

[66] F. Higuera, S. Succi, R. Benzi, Lattice gas dynamics with enhanced collisions, Europhys. Lett. 9 (1989) 345–349.

[67] J. Hyvaluma, P. Raiskinmaki, A. Kopenen, M. Kataja, Lattice-Boltzmann sumulation of particle suspensions in shear flow, J. Stat. Phys. 121 (2005) 149.

[68] S. Kim, S. J. Karrila, Microhydrodynamics: Principles and Selected Applications, Butterworth-Heinemann series in Chemical Engineering, Boston, U.S., 1991.

[69] S. Wakiya, C. L. Darabaner, S. G. Mason, Particle motions in sheared suspensions XXI: Interaction of rigid spheres (Theoretical), Rheol. Acta. 6 (1967) 273–284.

[70] C. J. Lin, K. J. Lee, N. F. Sather, Slow motion of two spheres in a shear field, J. Fluid. Mech. 43 (1970) 35–47.

[71] H. Brenner, M. E. O'Neill, On the Stokes resistance of multiparticle systems in a linear shear field, Chem. Engng. Sci. 27 (1972) 1421.

[72] I. E. Zarraga, D. T. Leighton, Normal stress and diffusion in a dilute suspension of hard spheres undergoing simple shear, Phys. Fluids 13 (2001) 565–577.

[73] A. J. C. Ladd, Hydrodynamic interactions in a suspension of spherical particles, J. Chem. Phys. 88 (1988) 5051–5063.

[74] C. L. Darabaner, S. G. Mason, Particle motions in sheared suspensions XXII: Interaction of rigid spheres (Experimental), Rheol. Acta. 6 (1967) 273–284.

[75] H. H. Hu, D. D. Joseph, M. J. Crochet, Direct simulation of fluid particle motions, Theor. Comput. Fluid Dyn. 3 (1992) 285–306.

[76] H. H. Hu, Direct simulation of flows of solid-liquid mixtures, Int. J. Multiphase Flow 22 (1996) 335–352.

[77] H. H. Hu, N. A. Patankar, M. Y. Zhu, Direct numerical simulations of fluid-solid systems using the arbitrary Lagrangian-Eulerian technique, J. Comp. Phys 169 (2001) 427–462.

[78] J. Feng, H. H. Hu, D. D. Joseph, Direct simulation of initial value problems for the motion of solid bodies in a Newtonian fluid. Part 2. Couette and Poiseuille flows, J. Fluid Mech. 277 (1994) 271–301.

[79] J. Matas, V. Glezer, E. Guazzelli, J. F. Morris, Trains of particles in finite-Reynolds-number pipe flow, Phys. Fluids 16 (2004) 4192–4195.

[80] B. Chun, A. J. C. Ladd, Inertial migration of neutrally buoyant particles in a square duct: An investigation of multiple equilibrium positions, Phys. Fluids 18 (2006) 031704.

[81] G. Subramanian, J. F. Brady, Trajectory analysis for non-Brownian inertial suspensions in simple shear flow, J. Fluid Mech. 559 (2006) 151–203.

[82] H. Nirschl, H. A. Dwyer, V. Denk, Three-dimensional calculations of the simple shear flow around a single particle betwen two moving walls, J. Fluid Mech. 283 (1995) 273–285.

[83] E. J. Ding, C. K. Aidun, The dynamics and scaling law for particles suspended in shear flow with inertia, J. Fluid Mech. 423 (2000) 317–344.

[84] M. Zurita-Gotor, J. Blawzdziewicz, E. Wajnryb, Swapping trajectories: a new wall-induced cross-streamline particle migration mechanism in a dilute suspension of spheres, J. Fluid Mech. 592.

[85] C. M. Zettner, M. Yoda, The circular cylinder in simple shear at moderate Reynolds number: An experimental study, Exps. Fluids 30 (2001) 346–353.

[86] F. R. da Cunha, E. J. Hinch, Shear–induced dispersion in a dilute suspension of rough spheres, J. Fluid Mech. 309 (1996) 211–223.

[87] D. Di Carlo, D. Irima, R. G. Tompkins, M. Toner, Continuous inertial focusing, ordering, and separation of particles in microchannels, Proc. Natl. Acad. Sci. 515 (2007) 104.

[88] D. Di Carlo, J. F. Edd, D. Irima, R. G. Tompkins, M. Toner, Equilibrium separation and filtration of particles using differential inertial focusing, Anal. Chem. 80 (2008) 2204.

[89] J. F. Edd, D. Di Carlo, K. J. Humphry, S. Köster, D. Irima, D. A. Weitz, M. Toner, Controlled encapsulation of single-cells into monodisperse picolitre drops, Lab Chip 104 (2008) 18892.

[90] A. S. Bhagat, S. S. Kuntaegowdanahalli, I. Papautsky, Enhanced particle filtration in straight microchannels using shear-modulated inertial migration, Phys. Fluids 20 (2008) 101702.

[91] A. S. Bhagat, S. S. Kuntaegowdanahalli, I. Papautsky, Inertial microfluidics for continuous particle filtration and extraction, Microfluid Nanofluid 5 (2008) 185–192.

[92] J. Matas, J. F. Morris, E. Guazzelli, Lateral forces on a sphere, Oil Gas Sci. Technol. 59 (2004) 59–70.

[93] J. Matas, J. F. Morris, E. Guazzelli, Lateral force on a rigid sphere in large-inertia laminar pipe flow, J. Fluid Mech. 621 (2009) 59–67.

[94] X. Shao, Z. Yu, B. Sun, Inertial migration of spherical particles in circular Poiseuille flow at moderately high Reynolds numbers, Phys. Fluids 20 (2008) 103307.

[95] Y. W. Kim, J. Y. Yoo, the lateral migration of neutrally-buoyant spheres transported through square microchannels, J. Micromech. Microeng. 18 (2008) 1.

[96] D. D. J. F. Edd, K. J. Humphry, H. A. Stone, M. Toner, Particle segregation and dynamics in confined flows, Phys. Rev. Lett. 102 (2009) 094503.

[97] P. M. Kulkarni, J. F. Morris, Pair sphere trajectories in finite-Reynolds-number shear flow, J. Fluid Mech. 596 (2008) 413.

[98] K. J. Humphry, Effects of confinement on two-phase flow in microfluidics devices, Ph.D. thesis, Harvard University, Boston US (2009).

[99] S. R. Wickramasinghe, W.-C. Lin, D. S. Dandy, Separation of different sized particles by inertial migration, Biotechnol. Lett. 23 (2001) 1417–1422.

[100] H. A. Barnes, Shear-thickening (dilatancy) in suspensions of nonaggregating solid particles dispersed in newtonian liquids, J. Rheol. 33 (1989) 329–366.

[101] J. F. Brady, G. Bossis, The rheology of concentrated suspensions in simple shear flow by numerical simulations, J. Fluid Mech. 155 (1988) 105.

[102] P. R. Nott, J. F. Brady, Pressure-driven suspension flow: Simulation and theory, J. Fluid Mech. 275 (1994) 157–199.

[103] Y. Yan, J. F. Morris, J. Koplik, Hydrodynamic interaction of two particles in confined linear shear flow at finite Reynolds number, Phys. Fluids 19 (2007) 113305.

[104] D. T. Leighton, The shear induced migration of particulates in concentrated suspensions, Ph.D. thesis, Stanford University, US (1985).

[105] G. K. Batchelor, J. T. Green, The hydrodynamic interation of two small freely-moving spheres in a linear flow field, J. Fluid. Mech. 56 (1972) 375–400.

[106] G. Drazer, J. Koplik, B. Khushid, A. Acrivos, Deterministic and stochastic behavior of non-Brownian spheres in sheared suspensions, J. Fluid Mech. 460 (2002) 307.

[107] A. J. Wagner, I. Pagonabarraga, Lees-Edwards boundary conditions for lattice Boltzmann, Int. J. Miner. Process. 107 (1998) 521.

[108] D. A. Drew, Mathematical modeling of two-phase flow, Ann. Rev. Fluid Mech. 15 (1983) 261–291.

[109] C. J. Koh, P. Hookham, L. G. Leal, An experimental investigation of concentrated suspension flows in a rectangular channel, J. Fluid Mech. 266 (1994) 1–32.

[110] M. Han, C. Kim, M. Kim, S. Lee, Particle migration in tube flow of suspensions, J. Rheol. 43 (1999) 1157–1174.

[111] Y. Yan, J. Koplik, Transport and sedimentation of suspended particles in inertial pressure-driven flow, Phys. Fluids 21 (2009) 013301.

[112] P. M. Kulkarni, J. F. Morris, Suspension properties at finite Reynolds number from simulated shear flow, Phys. Fluids 20 (2008) 040602.